Low-Scale String Resonances at the Large Hadron Collider

by

Pourya Vakilipourtakalou

A thesis submitted in partial fulfillment of the requirements for the degree of

Master of Science

Department of Physics

University of Alberta

Abstract

If the large extra dimensions scenario [1, 2] is correct, the string scale M_s of string theory can be of the order of a few TeV; a theory known as low-scale string theory. In the D-brane [3, 4] formulation of low-scale string theory, string resonances (Regge excitations) can be produced in proton-proton collisions through 2-parton scatterings, and furthermore, in the limit $M_s \to \infty$ these scattering amplitudes match the tree-level scattering amplitudes derived in QCD. Using the cross-sections and decay widths of the string resonances, we write a Monte Carlo event generator, STRINGS-1.00, for the production and decay of the first and second string resonances, such that colour, quark flavour, baryon number, electric charge and total angular momentum are conserved. STRINGS is also capable of generating QCD tree-level scatterings in proton-proton collisions. We study the discovery potential of the first string resonance at the LHC (luminosity = 140 fb^{-1}) and the upcoming HL-LHC run (luminosity = 3000 fb^{-1}) with a centre-of-mass energy of $\sqrt{s} = 13$ TeV. This is done by using STRINGS to generate events for different string scales and studying the significance of the signals over the background in the dijet invariant mass distribution. For luminosities of 140 fb^{-1} and 3000 fb^{-1}, we find the maximum detectable string scales to be 8.4 TeV and 9.1 TeV, respectively. We also use results from an ATLAS paper [5] to set upper limits on the cross-section and lower limits on string scale of the first string resonance. We find with 95% confidence level that string resonances with string scales lower than 7.4 TeV do not exist in ATLAS results with an integrated luminosity of 37 fb^{-1}.

Preface

The work presented in this thesis is original and is the author's own, except where denoted by citations.

Dedication

I would like to dedicate my Master's thesis to Maman Mahboobeh and Baba Enayat, who have been a lovely and supporting parent and always wanted the best for me.

Acknowledgements

I would like to appreciate Professor Douglas Gingrich's patience and great supervision during this research. Also, I would like to thank Sina Safarabadifarahani for his help during this work, which made my life a lot easier.

Contents

List of Tables

List of Figures

Chapter 1

Introduction

The Standard Model (SM) is the most complete model that describes matter and forces, and the interactions between them. However, some problems in the SM, like the inconsistency between the strengths of gravity and the electromagnetic force, known as the hierarchy problem [1], cause physicists to think about new theories. One of these theories is string theory, which can be considered as a candidate for a quantum field theory for gravity. In string theory, instead of zero-dimensional SM particles, there are one-dimensional strings that can be either closed or open. At low energies, strings behave like zero-dimensional SM particles and the excitations of strings from the energy ground state determine the properties of the SM particles. One way to describe SM particles in string theory is using a framework known as D-brane model [3, 4]. Based on the D-brane model, closed strings propagate in the ten-dimensional space-time, while open strings are attached to the D-brane at their end points, figure 1.1 [6]. According to the D-brane model, fermions of the SM are due to the open strings ending on stacks of D-brane and bosons are due to the open strings stretching between D-brane.

The distance scale of string theory is generally of the order of the Planck length, about 10^{-35} m, which corresponds to energy scales of the order of 10^{16} TeV, far beyond energies accessible by current colliders. However, if the large extra dimension scenario [1, 2] is correct, the string energy scale can be of the order of a few TeV. This model, with a few TeV string scale, is called low-scale string theory.

In Chapter 2 we discuss the theoretical background of low-scale string theory and how one can use the scattering amplitudes to look for string resonances in the data produced by colliders. Chapter 3 is dedicated to the phenomenological aspects of proton-proton collisions and the mechanism with which we study the scattering amplitudes to detect new physics in the invariant mass distribution of the outgoing jets. Chapter 4 describes the STRINGS Monte Carlo event generator for the production and decay of the string resonances in proton-proton

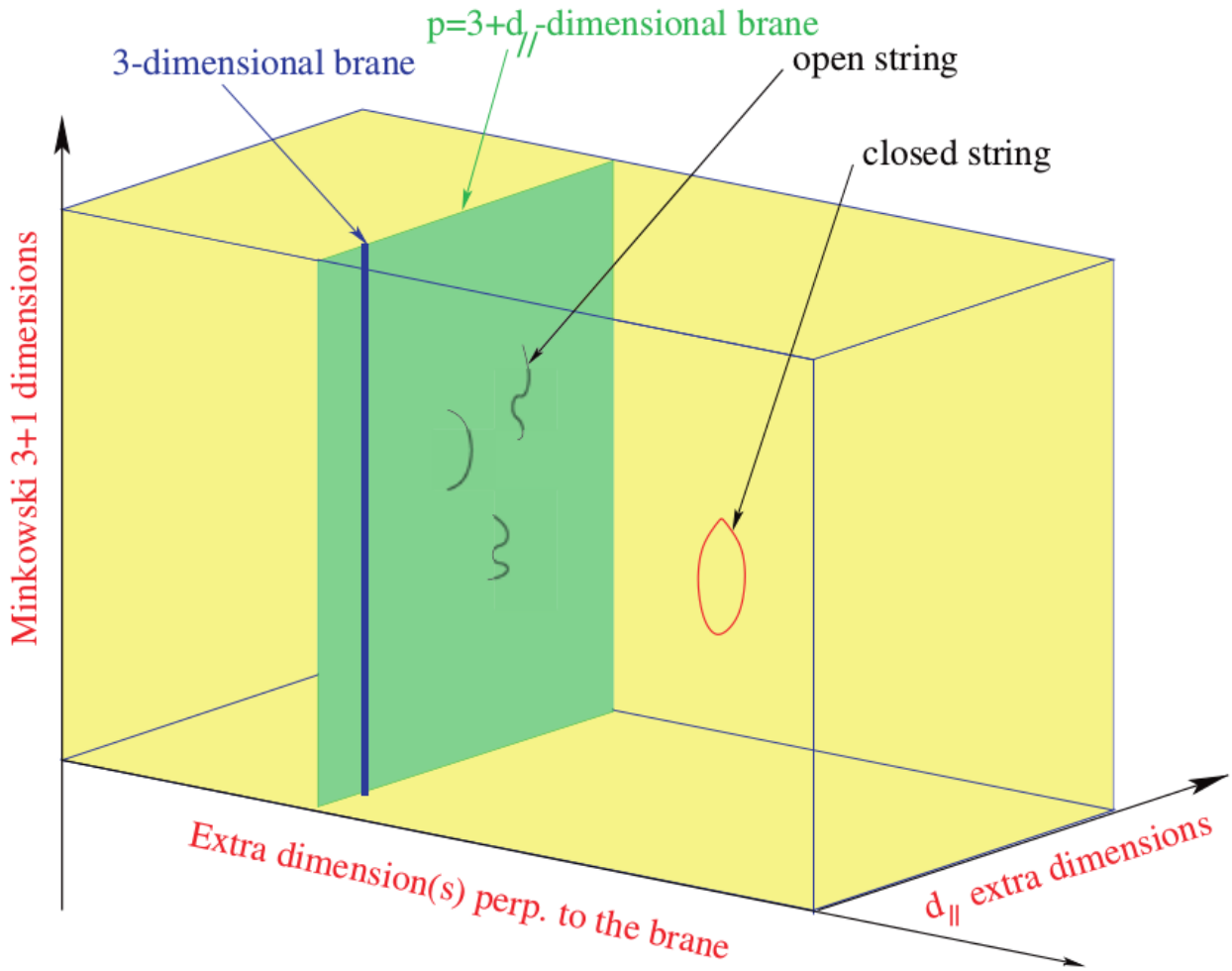

Figure 1.1: D-branes are the hosts for the end-points of the open strings. This figure is taken from [6].

collisions. We perform a comparison of QCD predictions between STRINGS and another Monte Carlo event generator, Pythia [7], and also the data recorded by ATLAS experiment at CERN [5]. In Chapter 5, we study the discovery potential of string resonances at the LHC, using the STRINGS Monte Carlo event generator. In Chapter 6, we use the data recorded by ATLAS to set upper limits on the cross-section and lower limits on the string scale of the first string resonance.

Chapter 2

Low-Scale String Theory

As was stated in the previous section, string theory implies a higher dimensional space-time. In order for string theory to be consistent with SM physics, the compactification of the extra dimensions in string theory should produce the physics of four-dimensional space-time. The Planck scale in four dimensions is given by [8]

$$M_{Pl}^2 = \frac{8}{g_s^2} M_s^8 \frac{V_6}{(2\pi)^6}, \tag{2.1}$$

where V_6 is the volume of the extra six-dimensional compactified space. According to the large extra dimension scenario [1, 2], if the size of the extra dimensions V_6 is large and the theory is weakly coupled ($g_s \ll 1$), the string scale can be of the order of a few TeV; limits on g_s [9] and the size of the extra dimensions [10] are set experimentally.

Having a low string scale makes it possible to look for evidence of string states at the LHC by looking for deviations from the SM. This can be done by comparing the invariant mass and angular distributions resulting from this theory to the data produced at the LHC.

The string scattering amplitudes of the n-gluon or quark-gluon scatterings, with at most two quarks among incoming and outgoing partons, i.e. $gg \to gg$, $gg \to q\bar{q}$, $gq \to gq$, $g\bar{q} \to g\bar{q}$, $q\bar{q} \to gg$, $gg \to g\gamma$ and $gq \to q\gamma$, are not dependent on the compactification and the geometry of higher dimensions, i.e. they are model-independent, thus they are called universal amplitudes [11, 12]. On the other hand, string scattering amplitudes with more than two quarks (or anti-quarks) among incoming and outgoing partons could lead to a set of Kaluza-Klein states [13], such as massive gravitations, which are model-dependent, since they depend on the geometry and compactification of the extra dimensions.

Generally, due to the parton distribution function (PDF) of the gluons, chapter 3.1, two-gluon and quark-gluon scatterings have the largest contribution to the total cross-section of the string resonances at low masses. However, at large masses, the contribution from qq scattering becomes significant. In order to calculate the contributions from the model-dependent scatterings, one needs to consider a specific model and calculate the scattering amplitudes in that model, which is beyond the scope of this thesis. Thus, in our studies we consider the universal amplitudes and the model-dependent scattering amplitudes, i.e. $qq \to qq$ and $q\bar{q} \to q\bar{q}$ scatterings, will be ignored. Note that since we consider the model-independent scatterings, g_s and V_6 in equation (2.1) do not enter our calculations [11].

The model of intersecting D-branes leads to a proliferation of $U(1)$ fields [8]. While the treatment of these gauge fields is model dependent, not all can be accommodated within the standard model and at least one will manifest itself as a heavy beyond-SM Z′, i.e. gauge boson corresponding to $U(1)$, that could have significant coupling to the SM particles. The models do not predict the mass of these extra gauge bosons but they cannot be very light or they would violate electroweak constraints [8]. Previous experiment searches limit a heavy Z′ to more than about 6 TeV [14]. The mass of the Z′ in our model could be expected to be of the order of the string scale, and would be related to g_s and V_6 [8].

2.1 String Resonances

Low-scale string resonances can be produced in proton-proton collisions [11, 12]. Since protons are made of partons, i.e. gluons and quarks, we study the production of the string resonances in parton-parton scatterings. If the incoming partons have four-momenta P_1 and P_2, and the outgoing partons have four-momenta P_3 and P_4, the partonic Mandelstam scalar variables $(\hat{s}, \hat{t}, \hat{u})$ are defined as [14]

$$\begin{aligned} \hat{s} &= (P_1 + P_2)^2 = (P_3 + P_4)^2, \\ \hat{t} &= (P_1 - P_3)^2 = (P_4 - P_2)^2, \\ \hat{u} &= (P_1 - P_4)^2 = (P_3 - P_2)^2. \end{aligned} \tag{2.2}$$

Conventionally, the polar angle θ of the outgoing partons in the centre-of-mass frame is mea-

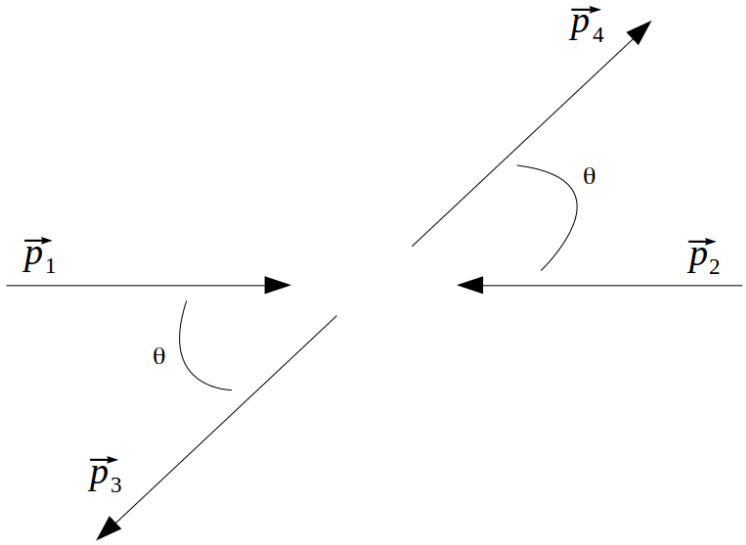

Figure 2.1: In parton-parton scattering incoming partons have three-momenta $\vec{p}_1$ and $\vec{p}_2$ and outgoing partons have three-momenta $\vec{p}_3$ and $\vec{p}_4$. The polar angle of the outgoing partons θ is measured with respect to the direction in which the incoming partons collide.

sured with respect to the direction in which incoming partons collide, such that $\theta < \pi/2$, figure 2.1. Furthermore, the invariant mass of the incoming (or outgoing) partons is defined as [14]

$$M \equiv \sqrt{\hat{s}}, \tag{2.3}$$

which, as is suggested by its name, is invariant under any Lorentz transformation. In order to study the phenomenological aspects of low-scale string resonances at the LHC, we simulate the partons' four-vector kinematics. Using the partons' four-kinematics, we calculate the di-parton invariant mass distribution and look for deviations from the QCD background. Furthermore, due to the Veneziano factors, that will be defined shortly, the angular distribution of the string resonances are different from the angular distribution of the QCD background. Thus, the angular distribution can be used as a signature for string resonances, chapter 5.

According to Regge theory [15], during the partonic scattering, intermediate states can be formed in the s-channel. Thus, the production of the string resonance in proton-proton collision can be expressed in terms of Regge excitations. The scattering amplitudes of the

model-independent parton-parton scatterings, with exchanges of excited string states (Regge excitations), are calculated in superconformal field theory [11] as

$$|M(gg \to gg)|^2 = \mathrm{g}^4 \left(\frac{1}{\hat{s}^2} + \frac{1}{\hat{u}^2} + \frac{1}{\hat{u}^2}\right) \left[\frac{9}{4}(\hat{s}^2 V_s^2 + \hat{t}^2 V_t^2 + \hat{u}^2 V_u^2) - \frac{1}{3}(\hat{s}V_s + \hat{t}V_t + \hat{u}V_u)^2\right], \tag{2.4}$$

$$|M(gg \to q\bar{q})|^2 = \mathrm{g}^4 \frac{\hat{t}^2 + \hat{u}^2}{\hat{s}^2} \left[\frac{1}{\hat{t}\hat{u}}(\hat{t}V_t + \hat{u}V_u)^2 - \frac{9}{4}V_t V_u\right], \tag{2.5}$$

$$|M(q\bar{q} \to gg)|^2 = \mathrm{g}^4 \frac{\hat{t}^2 + \hat{u}^2}{\hat{s}^2} \left[\frac{32}{9}\frac{1}{\hat{u}\hat{t}}(\hat{t}V_t + \hat{u}V_u)^2 - \frac{8}{3}V_t V_u\right], \tag{2.6}$$

$$|M(gq \to gq)|^2 = |M(g\bar{q} \to g\bar{q})|^2 = \mathrm{g}^4 \frac{\hat{s}^2 + \hat{u}^2}{\hat{t}^2} \left[V_s V_u - \frac{4}{9}\frac{1}{\hat{s}\hat{u}(\hat{s}V_s + \hat{u}V_u)^2}\right], \tag{2.7}$$

in which,

$$\mathrm{g} = \sqrt{4\pi\alpha} \tag{2.8}$$

is the QCD coupling constant and α is calculated from [8]

$$\frac{1}{\alpha(M_s)} = \frac{1}{\alpha(M_Z)} - \frac{7}{2\pi}\ln\frac{M_s}{M_Z}, \tag{2.9}$$

where, $M_Z = 91.2$ GeV and $\alpha(M_Z) = 0.118$. Furthemore,

$$V_t \equiv V(\hat{s}, \hat{t}, \hat{u}), \qquad V_u \equiv V(\hat{t}, \hat{u}, \hat{s}), \qquad V_s \equiv V(\hat{u}, \hat{s}, \hat{t}) \tag{2.10}$$

are the Veneziano form factors; functions of partonic Mandelstam variables $(\hat{s},\hat{t},\hat{u})$ and are given in terms of Gamma functions [11]:

$$V(\hat{s},\hat{t},\hat{u}) = \frac{\Gamma(1-\hat{s}/M_s^2)\Gamma(1-\hat{u}/M_s^2)}{\Gamma(1+\hat{t}/M_s^2)} = \frac{\hat{s}\hat{u}}{\hat{t}M_s^2}B(\hat{s},\hat{u}), \tag{2.11}$$

$$V(\hat{t},\hat{u},\hat{s}) = \frac{\Gamma(1-\hat{t}/M_s^2)\Gamma(1-\hat{s}/M_s^2)}{\Gamma(1+\hat{u}/M_s^2)} = \frac{\hat{s}\hat{t}}{\hat{u}M_s^2}B(\hat{t},\hat{s}), \tag{2.12}$$

$$V(\hat{u},\hat{s},\hat{t}) = \frac{\Gamma(1-\hat{u}/M_s^2)\Gamma(1-\hat{t}/M_s^2)}{\Gamma(1+\hat{s}/M_s^2)} = \frac{\hat{u}\hat{t}}{\hat{s}M_s^2}B(\hat{u},\hat{t}). \tag{2.13}$$

In order to use the Veneziano factors, for example $V(\hat{s},\hat{t},\hat{u})$, in the scattering amplitudes, we use the expansion of the corresponding B-function:

$$B(\hat{s},\hat{u}) = -\sum_{n=1}^{\infty}\frac{M_s^{2-2n}}{n!}\frac{1}{\hat{s}-nM_s^2}\left[\prod_{J=1}^{n}(\hat{u}+M_s^2J)\right], \tag{2.14}$$

which have the poles for all of the Regge excitations at invariant masses equal to $\sqrt{n}M_s$. By using equations (2.11) and (2.14), we can write $V(\hat{s},\hat{t},\hat{u})$ as [11]

$$\begin{aligned} V_t(\hat{s},\hat{u}) &= \sum_{n=1}^{\infty}\frac{\hat{s}\hat{u}}{(\hat{s}+\hat{u})M_s^2}\frac{M_s^{2-2n}}{n!}\frac{1}{\hat{s}-nM_s^2}\left[\prod_{J=1}^{n}(\hat{u}+M_s^2J)\right] \\ &= \frac{\hat{s}\hat{u}(\hat{u}+M_s^2)}{(\hat{s}+\hat{u})(\hat{s}-M_s^2)M_s^2} + \frac{\hat{s}\hat{u}(\hat{u}+M_s^2)(\hat{u}+2M_s^2)}{2(\hat{s}+\hat{u})(\hat{s}-2M_s^2)M_s^4} + \ldots \ . \end{aligned} \tag{2.15}$$

The other Veneziano factors, $V_u(\hat{t},\hat{s})$ and $V_s(\hat{u},\hat{t})$, are calculated in a similar way by expand-

ing about $\hat{t}$ and $\hat{u}$, respectively.

The $\hat{t}$, $\hat{u}$, $\hat{s}$ dependence in V_t, V_u, V_s, respectively, have been eliminated using the relation between the Mandelstam variables for massless partons, $\hat{s} + \hat{t} + \hat{u} = 0$ [14]. In our study, we took all of the incoming and outgoing partons as massless. For the incoming partons, this approximation is good since due to the PDFs the massless gluons and light quarks dominate the production subprocesses, and top quarks are not available in the PDF sets. On the other hand, the outgoing parton kinematics are affected in the case of heavy-flavour quarks. Based on the mass of the top quark and multi-TeV string resonances, we can estimate the effect on the outgoing parton kinematics to be of the order of a few percent.

2.2 First Resonance

As can be seen in equation (2.15), Veneziano factors contain infinitely many poles. It is common in particle physics that all of the resonances are described with Breit-Wigner distribution. Thus, in order to remove these divergences in the scattering amplitudes, one needs to soften these poles to a Breit-Wigner distribution [16]. Furthermore, it is impossible to remove all of the poles in a scattering amplitude at the same time, since they have different characteristics, e.g. they happen at different invariant mass. Thus, one should perform an expansion of the Veneziano factors around a single pole, which results in the removal of the other poles.

If we expand the Veneziano factor $V_t(\hat{s}, \hat{u})$ around the n^{th} pole in the s-channel ($\hat{s} \rightarrow nM_s^2$), we get the Veneziano factor corresponding to the n^{th} resonance:

$$V_t^n(\hat{s}, \hat{u}) \approx \frac{1}{\hat{s} - nM_s^2} \frac{M_s^{2-2n}}{(n-1)!} \left[\prod_{J=0}^{n-1} (\hat{u} + M_s^2 J) \right] + \frac{M_s^{2-2n}}{n!} \frac{\hat{u}}{(\hat{u} + nM_s^2) M_s^2} \left[\prod_{J=0}^{n-1} (\hat{u} + M_s^2 J) \right] + \quad .... \quad . \tag{2.16}$$

We are mainly interested in the first resonance since it happens at the lowest mass among the Regge resonances and it is the easiest resonance to produce. Thus, by applying $n = 1$ in equation (2.16), then taking into account the leading term in the expansion, we get

$$V_t^1(\hat{s},\hat{u}) \approx \frac{\hat{u}}{\hat{s}-M_s^2}. \tag{2.17}$$

Similarly, we calculate $V_u^1(\hat{t},\hat{s})$ and $V_s^1(\hat{u},\hat{t})$ as

$$V_u^1(\hat{t},\hat{s}) \approx \frac{\hat{s}}{\hat{t}-M_s^2}, \tag{2.18}$$

$$V_s^1(\hat{u},\hat{t}) \approx \frac{\hat{t}}{\hat{u}-M_s^2}. \tag{2.19}$$

As can be seen in the form of the Veneziano factors, the amplitudes include a pole at an invariant mass corresponding to $\hat{s} = M_s^2$. Softening this pole to a Breit-Wigner form makes the amplitudes have a finite value at the pole. Thus, the string resonances will have a finite decay width [16].

If the incoming partons have spins J_1 and J_2, the intermediate states, i.e. Regge excitations, will have spin J, which are calculated from the well-known equation in quantum mechanics

$$J = J_1 + J_2,\ J_1 + J_2 - 1,\ \ldots,\ |J_1 - J_2|. \tag{2.20}$$

Representing the first Regge excitations of the gluon, quarks and colour singlet by g^*, q^* and C^*, respectively, and after softening the amplitudes we have [17]

$$|M_{1st}(gg \to gg)|^2 = \frac{8}{9}\frac{\mathrm{g}^4}{M_s^4}\left\{\frac{25}{32}\left[\frac{M_s^8}{(\hat{s}-M_s^2)^2+(\Gamma^{J=0}_{g^*,1st}M_s)^2}+\frac{\hat{t}^4+\hat{u}^4}{(\hat{s}-M_s^2)^2+(\Gamma^{J=2}_{g^*,1st}M_s)^2}\right]\right. \\ \left.+\left[\frac{M_s^8}{(\hat{s}-M_s^2)^2+(\Gamma^{J=0}_{C^*,1st}M_s)^2}+\frac{\hat{t}^4+\hat{u}^4}{(\hat{s}-M_s^2)^2+(\Gamma^{J=2}_{C^*,1st}M_s)^2}\right]\right\}, \tag{2.21}$$

$$|M_{1st}(gg \to q\bar{q})|^2 = \frac{1}{2}\frac{\mathrm{g}^4}{M_s^4}\left[\frac{5}{2}\frac{\hat{u}\hat{t}(\hat{u}^2+\hat{t}^2)}{(\hat{s}-M_s^2)^2+(\Gamma^{J=2}_{g^*,1st}M_s)^2}+\frac{\hat{u}\hat{t}(\hat{u}^2+\hat{t}^2)}{(\hat{s}-M_s^2)^2+(\Gamma^{J=2}_{C^*,1st}M_s)^2}\right], \tag{2.22}$$

$$|M_{1st}(q\bar{q} \to gg)|^2 = \frac{16}{27}\frac{\mathrm{g}^4}{M_s^4}\left[\frac{5}{2}\frac{\hat{u}\hat{t}(\hat{u}^2+\hat{t}^2)}{(\hat{s}-M_s^2)^2+(\Gamma^{J=2}_{g^*,1st}M_s)^2}+\frac{\hat{u}\hat{t}(\hat{u}^2+\hat{t}^2)}{(\hat{s}-M_s^2)^2+(\Gamma^{J=2}_{C^*,1st}M_s)^2}\right], \tag{2.23}$$

$$|M_{1st}(qg \to qg)|^2 = |M_{1st}(\bar{q}g \to \bar{q}g)|^2 = \\ \frac{4}{9}\frac{\mathrm{g}^4}{M_s^2}\left[\frac{M_s^4(-\hat{u})}{(\hat{s}-M_s^2)^2+(\Gamma^{J=1/2}_{q^*,1st}M_s)^2}+\frac{(-\hat{u}^3)}{(\hat{s}-M_s^2)^2+(\Gamma^{J=3/2}_{q^*,1st}M_s)^2}\right], \tag{2.24}$$

where

$$\Gamma^{J=0}_{g^*,1st} = \frac{3}{4}\frac{\mathrm{g}^2}{4\pi}M_s, \qquad \Gamma^{J=2}_{g^*,1st} = \frac{9}{20}\frac{\mathrm{g}^2}{4\pi}M_s, \tag{2.25}$$

$$\Gamma^{J=0}_{C^*,1st} = \frac{3}{2}\frac{\mathrm{g}^2}{4\pi}M_s, \qquad \Gamma^{J=2}_{C^*,1st} = \frac{3}{4}\frac{\mathrm{g}^2}{4\pi}M_s, \tag{2.26}$$

$$\Gamma^{J=1/2}_{q^*,1st} = \frac{3}{8}\frac{\mathrm{g}^2}{4\pi}M_s, \qquad \Gamma^{J=3/2}_{q^*,1st} = \frac{3}{16}\frac{\mathrm{g}^2}{4\pi}M_s, \tag{2.27}$$

are the decay widths of the intermediate resonant states, g^*, q^* and C^*, with spin J [17].

Chapter 3

Proton-Proton Collisions

In this chapter, we go through the phenomenological aspects of proton-proton scattering and how it is possible to look for string resonances at the LHC. Since partons are constituents of protons, in order to simulate the new physics in proton-proton collisions, we need to study the distribution density of the partons in an individual proton, i.e. parton distribution functions (PDFs).

3.1 Parton Distribution Functions

Assuming the two incoming protons have four-momenta P, figure 3.1, the partons would carry a fraction of that four-momentum; these fractions are denoted by x_a and x_b. Assuming a constituent parton of the colliding proton carries a fraction x of the proton's four-momentum, one can define a momentum distribution function for that parton which is called the parton distribution function (PDF). Actually, PDFs determine the number density of a given parton, with a momentum fraction x, and at a given scale Q^2 inside the proton. These PDFs are determined by fitting data from hard scattering processes, for example, at the colliders [18]. Depending on different parametrization procedures of the data and also the accuracy, different PDF sets can be constructed [19].

We examine the PDF sets CT10 [20], CT14lo [21], CTEQ6L1 [22] and CTEQ6.6 [22]. As will be discussed in the next section, we use the PDF sets to simulate the production of the first string resonance, with a string scale of M_s, in proton-proton collisions. In our simulations, we use the string scale as the scale Q at which the PDF sets are calculated. Since the string scales that we study are around 7 TeV, chapter 5, we choose $Q = 7$ TeV ($Q^2 = 4.9 \times 10^7$ GeV^2) for our examination, figure 3.2. The minimum x that can be used to calculate the PDF sets is 10^{-6} [19]. Thus, in our analysis we choose $[10^{-6}, 1]$ for the range of x.

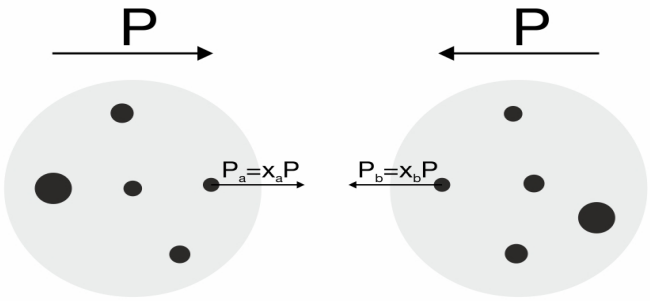

Figure 3.1: For equal proton energies, like at the LHC, incoming partons carry a portion of the incoming protons' four-momenta, $x_i P$, where $i = a, b$.

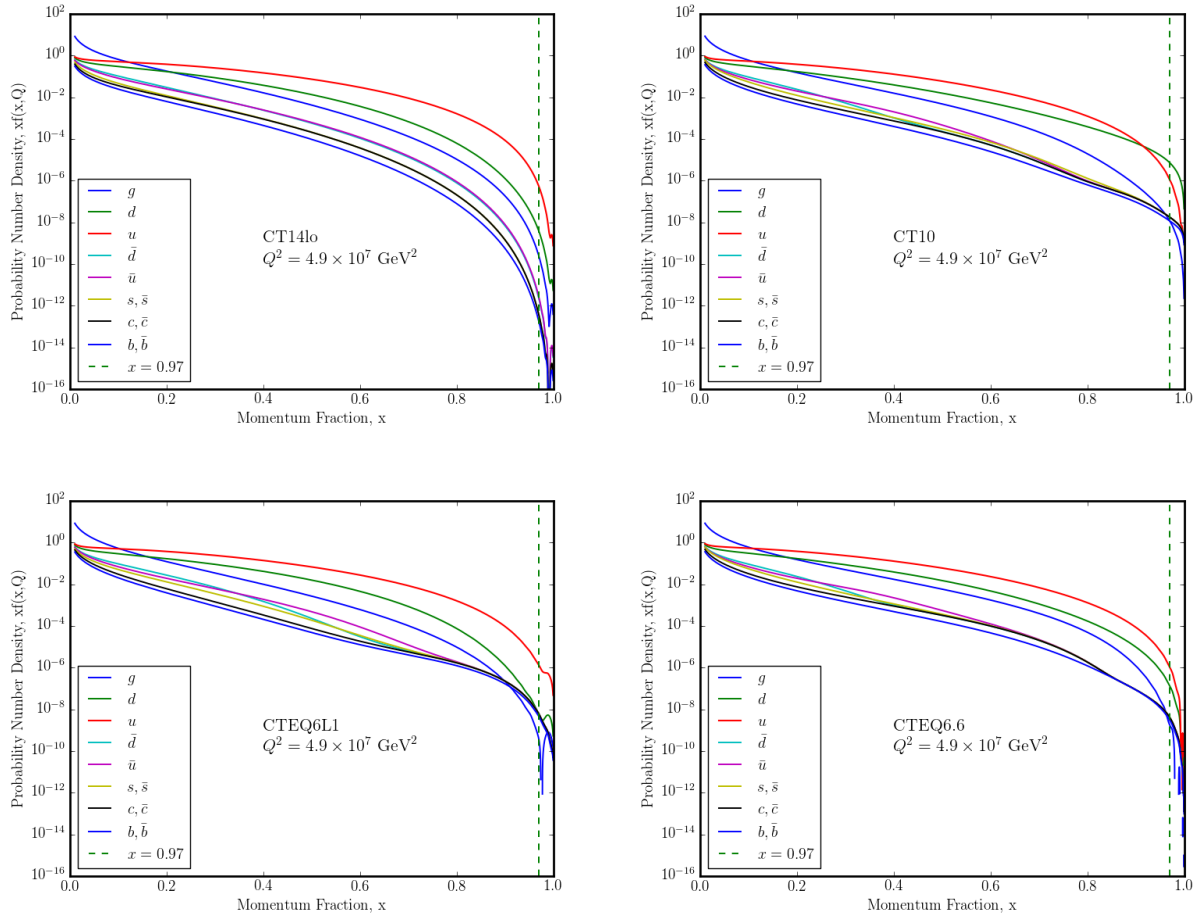

Figure 3.2: Parton distribution functions versus x at the energy scale $Q^2 = 4.9 \times 10^7$ GeV^2. A dashed line is drawn at $= 0.97$, where the unsmoothness in CTEQ6L1 starts.

As can be seen in figure 3.2, these PDF sets do not contain the probability distribution of top (t) and anti-top ($\bar{t}$) quarks. Furthermore, the high energy regions, which correspond to high values of x, are determined by extrapolating the low energy fitted functions to the higher energy regions since there are no data to constrain the high energy regions.

In order to prevent an artificial unsmoothness in the invariant mass distribution due to the PDF sets, we want to use a PDF set that is monotonically decreasing with x. As can be seen in figure 3.2, different PDF sets have bumps or fluctuations at high x. For our studies, we use the CTEQ6L1 PDF set because, historically, it is used to perform other resonance searches by ATLAS and CMS. Note that any other PDF set can also be used to perform this study, but the cross-sections would be different from our results. However, unsmoothness in the CTEQ6L1 PDF set starts at $x \approx 0.97$. On the other hand, the highest string scale that we study is 9 TeV, chapter 5. Thus, we run the STRINGS Monte Carlo event generator, which is described in chapter 4, and generate 22000 events for $M_s = 9$ TeV. As can be seen in figure 3.3, the highest x is around 0.95. Thus, the unsmoothness in the CTEQ6L1 PDF set does not affect our studies.

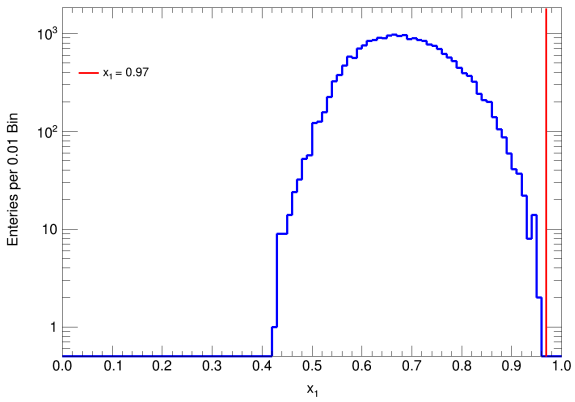

(a) x_1

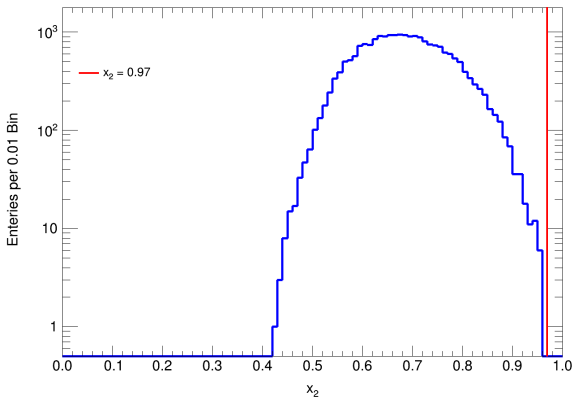

(b) x_2

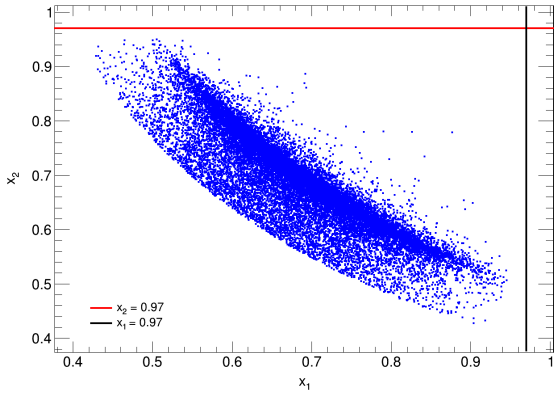

(c) x_2 versus x_1

Figure 3.3: Histograms of a) x_1 and b) x_2, and c) scatter plot of x_2 versus x_1 for $M_s = 9$ TeV. For a better visualization, $x_1 = 0.97$ and $x_2 = 0.97$ lines are drawn.

3.2 Proton-Proton Cross-Sections

In order to study proton-proton scattering, we consider the scattering of their constituent partons, $ij \to kl$, where i and j are incoming, and k and l are outgoing partons. For simplifying the form of the differential cross-sections, we define two variables y and Y in terms of the pseudorapidities of the outgoing partons η_1 and η_2 [23]:

$$\begin{aligned} Y &\equiv \frac{1}{2}(\eta_1 + \eta_2), \\ y &\equiv \frac{1}{2}(\eta_1 - \eta_2). \end{aligned} \tag{3.1}$$

By defining τ as

$$\tau = \frac{M^2}{s}, \tag{3.2}$$

where s is the centre-of-mass energy of the protons, the total differential cross-section in terms of y and Y can be written as the convolution of the parton distribution functions with the partonic scattering amplitudes [23]:

$$\frac{d\sigma}{dM} = M\tau \sum_{ij} \left(\int_{-Y_{\max}}^{Y_{\max}} dY \; f_i(x_a, M_s) \; f_j(x_b, M_s) \int_{-(y_{\max}-|Y|)}^{y_{\max}-|Y|} dy \; \frac{|\mathcal{M}(ij \to kl)|^2}{16\pi \hat{s}^2} \frac{1}{cosh^2 y} \right), \tag{3.3}$$

where $|\mathcal{M}(ij \to kl)|^2$ is the spin-averaged squared scattering amplitude for the $ij \to kl$ scattering and $y_{\max}$ is the upper limit on the absolute value of the pseudorapidities of the outgoing partons, i.e. $|\eta_1|, |\eta_2| < y_{\max}$. The maximum Y is a function of $y_{\max}$ [23]:

$$Y_{\max} = \min\{\ln(1/\sqrt{\tau}, y_{\max})\}. \tag{3.4}$$

The summation in equation (3.3) is over the gluons, quark and anti-quark flavours. $f_{i,j}$ are the PDFs for the incoming partons evaluated at the energy scale of the interaction, which we set to be the string scale throughout our study. The variables x_a and x_b can be written as functions of τ and Y [23]:

$$x_a = \sqrt{\tau}e^{Y}, \tag{3.5}$$

$$x_b = \sqrt{\tau}e^{-Y}. \tag{3.6}$$

3.3 Differential Cross-Sections

We insert the scattering amplitudes equations (2.21 - 2.24) into equation (3.3) and use the CTEQ6L1 PDF set to calculate the differential cross-sections. Figure 3.4 shows the proton-proton differential cross-sections for different subprocesses for $M_s = 8$ TeV, in which we see that QCD dominates except for $gq \to gq$ at $M_s = 8$ TeV. Figure 3.5 shows the proton-proton differential cross-sections for different string scales M_s. By integrating the proton-proton differential cross-sections over the invariant mass we calculate the total proton-proton cross-sections for different subprocesses, figure 3.6. As can be seen in figure 3.6, the $gq \to gq$ subprocess's contribution dominates for $M_s > 2$ TeV. Furthermore, above $M_s \approx 7$ TeV the only other significant contribution is $g\bar{q} \to g\bar{q}$, which is lower than $gq \to gq$ by an order of magnitude.

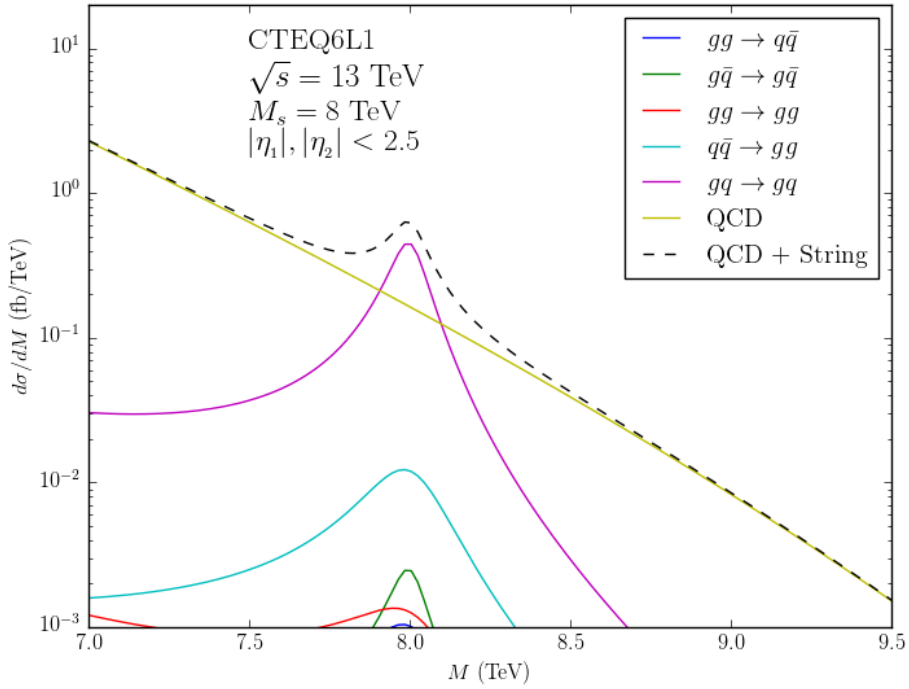

Figure 3.4: Proton-proton differential cross-section for different subprocesses for $M_s = 8$ TeV.

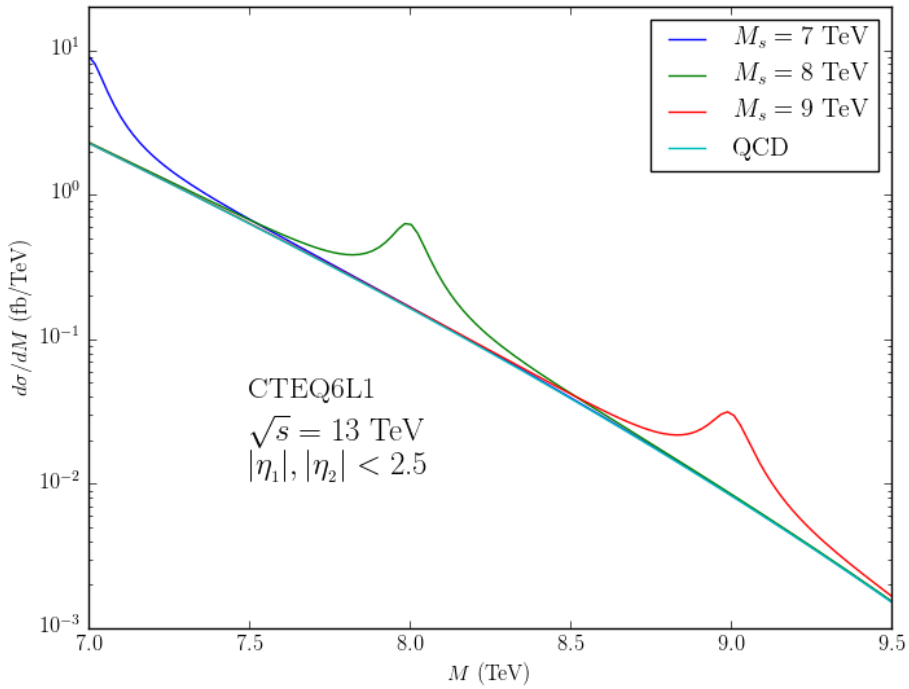

Figure 3.5: Proton-proton differential cross-section for all subprocesses added to the SM QCD cross-section for three different values of M_s. Notice that the amplitudes are approximately equal on a log scale.

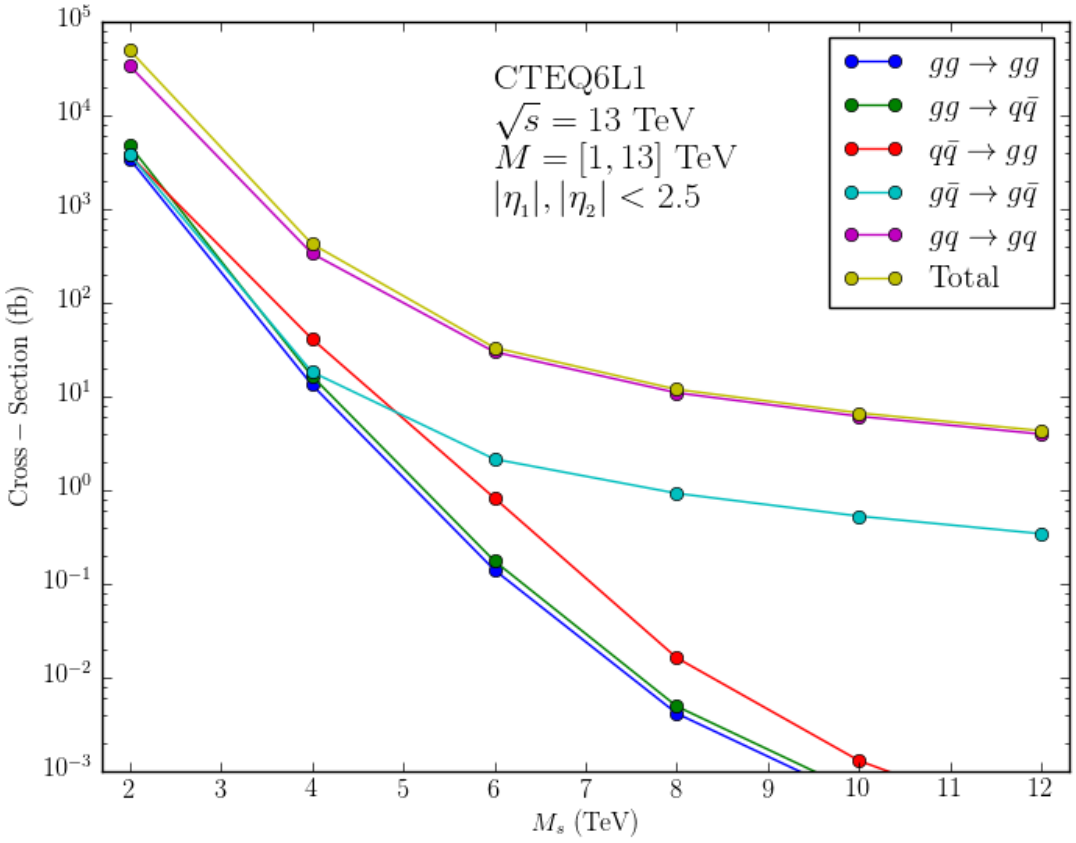

Figure 3.6: Total proton-proton cross-section of the different subprocesses versus the string scale M_s.

3.4 Breit-Wigner Study

As was discussed in the previous section, the total differential cross-section of the string resonance dominates over the differential cross-section of QCD at invariant masses around M_s. However, since the PDFs and the scattering amplitudes drop at high invariant masses, the total differential cross-section decreases with increasing invariant mass, figure 3.7; we choose $M_s = 4$ TeV to emphasize the divergence of the total differential cross-section at low-mass regions, which are closer to 4 TeV than 8 TeV. Thus, for a fixed M_s, if the integration of the total differential cross-sections is calculated over an arbitrarily large invariant mass interval that contains invariant masses significantly smaller than M_s, the contribution from QCD increases at lower mass, which results in a decrease in the significance of the resonance since it does not increase at the same rate. To increase the significance of the resonance, we find a lower requirement on the invariant mass M_{min}, at which the differential cross-section has its lowest value to the left of the peak at M_s, figure 3.8. Furthermore, by studying the Breit-Wigner curves equations (2.21 - 2.24), we find a lower requirement on the invariant mass M_{LowCut} in such a way that $[M_{\text{LowCut}}, 13\text{ TeV}]$ covers 95% of the area under the Breit-Wigner curve; the total area is chosen to cover [0.1, 13] TeV. Table 3.1 contains M_{min} and M_{LowCut} for different string scales M_s, and also the fraction of the area under the Breit-Wigner curve, covered by the region $[M_{\text{min}}, 13\text{ TeV}]$ to [0.1, 13] TeV, is shown in the last column.

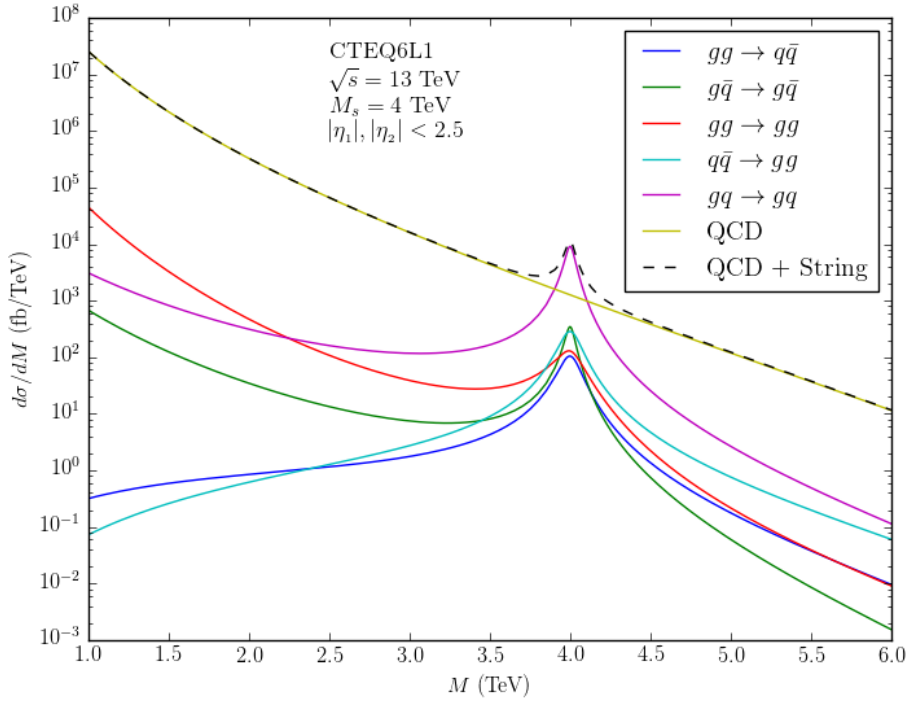

Figure 3.7: Differential cross-sections for the resonance subprocesses and QCD versus invariant mass for $M_s = 4$ TeV.

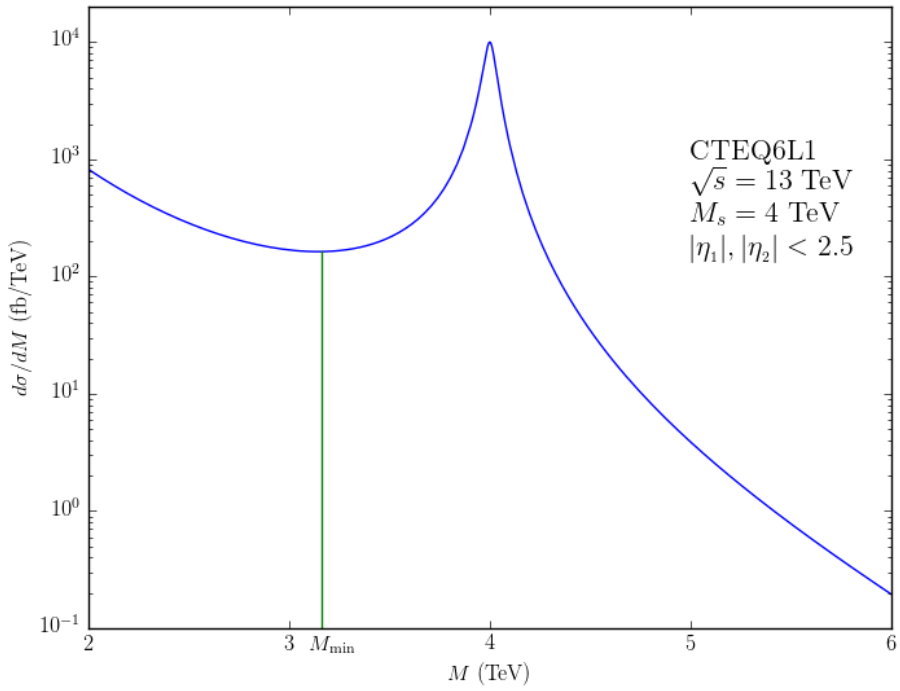

Figure 3.8: Proton-proton differential cross-section of the string resonance for $M_s = 4$ TeV. $M_{\min}$ is the mass of the minimum differential cross-section to the left of M_s.

M_s (TeV)	M_{min} (TeV)	M_{LowCut} (TeV)	Fractional Area
2.00	1.46	1.79	0.986
2.50	1.89	2.24	0.985
3.00	2.29	2.68	0.984
3.50	2.71	3.13	0.982
4.00	3.14	3.58	0.981
4.50	3.61	4.02	0.979
5.00	4.05	4.47	0.977
5.50	4.53	4.92	0.974
6.00	5.03	5.37	0.971
6.50	5.54	5.81	0.967
7.00	6.06	6.26	0.962
7.50	6.60	6.71	0.957
8.00	7.14	7.15	0.951
8.50	7.70	7.60	0.942
9.00	8.27	8.05	0.932
9.50	8.84	8.50	0.919
10.00	9.42	8.94	0.903

Table 3.1: Invariant mass requirements for different string scales M_s. M_{min} is the mass of the minimum differential cross-section to the left of M_s, and M_{LowCut} is the lower requirement on the invariant mass with which the mass interval [M_{LowCut}, 13 TeV] covers 95% of the area under the Breit-Wigner curve. The last column includes the fraction of the area under the Breit-Wigner curve covered by the invariant mass interval [M_{min}, 13 TeV].

As can be seen in table 3.1, for string scales smaller than $M_s \approx 8$ TeV, M_{min} is smaller than M_{LowCut} and the fractional area covered by the mass interval [M_{min}, 13 TeV] is greater than 95%. On the other hand, for string scales larger than $M_s \approx 8$ TeV, M_{min} is larger than M_{LowCut} and the mass interval [M_{LowCut}, 13 TeV] covers a larger invariant mass window than [M_{min}, 13 TeV]. While studying the discovery potential of the first string resonance, chapter 5, we use the cross-sections of the resonance (signal) and the QCD (background) to calculate the significance of the signal events. As was discussed earlier, in order to exclude the low-mass region, which indicates large cross-sections for the QCD background, we set lower requirements on the invariant mass. In this way, we decrease the QCD background and increase the signal to background, which corresponds to an increase in the significance of the signal over the background. In our studies, we use a lower requirement on the invariant mass, which corresponds to the larger mass window, with no upper boundary on the invariant mass.

3.4.1 Cross-Sections of the Subprocesses

Using the mass region [M_{min}, 13 TeV] from table 3.1, we calculate the cross-sections of different subprocesses versus the string scale. As can be seen in figure 3.9, the dominant subprocess for the string scales that we study is $gq \to gq$; the cross-section of $gq \to gq$ subprocess is more than two orders of magnitude larger than $q\bar{q} \to gg$ subprocess.

During writing of this thesis, it was discovered that MC samples, with dataset identifiers 312404 to 312408, made available to ATLAS are inconsistent with figure 3.9. The reason for the difference is not known at this time. The difference appears to only affect the relative subprocess contributions to the cross-section and is not believed to affect any other results in this thesis.

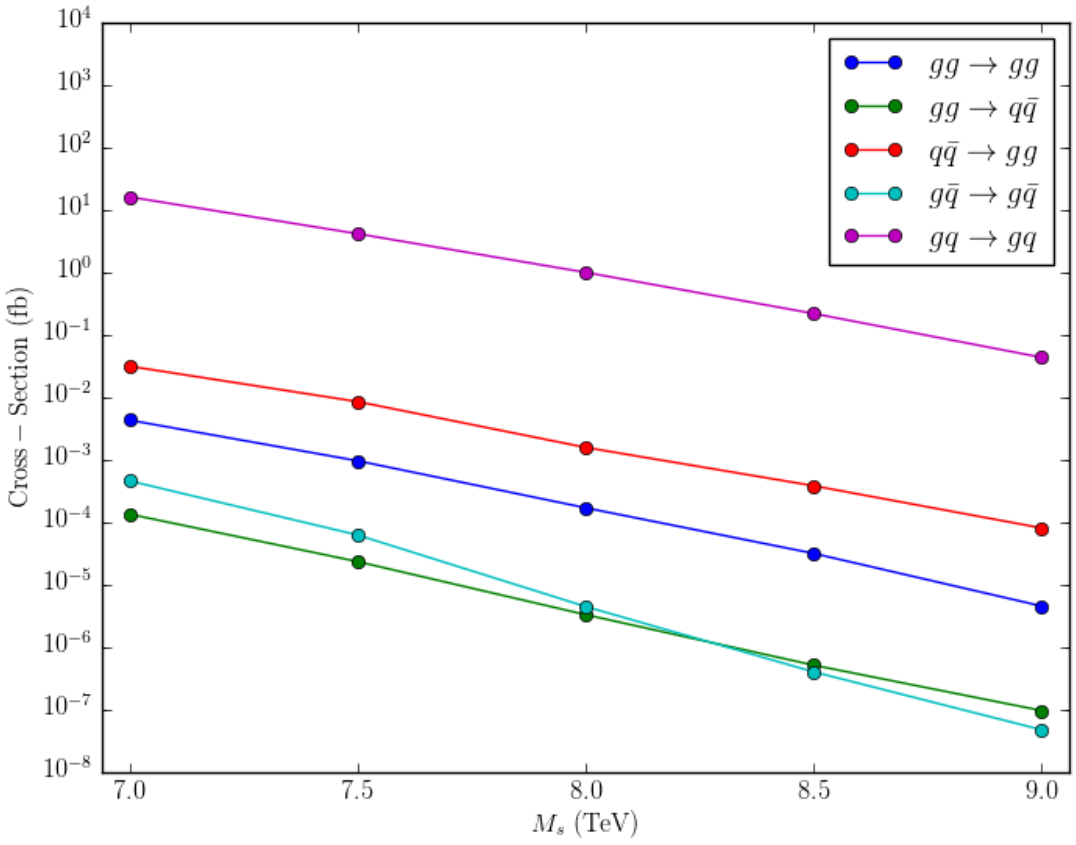

Figure 3.9: Total proton-proton cross-section of the subprocesses, using the mass range [M_{min}, 13 TeV], versus the string scale.

3.5 Validity Region of the Approximation

In order to soften the string amplitudes to a Breit-Wigner form, we used the approximation $\hat{s} \to M_s^2$ in the exact form of the Veneziano factors equations (2.11 - 2.13) to get the approximated Veneziano factors in the form of equations (2.17 - 2.19). Here we want to determine the accuracy of this approximation.

We use the exact and approximated Veneziano factors to calculate the differential cross-sections for two string scales 4 TeV and 11 TeV, figures 3.10 and 3.11. Figure 3.12 shows the ratios of the exact and approximated differential cross-sections. We use the ratios to calculate the cumulative area: we integrate the ratio by using a mass window ΔM centred at M_s and plot the result versus $\Delta M/M_s$, figure 3.13.

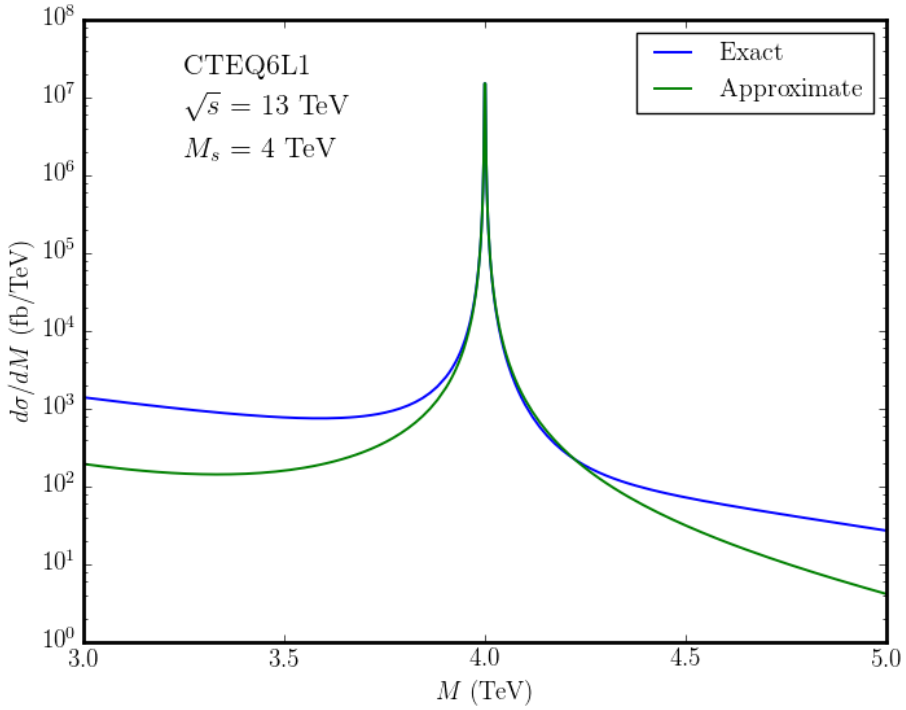

Figure 3.10: Proton-proton differential cross-section calculated from the exact (blue) and approximated (green) forms of the Veneziano factors for $M_s = 4$ TeV.

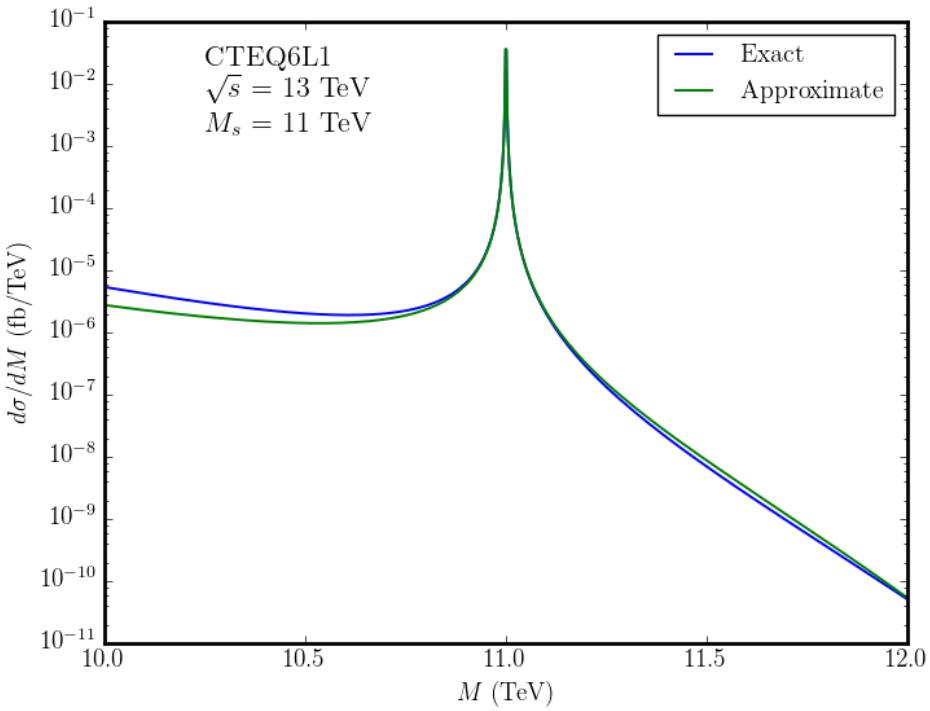

Figure 3.11: Proton-proton differential cross-section calculated from the exact (blue) and approximated (green) forms of the Veneziano factors for $M_s = 11$ TeV.

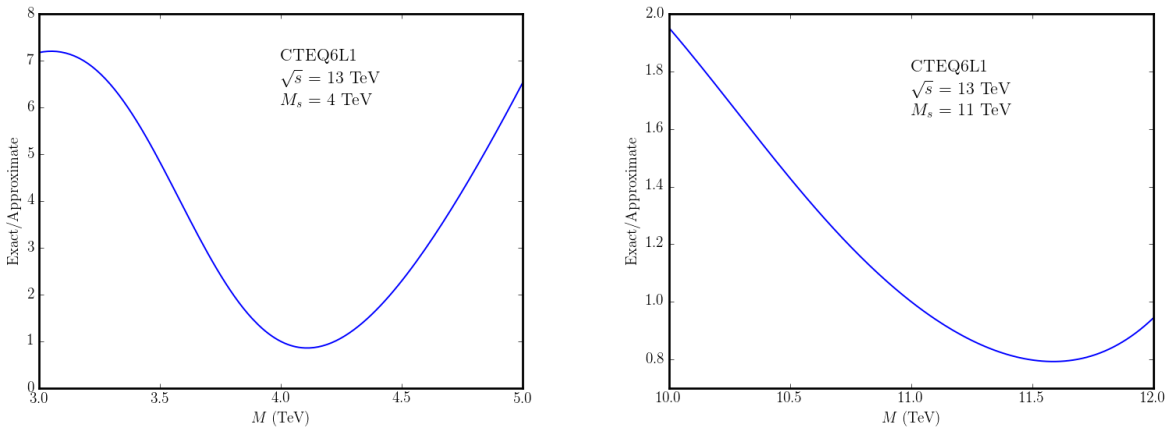

Figure 3.12: Ratios of the proton-proton differential cross-section for $M_s = 4$ TeV (left) and $M_s = 11$ TeV (right), calculated from the exact and approximated forms of the Veneziano factors.

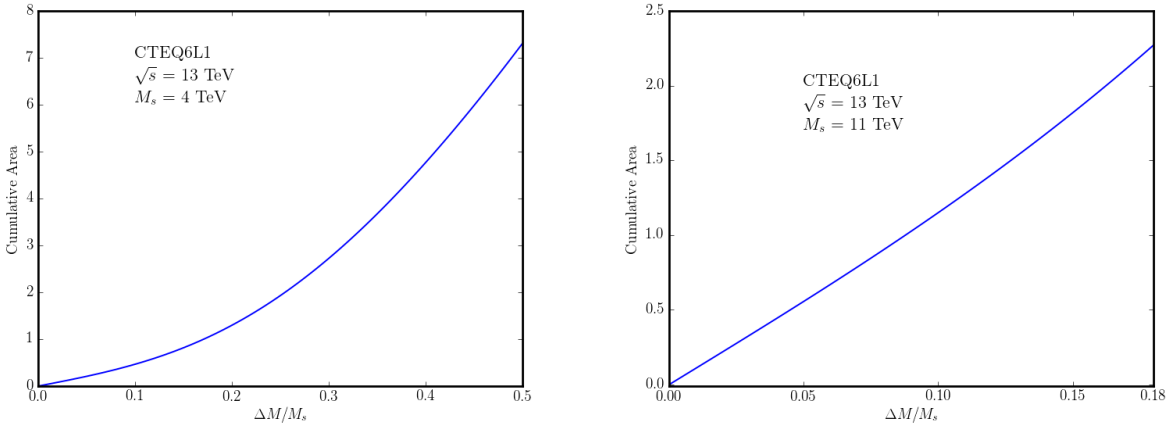

Figure 3.13: Cumulative area for $M_s = 4$ TeV (left) and $M_s = 11$ TeV (right), calculated from the ratios of the proton-proton differential cross-sections.

As can be seen in figures 3.10, 3.11 and 3.12, as the string scale increases the approximated and exact differential cross-sections get closer to each other, the ratio tends to cover a smaller range on the y-axis. The area under the curve for $M_s = 4$ TeV in figure 3.13 is approximately 1.3, while the area under the curve for $M_s = 11$ TeV is approximately 0.2.

In order to perform the discovery potential study, Chapter 5, we need to calculate the cross-sections of the resonances by integrating the approximated proton-proton differential cross-section over an invariant mass interval M. For the different string scales that are studied in chapter 5, we integrate the approximate and exact differential cross-sections over the larger invariant mass interval in table 3.1 and collect the results in table 3.2.

M_s (TeV)	M (TeV)	σ_{exact} (fb)	$\sigma_{\text{approximate}}$ (fb)	Relative Difference
7.00	[6.06, 13.00]	7.35×10^1	7.30×10^1	0.4 %
7.50	[6.60, 13.00]	2.18×10^1	2.17×10^1	0.3 %
8.00	[7.14, 13.00]	6.06	6.04	0.3 %
8.50	[7.60, 13.00]	1.54	1.53	0.2 %
9.00	[8.05, 13.00]	3.49×10^{-1}	3.48×10^{-1}	0.1 %

Table 3.2: Exact and approximated cross-sections, and the relative difference, for different string scales, calculated by integrating the exact and approximated differential cross-sections over the invariant mass interval M.

As can be seen in table 3.2, the relative difference of the cross-section, that arises due to the approximation made in the Veneziano factors, is small. The cross-section of the approximated differential cross-sections are smaller than the exact ones, which implies that there is an underestimation of 0.4 % for $M_s > 7$ TeV in the number of signal events in this approximation; the relative error in the number of events, which is the same as the relative error in the cross-sections, are collected in the last column in table 3.2.

Chapter 4

STRINGS Monte Carlo Event Generator

Using the differential cross-sections, decay widths, and the PDF sets described in the previous sections, we write a Monte Carlo event generator for the production and decay of string resonances in proton-proton collisions, STRINGS-1.00 [25]. STRINGS is also capable of producing QCD tree-level scattering amplitudes. The output of the STRINGS event generator is an LHE (Les Houches Event) file [26], which is a standard format to store the kinematic variables of the incoming and outgoing partons; LHE files can also be used to store all the particles' four-vectors after hadronization. We run the generator for different string scales and histogram the kinematic variables stored in the LHE files as a step toward the validation of STRINGS; appendix A contains the parton-level validation plots.

4.1 QCD Comparison

We use STRINGS to generate QCD tree-level events and use the particles' four-vectors in the LHE files to histogram the invariant mass distribution and compare it with results from an ATLAS paper [5]. We also use QCD dijets [27] produced by Pythia 8.212 [7], using the ATLAS set of tuned parameters [28] together with NNPDF2.3 LO [29] PDF set, to compare with QCD dijets produced by STRINGS. These tuned parameters are determined in a way that improves the modelling of QCD background.

We run the STRINGS generator with the input parameters in table 4.1 and produce the LHE files; we divided the invariant mass region [2, 8] TeV into 30 slices and generated 100,000 events in each slice. However, based on the colour confinement principle [14], partons cannot be found isolated. Thus, when the parton-parton scattering happens, the outgoing partons go through parton hadronization and decay to form stable colour-less particles, which are detected in the detector. Thus, in order to compare the QCD dijets produced by the STRINGS generator with data, we take the output LHE files and pass them to Pythia to perform the parton showering, fragmentation, hadronization, and decay. Note that, at this stage, we do not use the ATLAS tuned parameters and we just use Pythia to perform the

parton showering, fragmentation, hadronization, and decay, using an input LHE file.

When the stable particles are determined, jet reconstruction is performed to obtain the truth-level jets, i.e. no detector-related effect is considered in the jet reconstruction. Jets can be studied to give us intuition about the connection between the colour-less stable particles detected in the detectors and the underlying parton-level scattering happening in proton-proton collisions. We use the anti-k_t algorithm with `AntiKt4TruthDressedWZJets` container, with a distance parameter of $R = 0.4$ [30], to get the truth-level jets. `DressedWZ` in `AntiKt4TruthDressedWZJets` means that electrons and muons are not included in the jet. Jet-level validation plots for STRINGS are gathered in appendix B.

Using the two highest p_T jets (denoted by p_{T_1} and p_{T_2}), we calculate the invariant mass distribution. The requirements on p_{T_1}, p_{T_2} and $\eta^* = (\eta_1 - \eta_2)/2$ of the two highest p_T jets are the same as the requirements used in the ATLAS paper [5]. Figure 4.1 shows the invariant mass distribution for QCD produced by STRINGS, Pythia, and ATLAS results [5].

Proton-Proton Centre-of-Mass Energy	13 TeV
Invariant Mass Interval	M = [2, 13] TeV
Scale of the Running Coupling Constant	p_T
Number of Events (Generated by STRINGS)	3,000,000
Number of Events (Generated by Pythia)	17,986,500
PDF Set (Used by STRINGS)	CTEQ6L1
PDF Set (Used by Pythia)	NNPDF2.3 LO
Scale of the PDF Set	$Q = p_T$
$\lvert\eta_1\rvert$, $\lvert\eta_2\rvert$	< 2.5

Table 4.1: Input parameters of the Monte Carlo event generators for producing the QCD dijets.

As can be seen in figure 4.1, QCD dijets predicted by STRINGS and Pythia are different. One reason for this deviation is the choice of PDF set used by the generators, table 4.1. Another reason that the invariant mass distributions look different is probably because STRINGS contains only the leading order terms in the QCD tree-level scattering amplitude, and Pythia contains more terms. Since the generators cannot contain infinitely many terms of the perturbative expansions, they predict a QCD cross-section different from

data. Consequently, one needs to normalize the invariant mass distribution produced by any Monte Carlo event generator for QCD to data. If STRINGS or Pythia are used to estimate the background, we use the normalization factors in table 4.2. Since a large number of events are generated, table 4.1, the statistical error in normalization factors is negligible.

STRINGS/Pythia	STRINGS/ATLAS	Pythia/ATLAS
1.79	2.47	1.38

Table 4.2: Factors for normalizing STRINGS and Pythia to results from an ATLAS paper [5], and also STRINGS to Pythia, using the invariant mass range [2, 13] TeV.

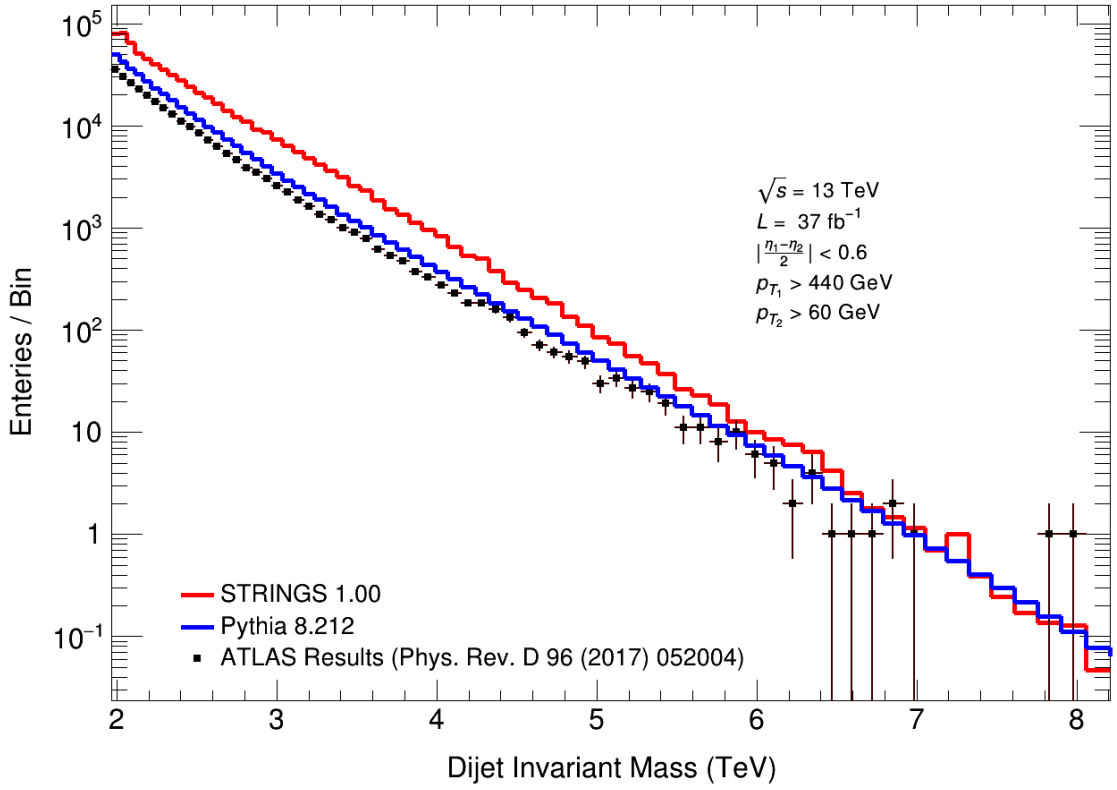

Figure 4.1: QCD comparison between STRINGS, Pythia, and data presented by ATLAS [5], using the paramters listed in table 4.1.

Figures 4.2 and 4.3 show the ratio of QCD dijets produced by STRINGS to the QCD dijets produced by Pythia and ATLAS results [5], respectively. It can be seen in figures 4.2 and 4.3 that the normalization factors collected in table 4.2 actually represent the ratio of the first few bins of the invariant mass distributions since the first few bins have larger weights in the sum, figure 4.1. Thus, depending on the invariant mass interval, we get different normalization factors. If, for example, we use an invariant mass interval $M = [6, 13]$ TeV, the normalization factor of STRINGS to data would be 1.5, rather than 2.5, figure 4.3.

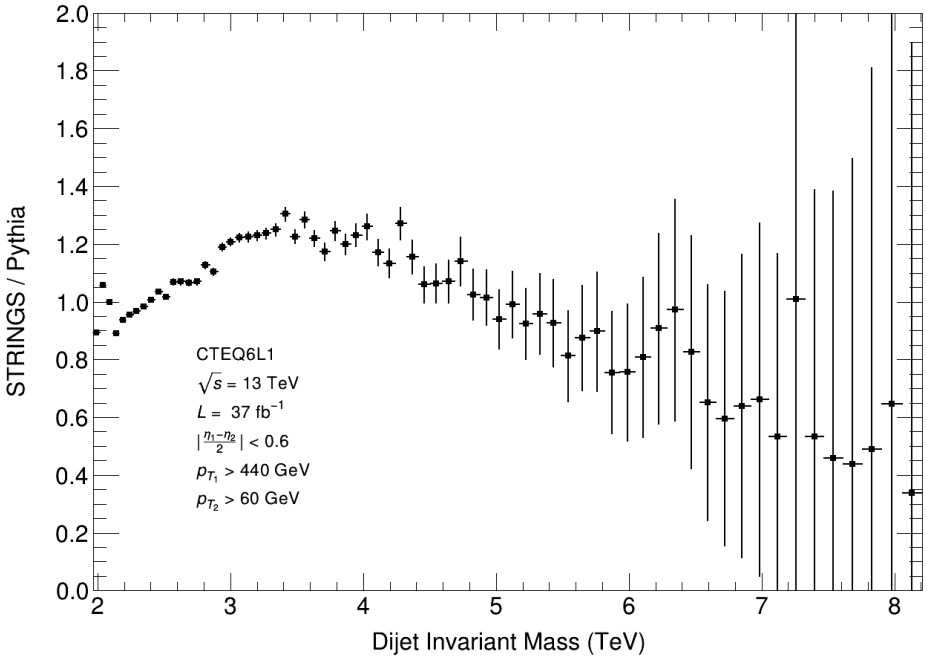

Figure 4.2: Ratio of the QCD produced by STRINGS to the QCD produced by Pythia.

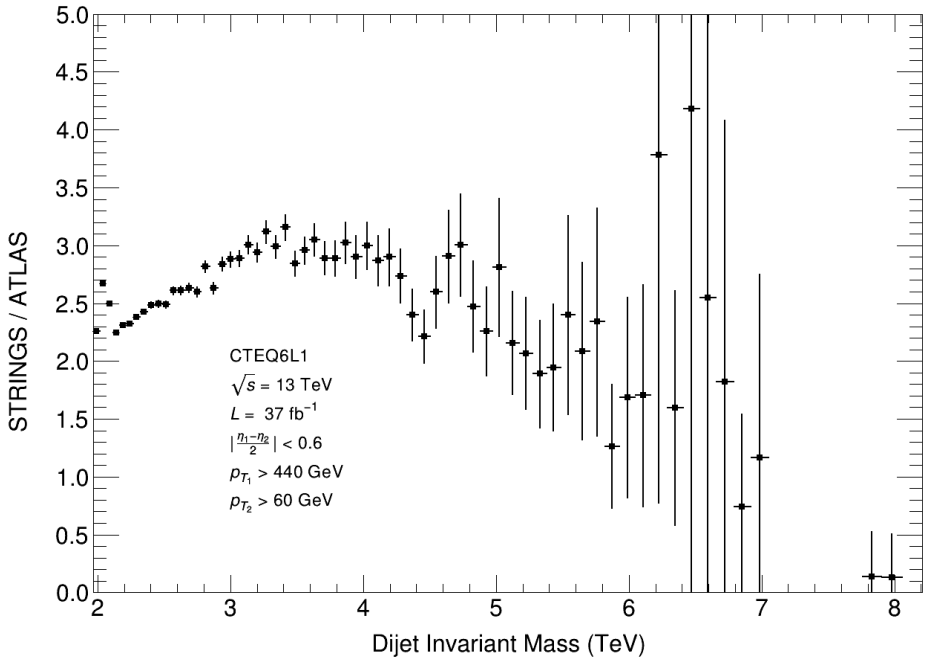

Figure 4.3: Ratio of the QCD produced by STRINGS to results from an ATLAS paper [5].

Chapter 5

Discovery Potential at the LHC

Until now, we discussed low-scale string theory and studied some features of the first string resonance. In this chapter, we study the discovery potential of the first string resonance at the LHC. Since low-scale string theory is not predicted by SM physics, it is regarded as a theory beyond the SM. In order to look for evidence of a theory beyond the SM, we need to look at the data produced in the experiments and see if there are any significant deviations from the SM physics, which, in our case, is called QCD background. In other words, we need to compare two hypotheses: 1) null hypothesis, which stands for QCD only, and 2) the signal hypothesis, which represents the resonance added to QCD, i.e. signal + background. By studying each hypothesis, we can expect to see a certain number of events, assuming that hypothesis is correct. On the other hand, data produced by colliders represent the observed number of events. Thus, by comparing the observed number of events with the expected number of events predicted by each hypothesis, we can report a discovery, which is discussed in this chapter, or set limits on the cross-sections, which is discussed in chapter 6.

We start by simulating the cross-sections predicted by low-scale string theory, and by using an integrated luminosity L, we calculate the expected number of signal events above the background as

$$N = L\sigma_s, \tag{5.1}$$

where σ_s is the cross-section of the resonance (signal). Furthermore, the expected number of background events can be calculated as

$$B = L\sigma_b, \tag{5.2}$$

where σ_b is the cross-section of the QCD (background). There are different models for quantitatively describing the statistical significance, and they are described and compared in Ref.[31]. We use the Poisson model, which suggests that the statistical significance S is described as [31]

$$S = \sqrt{2\left(\left(N+B\right)\ln\left(1+\frac{N}{B}\right)-N\right)}. \tag{5.3}$$

Note that the Poisson model [31] does not contain any uncertainty. The significance is reported in terms of the standard deviation σ of a Gaussian distribution. Conventionally, a significance of 5σ corresponds to a discovery [31].

We use the STRINGS Monte Carlo event generator to simulate the production of the first string resonance in proton-proton collisions at the LHC. Also, the QCD background is produced by STRINGS and is normalized to results from an ATLAS paper [5], using the normalization factor in table 4.2. After calculating the cross-sections, we use equations (5.1 - 5.3) to calculate the significance of the signal events over the background. Based on the conventions of reporting a discovery, we require the significance of the signal events be larger than 5 in our study. On the other hand, sometimes, while the number of signal events is small, the significance of the signal events is large. This case happens only due to a small number of background events. Thus, to make sure the number of signal events is not very small, we require the number of signal events above background N be larger than 10. Consequently, in order to report a discovery, we require two conditions:

$$N > 10, \tag{5.4}$$

$$S > 5. \tag{5.5}$$

If these conditions are satisfied, we predict an observation if the beyond SM process occurs.

5.1 Parton-Level Discovery Potential

We run the STRINGS event generator for different string scales and use the partons' four-momenta to perform the discovery potential study. Using a luminosity of 140 fb^{-1}, which approximately corresponds to the delivered LHC data for run 2, we calculate the significance of the signal events, shown in figure 5.1, by integrating the differential cross-sections over the invariant mass interval $M = [3, 13]$ TeV. Knowing that the number of signal events above the background is greater than 10 for all of the string scales in figure 5.1, the highest detectable string scale is 6.2 TeV. If we use a luminosity of 3000 fb^{-1}, string scales as high as 7.0 TeV can be probed, figure 5.2. Figure 5.3 depicts the required luminosity for satisfying the two detectability conditions, equations (5.4, 5.5), versus string scale. Each point in these plots represents a string scale that was used in the STRINGS event generator run, while linear interpolation is used to connect the points.

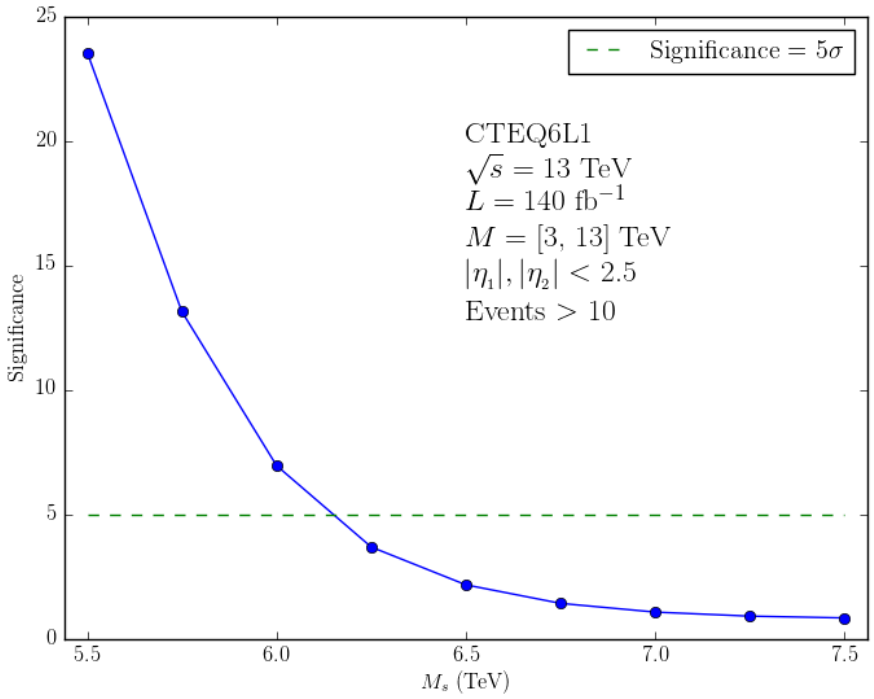

Figure 5.1: Significance of the signal events above background for different string scales using $L = 140$ fb^{-1} and requiring the number events be larger than 10.

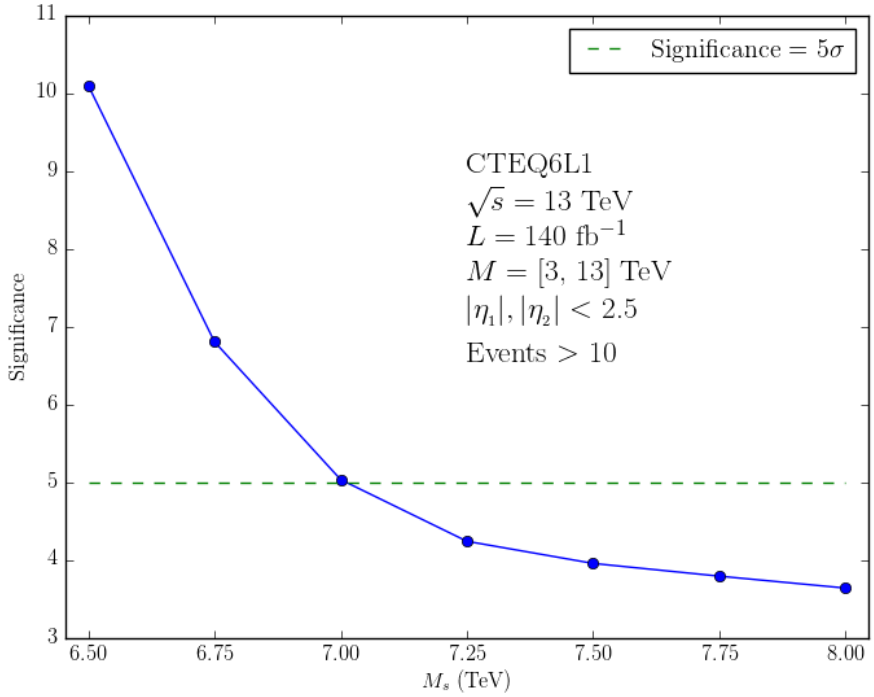

Figure 5.2: Significance of the signal events above background for different string scales using $L = 3000$ fb^{-1} and requiring the number events be larger than 10.

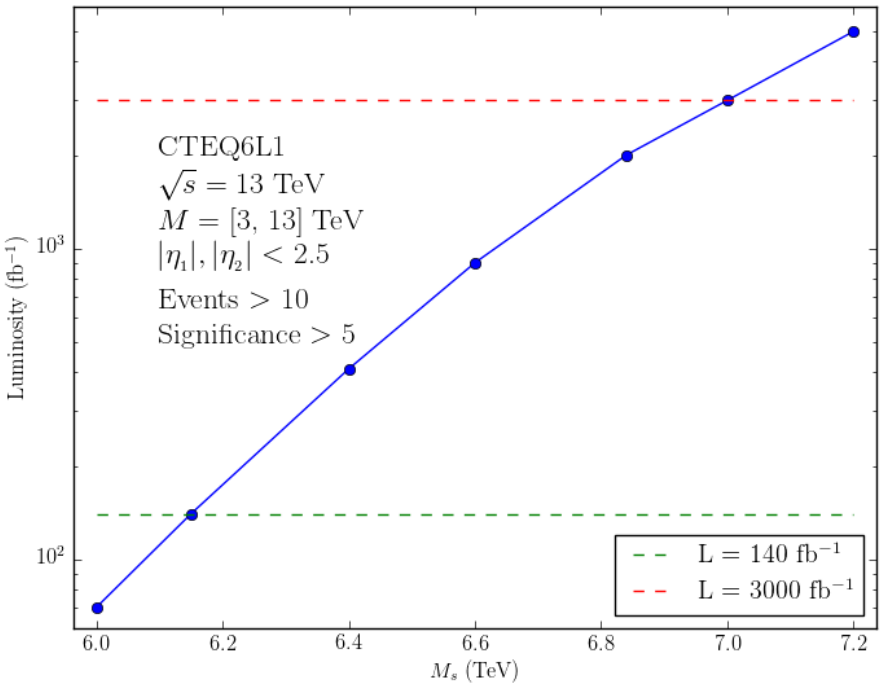

Figure 5.3: Required luminosity versus string scale for satisfying the detectability conditions, i.e. $N > 10$ and $S > 5$.

5.2 Angular Distribution Study

Until now, we studied the invariant mass distribution of the first string resonance, which indicated an excess of signal events over the QCD background. As can be seen in equations (2.4 - 2.7), the scattering amplitudes for the production of the string resonances contain the Veneziano factors, which are functions of the Mandelstam variables. However, in the QCD tree-level scattering amplitudes, the Veneziano factors are equal to 1, Chapter 2. Since Mandelstam variables are functions of the angle of the outgoing partons, the angular distribution of the string resonances is different from the angular distribution of the two-parton combination of the QCD tree-level scattering, figure 5.4.

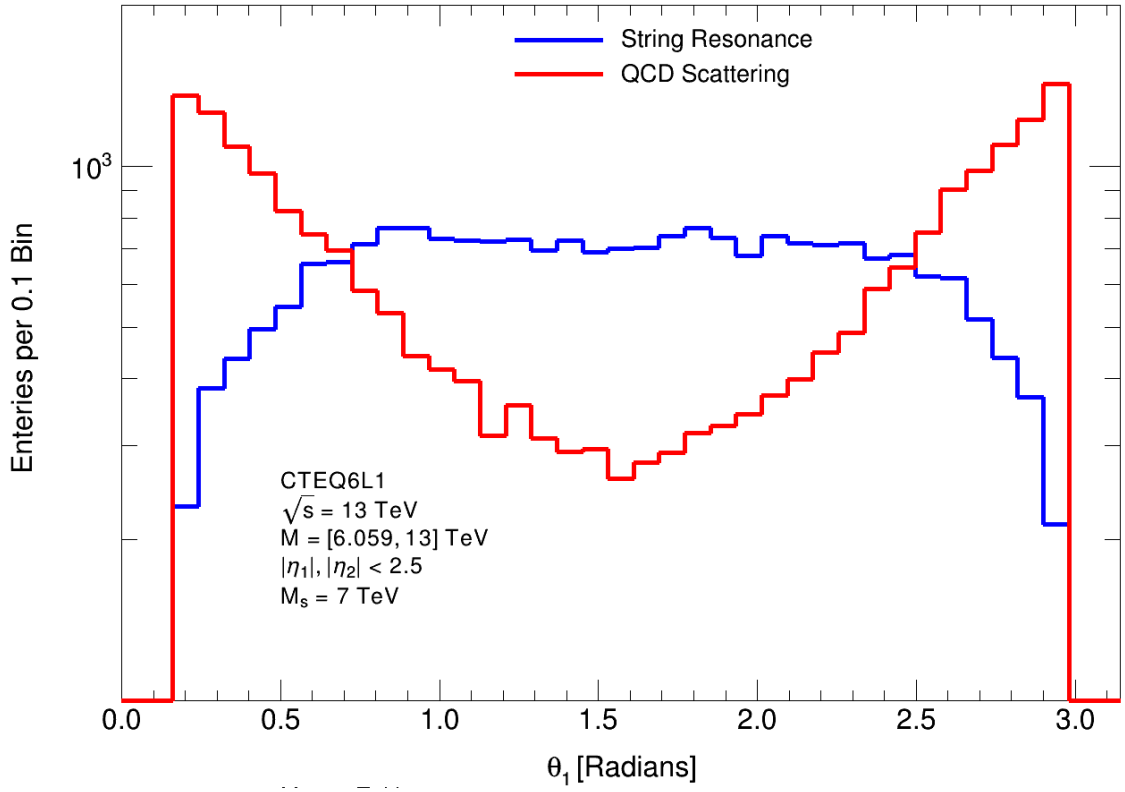

Figure 5.4: Angular distribution of an outgoing parton, in the laboratory frame, resulting from the decay of a string resonance at $M_s = 7$ TeV and QCD tree-level scattering. These histograms are normalized to 22000 events.

Since, at leading order, the QCD background is in the t-channel and the string resonances are in the s-channel, we set some requirements on the leading p_T, sub-leading p_T and pseudorapidities of the highest p_T jets [5] to suppress the t-channel contributions and reduce the QCD background. These requirements reduce the number of signal events but reduce

background more.

In the previous section we found that by using luminosities 140 fb^{-1} and 3000 fb^{-1}, the highest detectable string scales would be 6.2 TeV and 7.0 TeV. Thus, we study the effects of the requirements on p_T and η^* on the string resonances and the QCD background by running the STRINGS event generator for different string scales in [5, 8] TeV. Also, at parton-level, the transverse momentum of the outgoing partons are the same, i.e. $p_{T_1} = p_{T_2} \equiv p_T$. The best p_T requirement is approximately $M_s/2$ since the signals have a resonance at $M = M_s$, and the resonance decays into two partons, while there is no resonance in the QCD background.

We do not want to include the low-mass regions, where the QCD background is huge. Thus we require $p_T > 500$ GeV for the outgoing partons, close to the requirements in Ref. [5]. Using this p_T requirement, we vary the η^*_{max} requirement, while the detectability requirements, equations (5.4, 5.5), are satisfied, and plot the signal efficiency, background rejection and signal-to-background ratios for different string scales, figures 5.5 and 5.6.

As can be seen in figures 5.5 and 5.6, with the decrease of η^*_{max}, the signal-to-background ratio increases but signal efficiency decreases. We could use a very small value for η^*_{max}, but most of the signal events would be rejected. At $\eta^*_{\text{max}} \approx 0.6$, the signal efficiency is 0.5. Also, for $M_s = 8$ TeV, $\eta^*_{\text{max}} \approx 0.6$ results in the highest signal-to-background ratio.

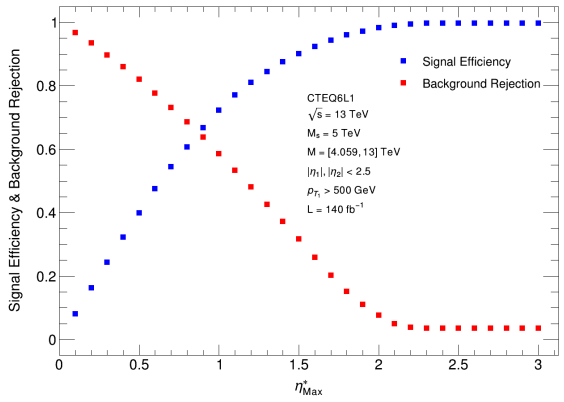

(a) Signal efficiency and background rejection for $M_s = 5$ TeV

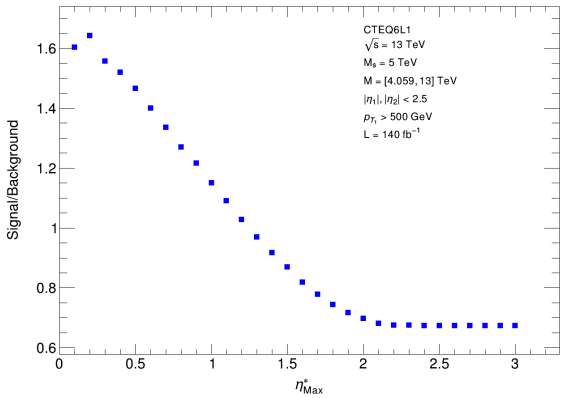

(b) Signal-to-background ratio for $M_s = 5$ TeV

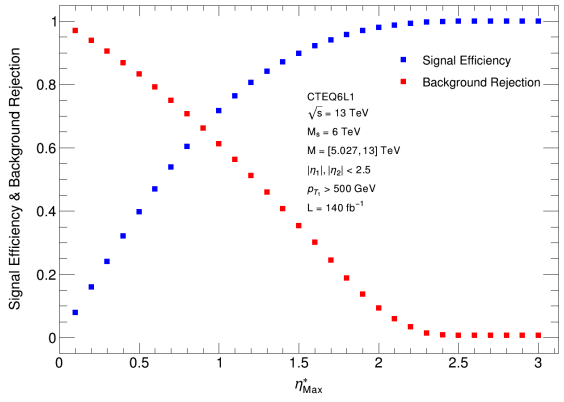

(c) Signal efficiency and background rejection for $M_s = 6$ TeV

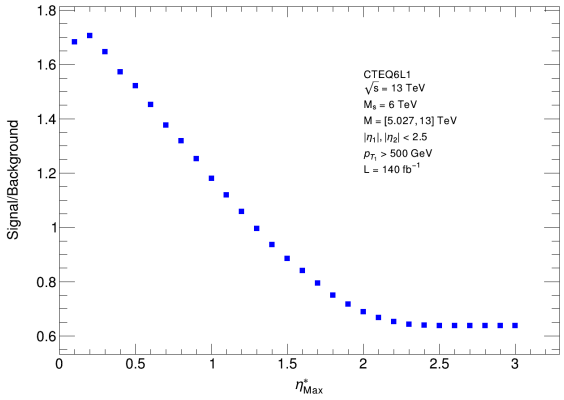

(d) Signal-to-background ratio for $M_s = 6$ TeV

Figure 5.5: a) Signal efficiency and background rejection for $M_s = 5$ TeV, b) signal-to-background-ratio for $M_s = 5$ TeV, c) signal efficiency and background rejection for $M_s = 6$ TeV and b) signal-to-background-ratio for $M_s = 6$ TeV.

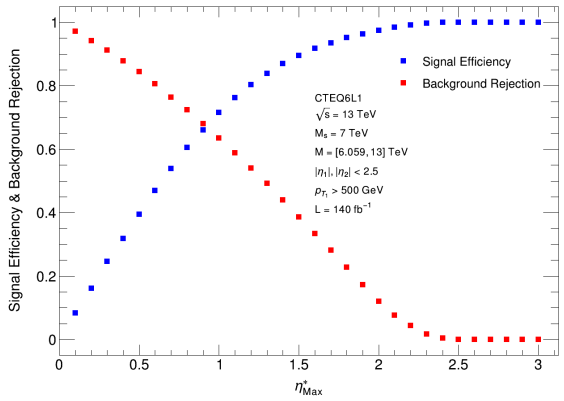

(a) Signal efficiency and background rejection for $M_s = 7$ TeV

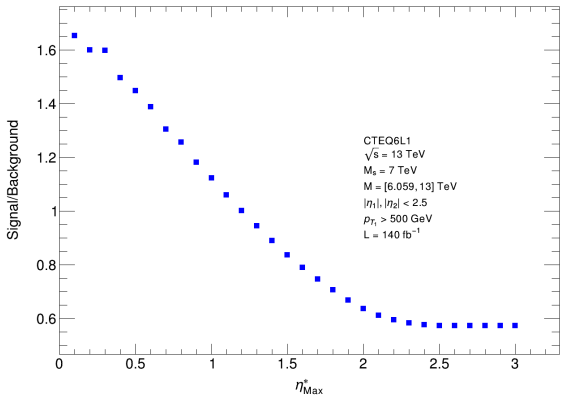

(b) Signal-to-background ratio for $M_s = 7$ TeV

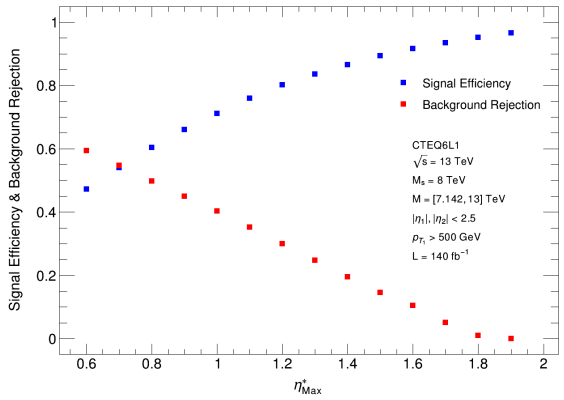

(c) Signal efficiency and background rejection for $M_s = 8$ TeV

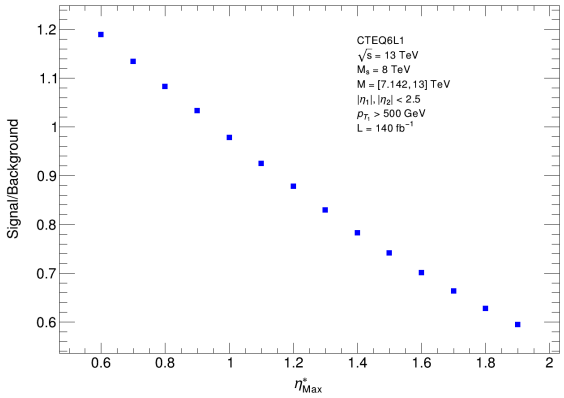

(d) Signal-to-background ratio for $M_s = 8$ TeV

Figure 5.6: a) Signal efficiency and background rejection for $M_s = 7$ TeV, b) signal-to-background-ratio for $M_s = 7$ TeV, c) signal efficiency and background rejection for $M_s = 8$ TeV and b) signal-to-background-ratio for $M_s = 8$ TeV.

5.3 Jet-Level Discovery Potential

As was discussed in Chapter 4, it would be more realistic to perform the jet-level discovery potential study. First, we run the STRINGS event generator with an invariant mass requirement that corresponds to the larger invariant mass interval in table 3.1 and generate the LHE files. We take the LHE files as input to Pythia to perform the parton showering, fragmentation, hadronization and decay. Then we perform the jet-reconstruction and get the truth-level jets, chapter 4. Using the two highest p_T jets, we construct the dijet invariant mass, figure 5.7.

Using the dijet invariant mass, we perform the discovery potential study at the jet-level. For this study, we use the QCD dijet background [27] produced by Pythia, using the ATLAS set of tuned parameters [28], to estimate the QCD background. As was discussed in the previous section, we use the requirements on p_T and η^* in Ref. [5] on the leading p_T and sub-leading p_T jets to suppress the t-channel contributions. Figure 5.8 shows the invariant mass distribution for different string scales using 140 fb^{-1} of luminosity.

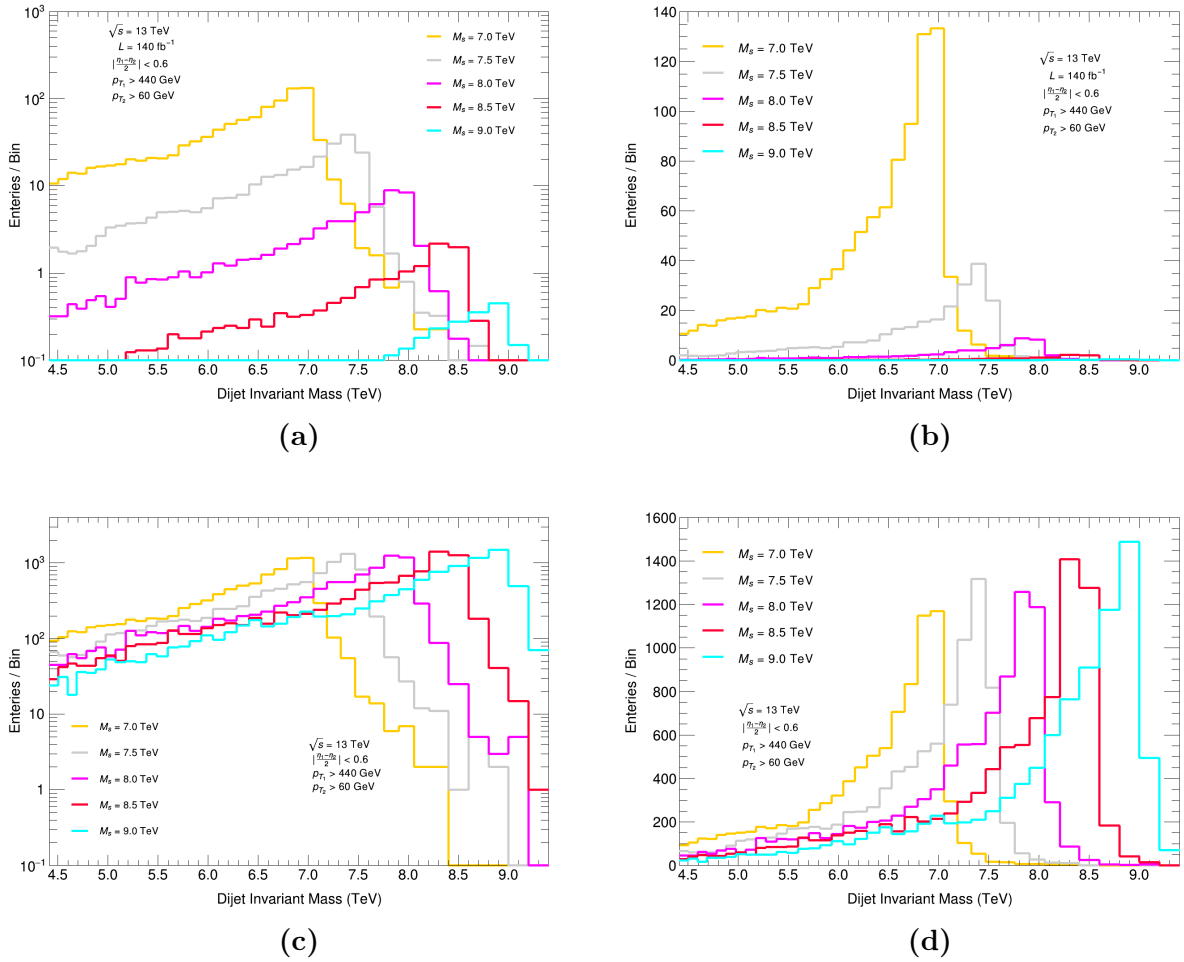

Figure 5.7: Dijet invariant mass distribution of the signal events for different string scales a) normalized by cross-section on log-scale, b) normalized by cross-section on linear-scale, c) normalized to the same number of events on log-scale, and d) normalized to the same number of events on linear-scale.

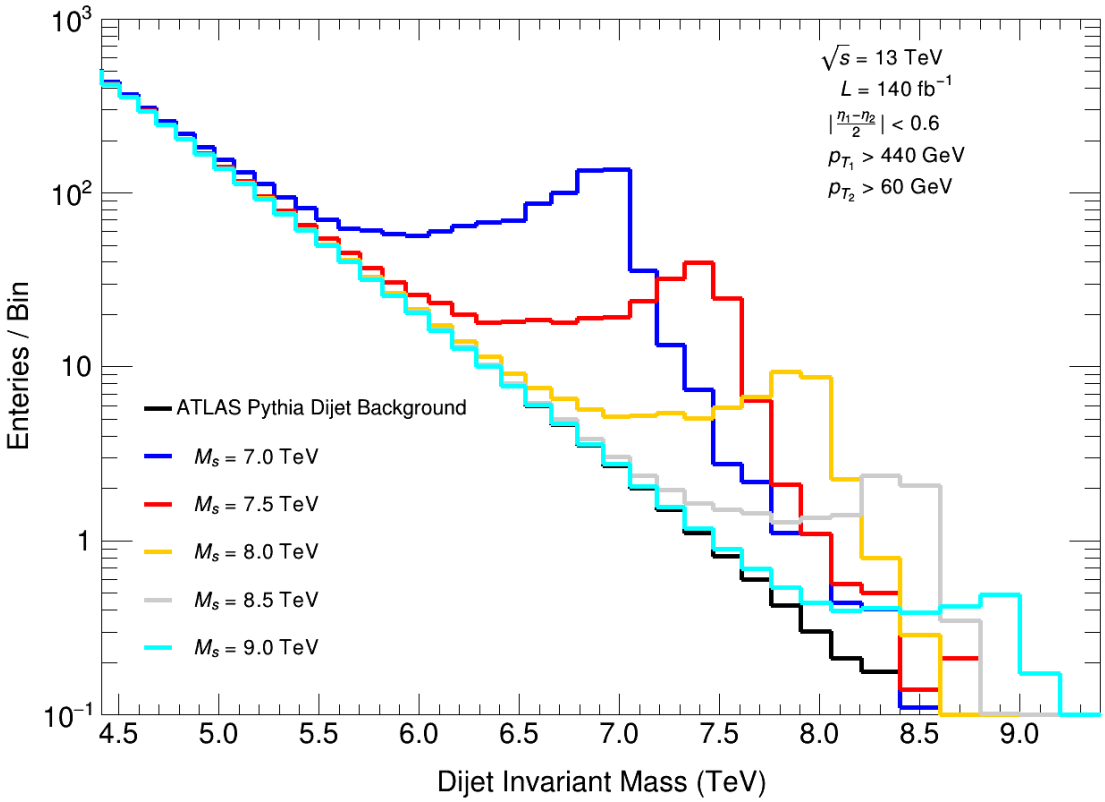

Figure 5.8: Dijet invariant mass distribution for different string scales M_s superimposed on the ATLAS Pythia dijet background normalized to data (black) [27].

Figures 5.9 and 5.10 show the number of signal events above the background and the significance of the signal events for 140 fb^{-1} of luminosity. Each point in these plots represents a string scale that was used in the STRINGS event generator run, while linear interpolation is used to connect the points. As can be seen in figure 5.10, the highest string scale that satisfies $S > 5$ is $M_s = 8.4$ TeV. On the other hand, as can be seen in figure 5.9, $M_s = 8.4$ TeV satisfies $N > 10$. Consequently, these plots indicate that by using a luminosity of 140 fb^{-1}, the highest string scale that satisfies the detectability conditions equations (5.4, 5.5) is $M_s = 8.4$ TeV. Figure 5.11 shows the three-dimensional parameter space, in which the plane at $M_s = 8.4$ TeV represents the highest string scale that satisfies the conditions on the number of events and the significance. Figure 5.12 shows the required luminosity for satisfying the detectability conditions versus string scale, which suggests that a luminosity of 3000 fb^{-1} makes the detection of string scales up to $M_s = 9.1$ TeV possible.

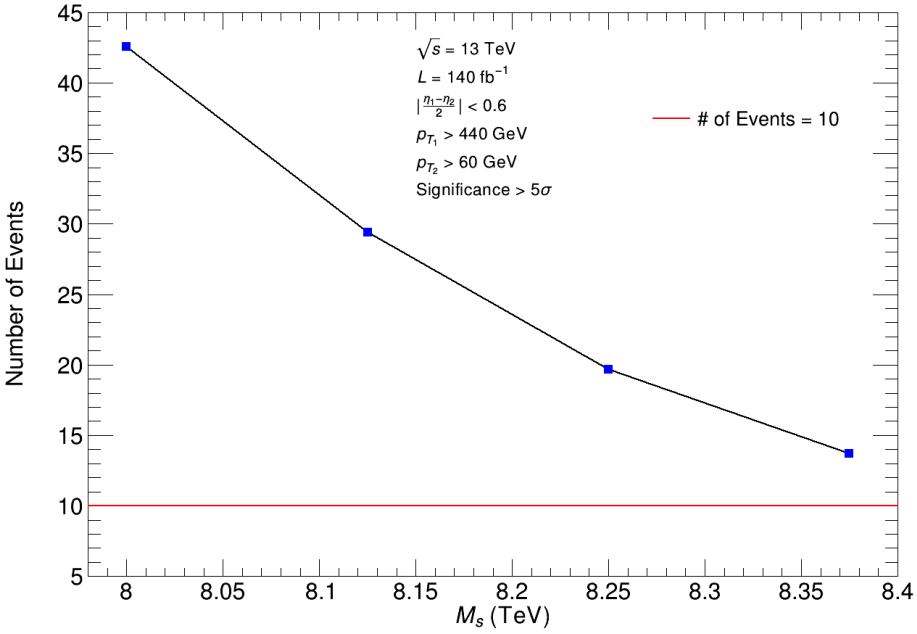

Figure 5.9: Number of signal events above background for different string scales M_s, using STRINGS dijet events as signal and ATLAS Pythia dijet background.

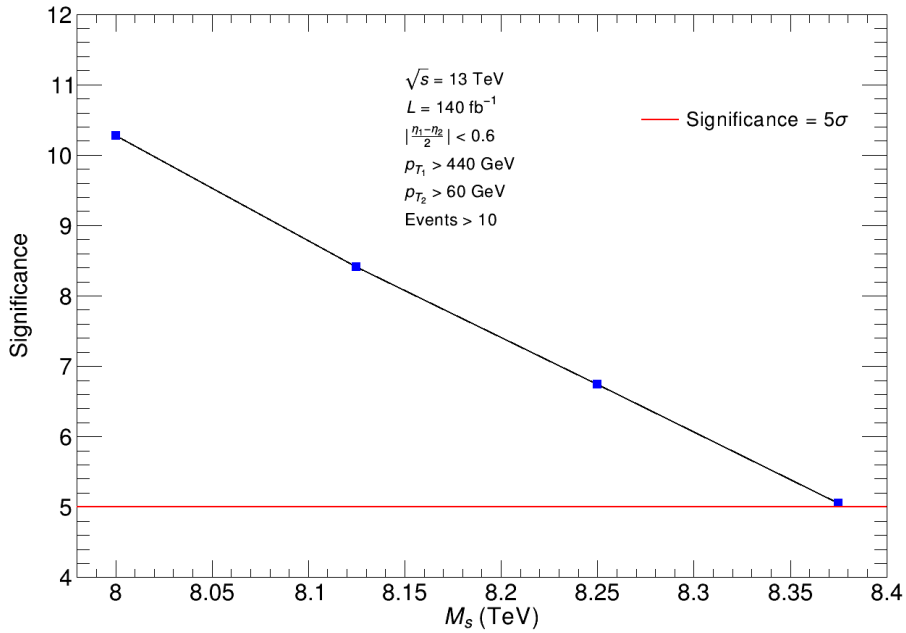

Figure 5.10: Significance of the signal events for different string scales, using STRINGS dijet events as signal and ATLAS Pythia dijet background.

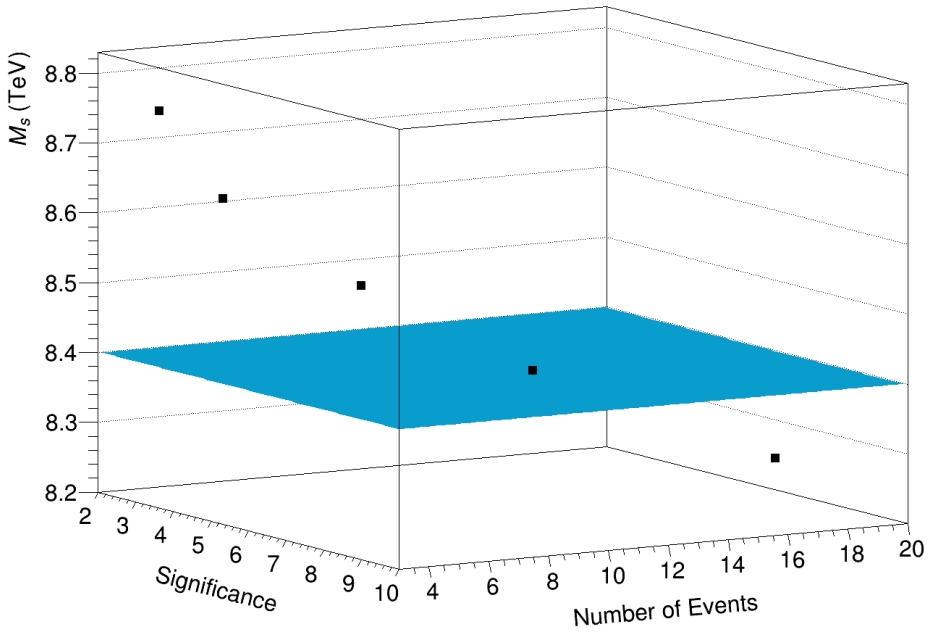

Figure 5.11: Three-dimensional parameter space for string scale, number of events N and significance S. The plane is drawn at the highest detectable ($N > 10$ and $S > 5$) string scale 8.4 TeV.

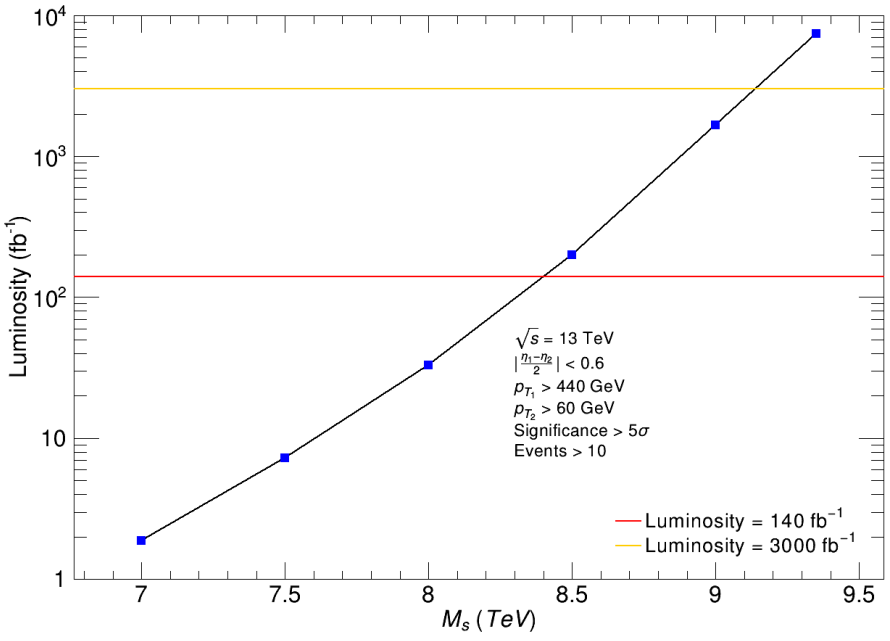

Figure 5.12: Luminosity required to satisfy the conditions $N > 10$ and $S > 5$ versus string scale.

5.4 Acceptance at the Truth-Level Jets

In the previous sections, we justified the requirements on p_T and η^* from Ref. [5] and used them to perform the discovery potential study at the truth-level jets. Now we are going to set these requirements one by one and study the signal acceptance, for different string scales for truth-level jets. Using the invariant mass requirement [M_{min}, 13 TeV] from table 3.1, we run the STRINGS event generator and use the LHE files as an input to Pythia to perform the parton showering, fragmentation, hadronization and decay. Then we perform the jet-reconstruction and get the truth-level jets, chapter 4. Using the leading p_T and sub-leading p_T jets, we construct the dijet invariant mass distribution.

Table 5.1 contains the acceptance A of the signal events for truth-level jets using the requirements described in the previous section. These values are accumulative acceptance, meaning that the acceptance presented in the first column is calculated using the requirements $|\eta_1|, |\eta_2| < 2.5$, $p_{T_1} > 440$ GeV, and $p_{T_2} > 60$ GeV together with $\eta^* < 0.6$. Also, the acceptance presented in the second column is calculated using all of the requirements mentioned above together with $M > M_{\text{min}}$. The percentage of the acceptance due to the requirements applied before the requirements in this table, i.e. $|\eta_1|, |\eta_2| < 2.5$, $p_{T_1} > 440$ GeV, and $p_{T_2} > 60$ GeV, is more than 98% for all of the string scales. On the other hand, D in table 5.1 is the absolute non-accumulative acceptance calculated using the requirement in each column. A and D calculated using the requirements on η_1, η_2, p_{T_1}, and p_{T_2} are not presented in table 5.1 since they have a 2% reduction on the acceptance.

The requirement on the pseudo-rapidity of the outgoing jets is $|\eta_1|, |\eta_2| < 2.5$, which is the requirement set on the pseudo-rapidities of the outgoing partons. This produces a bias, since the reconstructed jets might have a rapidity more than 2.5. Since the truth-level dijet invariant mass in smeared out, we set a requirement on the invariant mass, [M_{min}, 13 TeV] from table 3.1, which is indicated in the last column in table 5.1. Figure 5.13 shows the acceptance of the signal events after requiring all of the requirements in table 5.1.

M_s (TeV)		η^*	M
4.0	A	51 %	36 %
	D	51 %	72 %
4.5	A	51 %	36 %
	D	51 %	69 %
5.0	A	50 %	35 %
	D	50 %	68 %
5.5	A	50 %	34 %
	D	50 %	66 %
6.0	A	50 %	33 %
	D	49 %	62 %
6.5	A	49 %	32 %
	D	50 %	60 %
7.0	A	49 %	31 %
	D	50 %	59 %
7.5	A	49 %	30 %
	D	50 %	57 %
8.0	A	49 %	29 %
	D	50 %	56 %
8.5	A	48 %	27 %
	D	49 %	53 %
9.0	A	48 %	26 %
	D	49 %	52 %
9.5	A	47 %	24 %
	D	49 %	51 %
10.0	A	47 %	22 %
	D	48 %	49 %

Table 5.1: Accumulative acceptance A of the signal events at the truth-level jets. The requirements are as follows: $\eta^* < 0.6$, and $M > M_{\rm min}$. D is the absolute non-accumulative acceptance of the requirement in each column. The percentage of the acceptance due to the requirements applied before the requirements in this table, i.e. $|\eta_1|, |\eta_2| < 2.5$, $p_{T_1} > 440$ GeV, and $p_{T_2} > 60$ GeV, is more than 98% for all of the string scales.

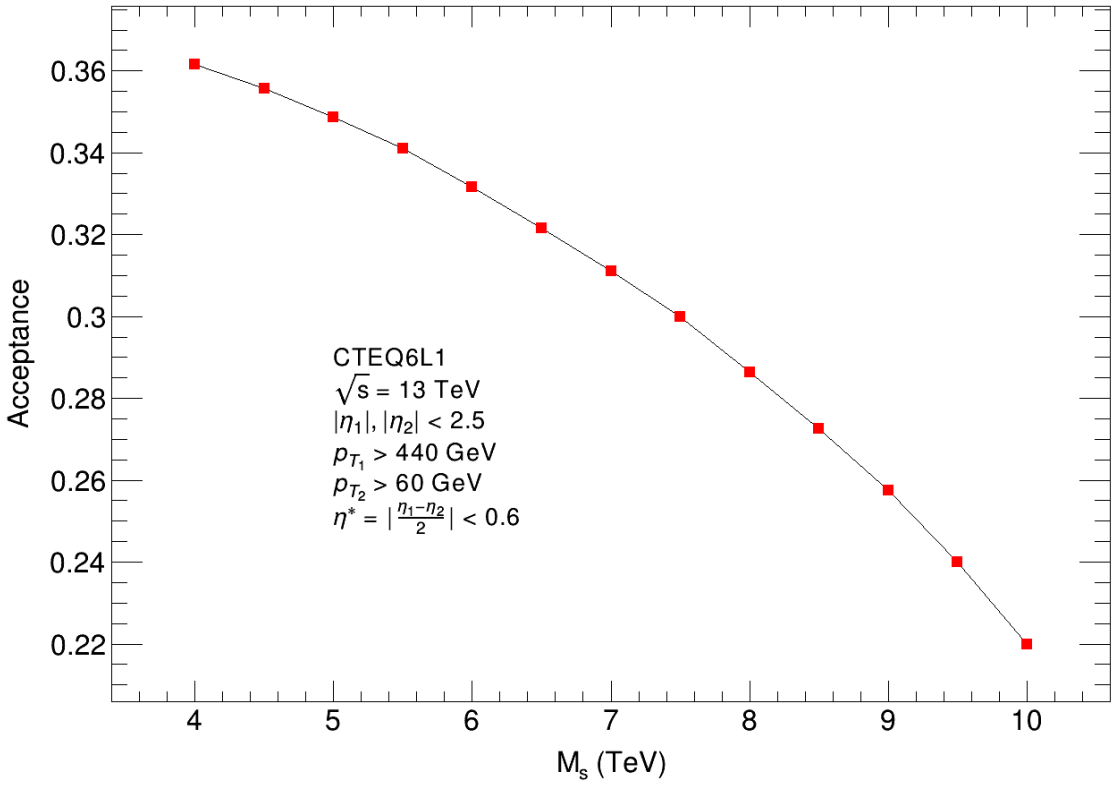

Figure 5.13: Acceptance of the signal events after requiring all of the requirements used in Ref.[5] for different string scales.

As can be seen in table 5.1, the requirement responsible for the shape of the acceptance in figure 5.13 is the invariant mass requirement.

Chapter 6

Cross-Section Upper Limits and String Scale Lower Limits

In the previous section, we studied the discovery potential of the first string resonance at the LHC. Using a luminosity of 140 fb^{-1}, we determined the highest detectable string scale is 8.4 TeV. However, if no signal is observed and we have a data sample, we can set limits on the cross-section of the signal and find lower limits on the string scale for our model. In other words, this limit setting would exclude the regions in which the string resonances are not present in data. For expressing the incompatibility of data with the signal hypothesis, the idea of the confidence level (CL) is used [32]. CL quantifies the level at which the signal lies in the data. Conventionally, for the limit studies, 95% CL, which corresponds to a p-value of 5%, is required to exclude a region in which the signal is not present. This chapter is dedicated to the calculation of upper limits on the signal cross-section and lower limits on the string scale.

6.1 String Scale Lower Limit Using CMS Results

Before we perform our own cross-section limit study, we use the CMS results for the cross-section limit [36] for q^*, i.e. the quark excited state, which has a Breit-Wigner shaped amplitude, and use the cross-section of the first string resonance to find a lower limit on the string scale. As can be seen in figure 6.1, using a luminosity of 36 fb^{-1}, the region below 7.4 TeV is excluded with 95% CL.

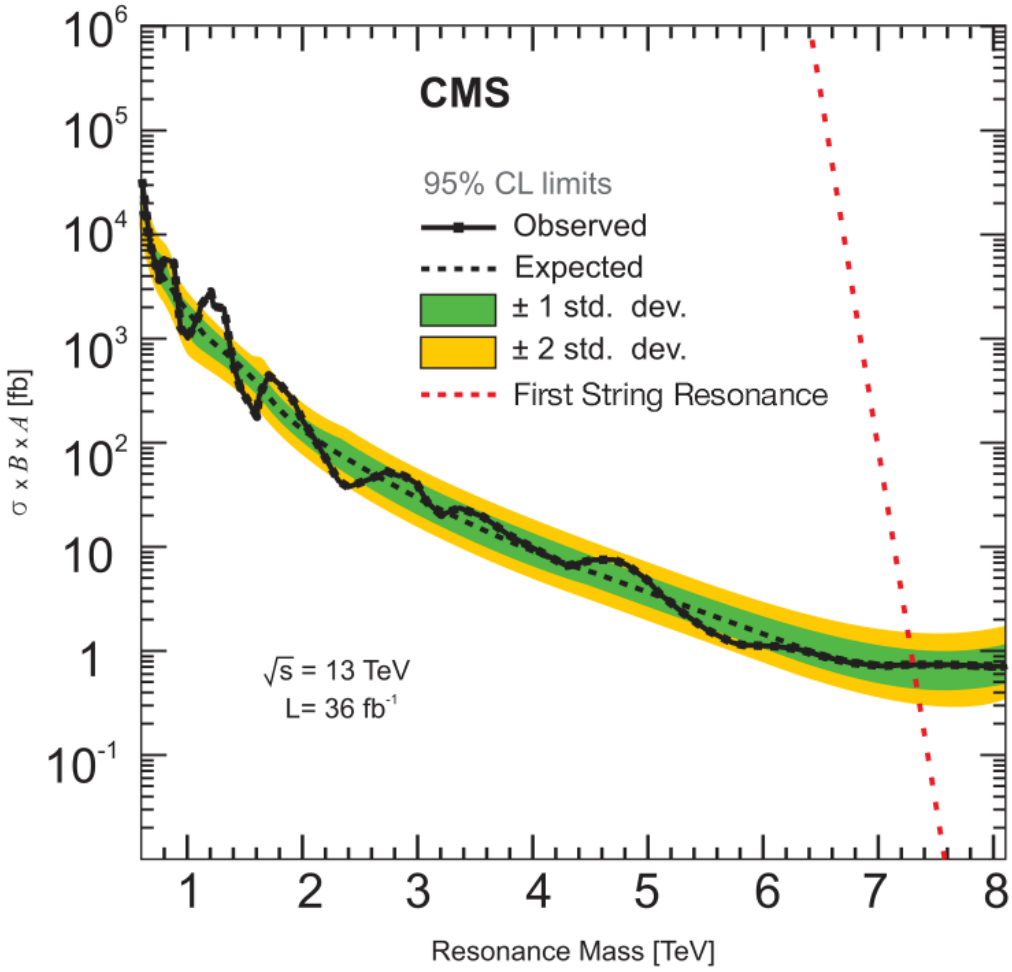

Figure 6.1: Cross-section limit result by CMS [36] and the cross-section of the first string resonance (red dashed line).

6.2 Cross-Section Limit Setting Using ATLAS Results

In this sections, we use results from an ATLAS paper [5] and perform the cross-section limit study, which can be used to set lower limits on the string scale. To perform the cross-section limit study, we need to compare the number of events predicted by background only and signal + background hypotheses with the number of observed events resulting from the experiment and set limits on the number of signal events. We use results from an ATLAS paper [5] with an integrated luminosity of 37 fb^{-1} as the observed data and the ATLAS background estimate and uncertainty [5]. The ATLAS background estimate is a fit to the results in an ATLAS paper [5], figures 6.2. Thus, there are two systematic uncertainties related to the ATLAS background estimate: one uncertainty is due to the choice of the fit function, and the other is due to the fit parameters [5]. These uncertainties are symmetric

and since they are independent, they are added in quadrature. As can be seen in figure 6.2, the total uncertainty on the ATLAS background estimate is very small.

After a limit on the number of signal events N is set, it can be converted to a limit on the cross-section of the signal σ_s by using the following equation:

$$\sigma_s = \frac{N}{L\, A\, \eta\, B}, \tag{6.1}$$

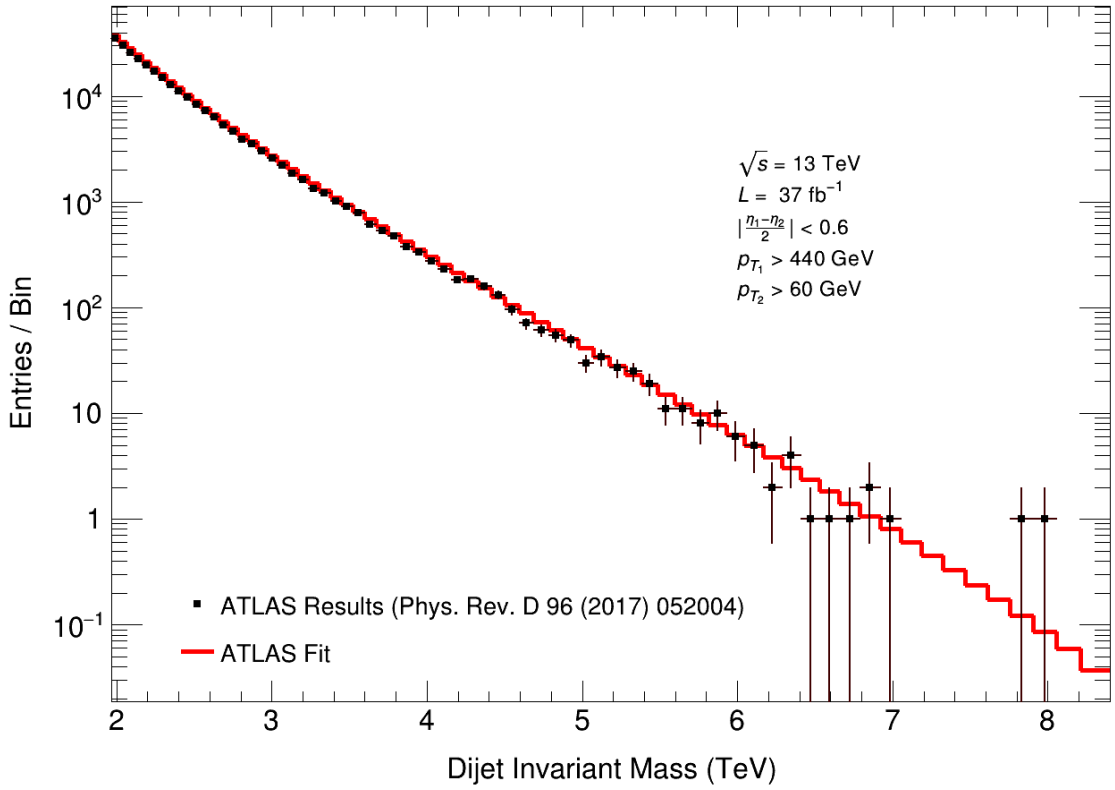

Figure 6.2: Results from an ATLAS paper [5] (black points) and the background estimate (red histogram), which is a fit to the data. This is taken from [5]. Note the error bars on the histogram.

where η is the efficiency due to the detector effects, A is the acceptance and B is the total resonance branching ratio, which is one in our case, because we consider all of the subprocesses inclusively. L is the luminosity recorded by ATLAS with a systematic uncertainty of 2%, Ref.[5]. We take $\eta = 1 \pm 0$ since we do not consider the detector effects, chapter 5. As can be seen in Ref.[5], if the detector effects are considered, the value of η would be approximately 0.97. Thus, changing η by 3% in equation (6.1) would scale the cross-section by 97%. Since we are neglecting detector effects, we omit any possible systematic uncertainty on the signal acceptance. Furthermore, we use a large number of signal events, of the order of a million, to calculate the acceptance, which makes the statistical uncertainty of the acceptance negligible, chapter 5. Consequently, we neglect any uncertainty on the signal acceptance as well.

The modified frequentist CL_s method [33, 34] is used to set upper limits on the number of signal events. In this method, the number of events predicted by the background only and signal + background hypotheses are modelled with Poisson distributions and systematic uncertainties are modelled with normal distributions. Thus, if background and luminosity are determined with a systematic uncertainty as $B = B_0 \pm \sigma_B$ and $L = L_0 \pm \sigma_L$, respectively, the full probability distribution of the number of signal + background events, i.e. signal hypothesis, is written as a convolution of the normalized distribution functions, representing the systematic errors, with the Poisson distribution function, representing the probability distribution of the number of events, as [33]

$$\begin{aligned} P_{N+B}(x) &= \int_{B_0-\sigma_B}^{B_0+\sigma_B} dB \int_{L_0-\sigma_L}^{L_0+\sigma_L} dL\, P(x; N+B)\, G(L; L_0, \sigma_L)\, G(B; B_0, \sigma_B) \\ &= \int_{B_0-\sigma_B}^{B_0+\sigma_B} dB \int_{L_0-\sigma_L}^{L_0+\sigma_L} dL\, \frac{e^{-(N+B)}\,(N+B)^x}{x!} \frac{1}{\sqrt{2\pi}\,\sigma_L}\, e^{\dfrac{-(L-L_0)^2}{2\sigma_L^2}} \\ &\quad \cdot \frac{1}{\sqrt{2\pi}\,\sigma_B}\, e^{\dfrac{-(B-B_0)^2}{2\sigma_B^2}}, \end{aligned} \tag{6.2}$$

where N and B are the number of signal and background events, respectively, which are related to the cross-section and luminosity through equation (6.1). Similarly, the full probability distribution of the number of background events, i.e. background only hypothesis, can be written as [33]

$$
\begin{aligned}
P_B(x) &= \int_{B_0-\sigma_B}^{B_0+\sigma_B} dB \int_{L_0-\sigma_L}^{L_0+\sigma_L} dL\, P(x;B)\, G(L;L_0,\sigma_L)\, G(B;B_0,\sigma_B) \\
&= \int_{B_0-\sigma_B}^{B_0+\sigma_B} dB \int_{L_0-\sigma_L}^{L_0+\sigma_L} dL\, \frac{e^{-B}\, B^x}{x!} \frac{1}{\sqrt{2\pi}\,\sigma_L}\, e^{\dfrac{-(L-L_0)^2}{2\sigma_L^2}} \frac{1}{\sqrt{2\pi}\,\sigma_B}\, e^{\dfrac{-(B-B_0)^2}{2\sigma_B^2}}.
\end{aligned} \tag{6.3}
$$

The $\mathrm{CL_s}$ method states that if the observed number of events N_{obs} are less than the expected number of events given by the signal hypothesis, a p-value CL_{N+B} is defined as [33]

$$
CL_{N+B} = \int_0^{N_{\mathrm{obs}}} P_{N+B}(x)\, dx, \tag{6.4}
$$

which represents the probability of observing N_{obs} or less, given that the signal hypothesis is correct. To exclude a signal from a region, and not the signal + background (signal hypothesis), a p-value for the case of signal only needs to be defined. In order to do so, a p-value for the null (background only) hypothesis is defined as [33]

$$
CL_B = \int_0^{N_{\mathrm{obs}}} P_B(x)\, dx, \tag{6.5}
$$

which represents the probability of observing N_{obs} or less, given that the null hypothesis is correct. By using CL_{N+B} and CL_B, we can define a p-value as [33]

$$
CL_s = \frac{CL_{N+B}}{CL_B}. \tag{6.6}
$$

which is used for the signal exclusion. This means that if $CL_s = 5\%$, the signal hypothesis is excluded with 95% CL [35].

In order to calculate the p-values and set a limit on the number of signal events, using the procedure defined above, we generate 40,000 pseudo-experiments for each M_s using the probability distribution of the background only and signal hypotheses. In this procedure, we use the cut-and-count method, i.e. for each string scale we set requirements on the invariant mass [M_{min}, 13 TeV] from table 3.1, p_T and η^* from Ref. [5] and count the number of events that satisfy these requirements. Then by varying the number of signal events N, we find a N that yields $CL_s = 5\%$.

Afterwards, equation (6.1) together with the values for acceptance calculated in chapter 5, are used to convert the limit on N to a limit on the signal cross-section times acceptance, figure 6.3, or cross-section, figure 6.4. Note that the limit calculation on $\sigma \times A$ is model-independent since there is no signal information in the limit. As can be seen in figure 5.13, since the acceptance drops only 0.12 over $M_s = [4, 10]$ TeV, the shape of $\sigma \times A$ and σ does not differ significantly in figures 6.3 and 6.4.

The solid black lines in figures 6.3 and 6.4 give the lower limit with $CL_s = 5\%$, due to any physics beyond the SM that might exist in the observed data. The black dashed line is the average (or expected) value of CL_s assuming the background only hypothesis is true and there is no signal. The black dashed line is a measure of how good an experiment would exclude a signal from a region if the signal is not present [33]. Thus, the difference between these two line in figures 6.3 and 6.4 comes from the fact that the ATLAS background estimate and the results from an ATLAS paper [5] are not exactly the same in figure 6.2. 1σ (green) and 2σ (yellow) bands around the expected 95% upper limit line are the error bands, which imply that the observed 95% upper limit line should lie in the green (yellow) band for approximately 68% (95%) of the time.

As can be seen in figure 6.3, the 95% CL cross-section times acceptance starts from 10 fb at $M_s = 4$ TeV and drops two orders of magnitude over the range $M_s = [4, 8]$ TeV.

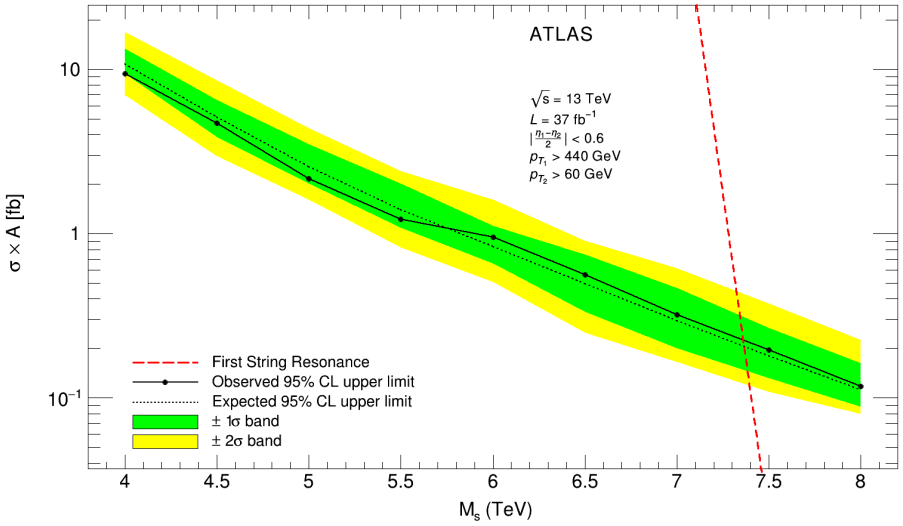

Figure 6.3: The expected (black dashed) and observed (solid black) 95% CL limits on the signal production cross-section times acceptance versus the string scale. The green and yellow bands represent one and two standard deviations from the expected limit, respectively. The red dashed line indicates the cross-section of the string resonance for different string scales.

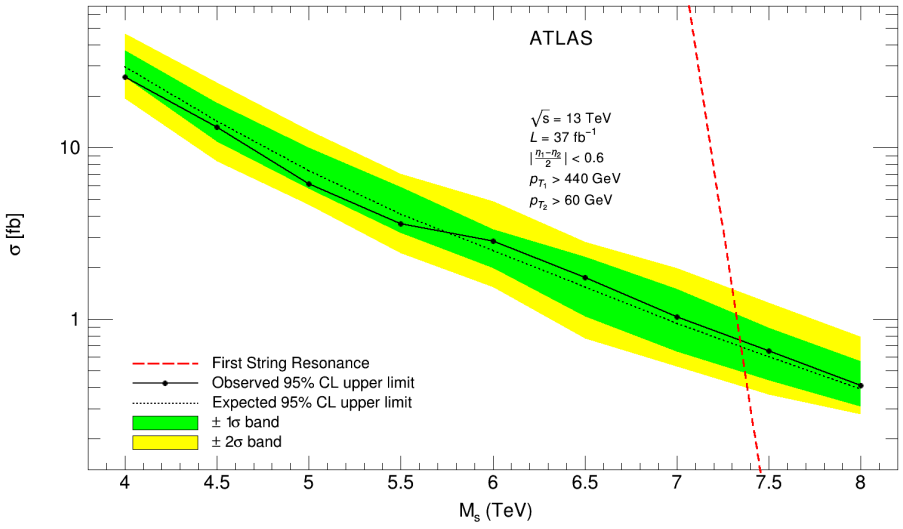

Figure 6.4: The expected (black dashed) and observed (solid black) 95% CL limits on the signal production cross-section versus the string scale. The green and yellow bands represent one and two standard deviations from the expected limit, respectively. The red dashed line indicates the cross-section of the string resonance for different string scales.

After setting a limit on the signal cross-section, we use the STRINGS event generator to find the expected number of signal events resulted from our model for different string scales. If the expected number of signal events, which is predicted by STRINGS for a string scale, is larger than the number of signal events predicted by the CL_s method, that has $CL_s = 5\%$, we exclude the region below the string scale with 95% CL. The red dashed line in figures 6.3 and 6.4 is the cross-section of the signal events for our model, calculated by STRINGS. As can be seen, in the region $M < 7.4$ TeV, the cross-section of the first string resonance is above the observed 95% upper limit, which implies that the first string resonances do not exist in this region with 95% CL.

Chapter 7

Summary

The string scale of string theory corresponds to energies far beyond accessible energies by any collider on the Earth. However, in the D-branes formulation of the string theory, in large extra dimensions, the string scale can be of the order of a few TeV, which makes it possible to check for the signatures of string states in colliders. We utilized the cross-sections and decay widths of the low-scale string resonances to write a Monte Carlo event generator for the production and decay of string resonances in proton-proton collisions, STRINGS-1.00. Requiring two conditions on the number of signal events N above background ($N > 10$) and the significance S of the signal events ($S > 5$), we estimate the discovery potential for string resonances at the LHC. We used the STRINGS event generator and performed a study at parton level. We also performed the discovery potential using truth-level jets; table 7.1 gathers the highest string scales that satisfy the detectability conditions.

L (fb^{-1})	M_s (TeV)		
	$N > 10$	$S > 5$	$(N > 10)$ & $(S > 5)$
140	8.5	8.4	8.4
3000	9.4	9.1	9.1

Table 7.1: Highest string scales M_s that satisfy the required detectability conditions, using different luminosities L.

Assuming no acceptance or efficiency uncertainty, we performed a cross-section limit setting study and excluded the region $M_s < 7.4$ TeV, in which, with 95% CL, the first string resonance is not present in the results from an ATLAS paper [5] with an integrated luminosity of 37 fb^{-1}. The 95% CL cross-section times acceptance lower limit starts from 10 fb at M_s = 4 TeV and drops two orders of magnitude over the range M_s = [4, 8] TeV. Furthermore, we used cross-section limit result by CMS to exclude the region below 7.4 TeV with 95% CL, which is the same as our result. On the other hand, using a luminosity of 140 fb^{-1}, we found that the detection of the string resonances with $M_s < 8.4$ TeV is still possible, table 7.1,

which means that it is still possible to see the first string resonance in the region [7.4, 8.4] TeV.

References

[1] N. Arkani-Hamed, S. Dimopoulos and G.R. Dvali, The Hierarchy Problem and New Dimensions at a Millimeter, Phys. Lett. B 429 (1998) 263, [ArXiv:hep-ph/9803315].

[2] I. Antoniadis, N. Arkani-Hamed, S. Dimopoulos and G. R. Dvali, New Dimensions at a Millimeter to a Fermi and Superstrings at a TeV, Phys. Lett. B 436 (1998) 257, [ArXiv:hep-ph/9804398].

[3] M. R. Garousi and R. C. Myers, Superstring Scattering from D-Branes, Nucl. Phys. B 475 (1996) 193, [ArXiv:hep-th/9603194].

[4] A. Hashimoto and I. R. Klebanov, Decay of Excited D-branes, Phys. Lett. B 381 (1996) 437, [ArXiv:hep-th/9604065].

[5] ATLAS Collaboration, Search for New Phenomena in Dijet Events Using 37 fb^{-1} of pp Collision Data Collected at $\sqrt{\text{s}} = 13$ TeV with the ATLAS Detector, Phys. Rev. D 96 (2017) 052004, [ArXiv:1703.09127 [hep-ex]].

[6] I. Antoniadis, The Physics of Extra Dimensions, Lect. Notes Phys. 720:293-321 (2007), [ArXiv:0512182 [hep-ph]].

[7] T. Sjöstrand, S. Mrenna and P. Skands, A Brief Introduction to PYTHIA 8.1, Jour. High Energy Phys. 05 (2006) 026, Comput. Phys. Comm. 178 (2008) 852, [ArXiv:0710.3820 [hep-ph]].

[8] D. De-Chang *et al.*, String Resonances at Hadron Colliders, Phys. Rev. D 90 (2014) 066013, [ArXiv:1407.8120 [hep-ph]].

[9] ATLAS Collaboration, Search for Strong Gravity in Multijet Final States Produced in Proton-Proton Collisions at $\sqrt{\text{s}} = 13$ TeV, Jour. High Energy Phys. 03 (2016) 026, [ArXiv:1512.02586 [hep-ex]].

[10] C.D. Hoyle *et al.*, Sub-millimeter Tests of the Gravitational Inverse-square Law, Phys. Rev. D 70 (2004) 042004, [ArXiv:hep-ph/0405262].

[11] D. Lust, S. Stieberger and T.R. Taylor, The LHC String Hunter's Companion, Nucl. Phys. B 808 (2009) 1, [ArXiv:0807.3333 [hep-th]].

[12] D. Lust, O. Schlotterer, S. Stieberger and T. Taylor, The LHC string hunter's companion (II): Five-Particle Amplitudes and Universal Properties, Nucl. Phys. B 828 (2010) 139, [ArXiv:0908.0409 [hep-th].

[13] E. Dudas and J. Mourad, String Theory Predictions for Future Accelerators, Nucl. Phys. B 575 (2000) 3, [ArXiv:hep-th/9911019].

[14] C. Patrignani *et al.*, Particle Data Group, Chin. Phys. C 40 (2016) 100001 and 2017 update, [pdg.lbl.gov].

[15] T. Regge, Introduction to Complex Orbital Momenta, Nuovo Cim. 14 (1959) 951.

[16] L. A. Anchordoqui, H. Goldberg, T. R. Taylor, Decay Widths of Lowest Massive Regge Excitations of Open Strings, Nucl. Phys. B 828 (2010) 139, [ArXiv:0908.0409 [hep-th].

[17] M. Hashi, N, Kitazawa, Signatures of Low-Scale String Models at the LHC, Jour. High Energy Phys. 02 (2012) 050, [ArXiv:1110.3976 [hep-ph]].

[18] E. Askanazi, K. Holcomb and S. Liuti, Self-Organizing Maps Parametrization of Deep Inelastic Structure Functions with Error Determination, [ArXiv:1309.7085 [hep-ph]].

[19] A. Buckley *et al.*, LHAPDF6: Parton Density Access in the LHC Precision Era, Eur. Phys. J. C 75 (2015) 132, [ArXiv:hep-ph/1412.7420].

[20] H. L. Lai, *et al.*, New Parton Distributions for Collider Physics, Phys. Rev. D 82 (2010) 074024, [ArXiv:1007.2241 [hep-ph]].

[21] S. Dulat, *et al.*, New Parton Distribution Functions from a Global Analysis of Quantum Chromodynamics, Phys. Rev. D 93 (2016), 033006, [ArXiv:1506.07443 [hep-ph]].

[22] P. M. Nadolsky, *et al.*, Implications of CTEQ Global Analysis for Collider Observables, Phys. Rev. D 78 (2008) 013004, [ArXiv:0802.0007 [hep-ph]].

[23] E. Eichten, I. Hinchliffe, K. D. Lane and C. Quigg, Supercollider Physics, Rev. Mod. Phys. 56 (1984) 579.

[24] S. Chatrchyan, *et al.* [The CMS Collaboration], Search for Narrow Resonances Using the Dijet Mass Spectrum in pp Collisions at $\sqrt{s} = 8$ TeV, Phys. Rev. D 87 (2013) 114015, [ArXiv:1302.4794 [hep-ex]].

[25] P. Vakilipourtakalou, D. Gingrich, Monte Carlo Event Generator For the Production and Decay of String Resonances in Proton-Proton Collisions, [ArXiv:1811.07458[hep-ph]], [strings.hepforge.org].

[26] J. Alwall, *et al.*, A Standard Format for Les Houches Event Files, Comput. Phys. Commun. 176 (2007) 300, [ArXiv:hep-ph/0609017].

[27] Z. Marshall, Re-defining the Standard QCD Di-Jet Samples, CERN, Geneva, Tech. Rep. ATL. COM. PHYS. 992 (2011), [Available: cds.cern.ch/record/1370089?].

[28] [ATLAS Collaboration], ATLAS Run 1 Pythia8 tunes, CERN, Geneva, Tech. Rep. ATL. PHYS. PUB. 021 (2014), [Available: cds.cern.ch/record/1966419].

[29] R. D. Ball, *et al.*, Parton Distributions with LHC Data, Nucl. Phys. B 867 (2013) 244, [ArXiv:1207.1303 [hep-ph]].

[30] M. Cacciari, *et al.*, The Anti-k_t Jet Clustering Algorithm, Jour. High Energy Phys. 0804 (2008) 063, [ArXiv:0802.1189 [hep-ph]].

[31] W. Buttinger, M. Lefebvre, Formulae for Calculating Significance in a Counting Experiment. [Online]. Available: [https://cds.cern.ch/record/2643488?ln=en], [https://cernbox.cern.ch/index.php/s/Qxngvi0Rt2NbASi].

[32] LHC Higgs Combination Group, Procedure for the LHC Higgs Boson Search Combination in Summer 2011, Technical Report CMS-NOTE-2011-005, ATL-PHYS-PUB-2011-11, 2011.

[33] T. Junk, Confidence Level Computation for Combining Searches With Small Statistics, Nucl. Instr. Meth. A 434 (1999) 435, [ArXiv:hep-ex/9902006].

[34] A. L. Read, Presentation of search results: The CL_s Technique, Jour. Phys. G 28 (2002) 2693.

[35] G. Cowan, *et al.*, Asymptotic Formulae for Likelihood-Based Tests of new Physics, Eur. Phys. Jour. C 71 (2011) 1554, [Erratum: Eur. Phys. J. C 73 (2013) 2501], [ArXiv:1007.1727[physics.data-an]].

[36] [CMS Collaboration], Search for narrow and broad dijet resonances in proton-proton collisions at $\sqrt{s} = 13$ TeV and constraints on dark matter mediators and other new particles, Jour. High Energy Phys. 08 (2018) 130, [ArXiv:1806.00843 [hep-ex]].

Appendix A

Parton-level validation plots for STRINGS-1.00

Parameters:

13000	Centre of Mass Energy (GeV)
22000	Number of Generated Events by STRINGS
8000	String Scale (GeV)
7142	Minimum Invariant Mass (GeV)
13000	Maximum Invariant Mass (GeV)
2.5	Upper Bound for the Rapidity of the Outgoing Partons
cteq6l1	PDF Set of the LHAPDF
8000	Scale at Which the PDF Set is Evaluated (GeV)
-1	Running Coupling Constant (alpha_s without 4*pi Factor)
8000	Scale at Which the Running Coupling is Calculated (GeV)
0.005	Mass of the Down Quark (GeV)
0.002	Mass of the Up Quark (GeV)
0.001	Mass of the Strange Quark (GeV)
1.27	Mass of the Charm Quark (GeV)
4.4	Mass of the Bottom Quark (GeV)
172.0	Mass of the Top Quark (GeV)
false	(Disabled) Production of QCD tree-level diparton
true	(Enabled) Production of First String Resonance
false	(Disabled) Production of Second String Resonance
true	(Enabled) gg $\rightarrow$ gg Subprocess (ID = 1)
true	(Enabled) gg $\rightarrow$ qqbar Subprocess (ID = 2)
true	(Enabled) gq $\rightarrow$ gq Subprocess (ID = 3)
true	(Enabled) gqbar $\rightarrow$ gqbar Subprocess (ID = 4)
true	(Enabled) qqbar $\rightarrow$ gg Subprocess (ID = 5)
false	(Disabled) gg $\rightarrow$ gGamma Subprocess (ID = 6)
false	(Disabled) gq $\rightarrow$ qGamma Subprocess (ID = 7)

A.1 Kinematic Variables of First Incoming Parton

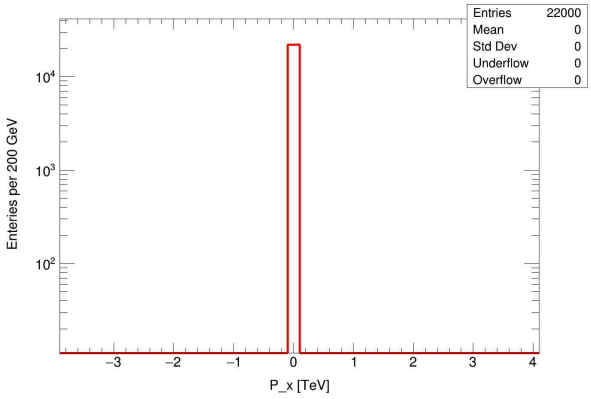

(a)

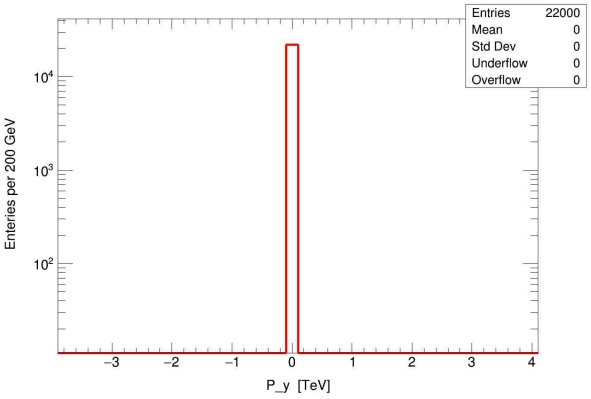

(b)

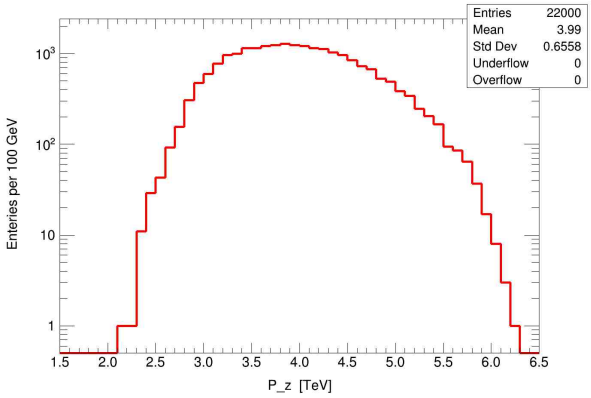

(c)

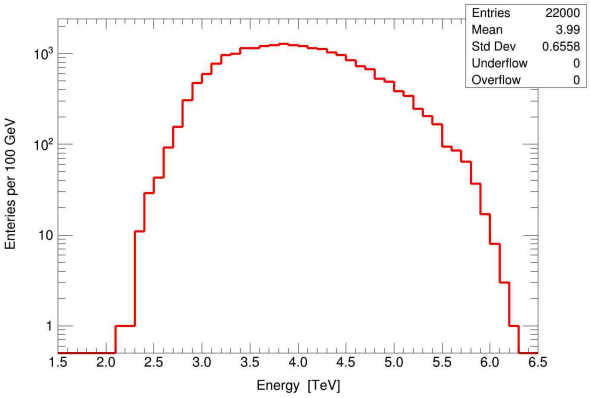

(d)

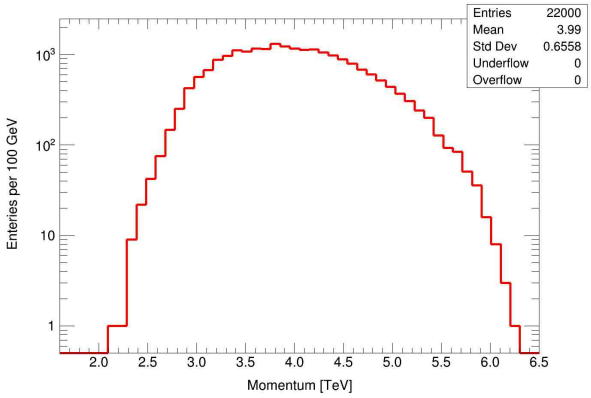

(e)

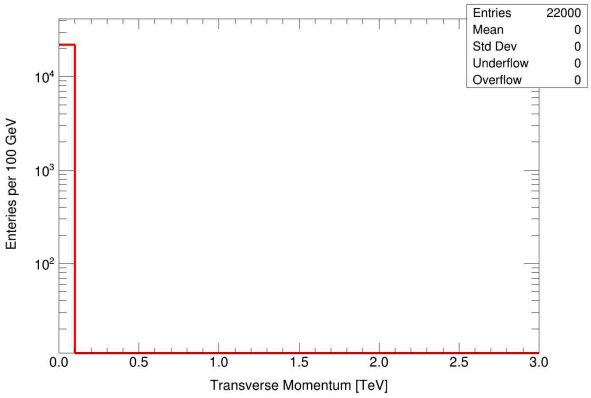

(f)

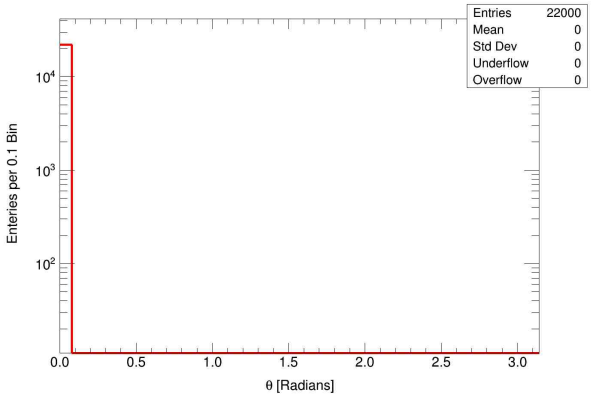
Entries 22000
Mean 0
Std Dev 0
Underflow 0
Overflow 0
Enteries per 0.1 Bin
10^4
10^3
10^2
0.0
0.5
1.0
1.5
2.0
2.5
3.0
θ [Radians]

(g)

A.2 Kinematic Variables of Second Incoming Parton

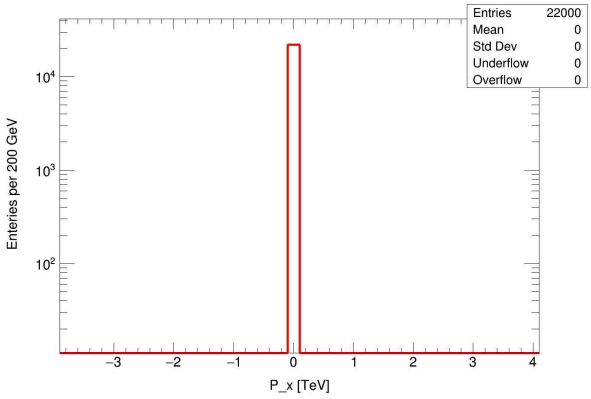

(a)

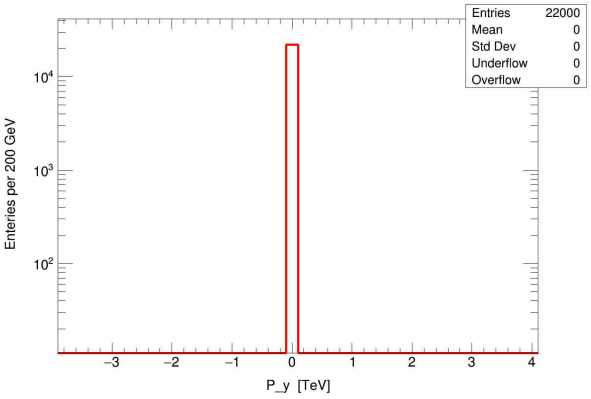

(b)

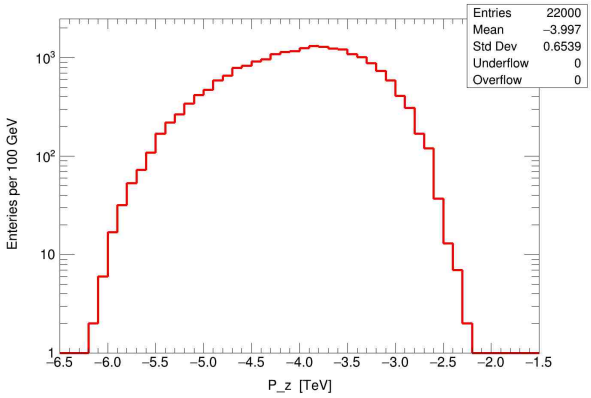

(c)

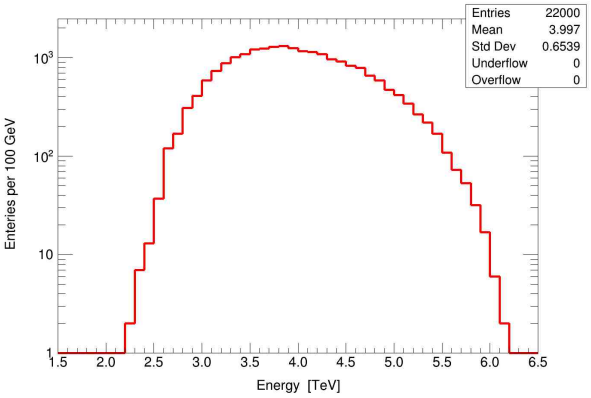

(d)

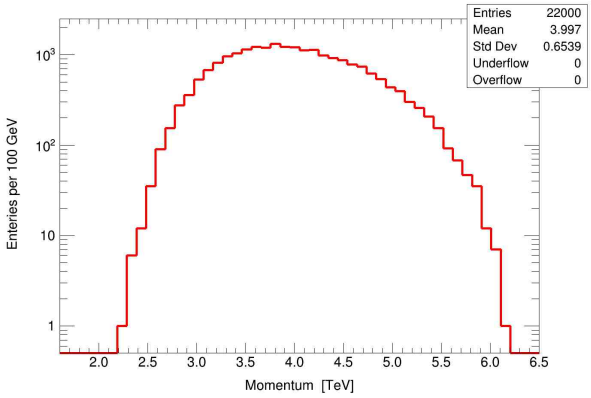

(e)

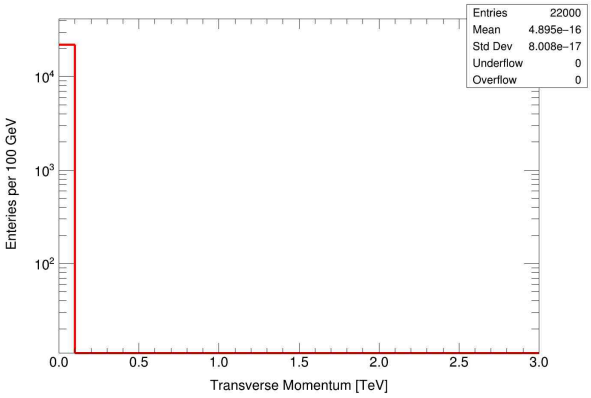

(f)

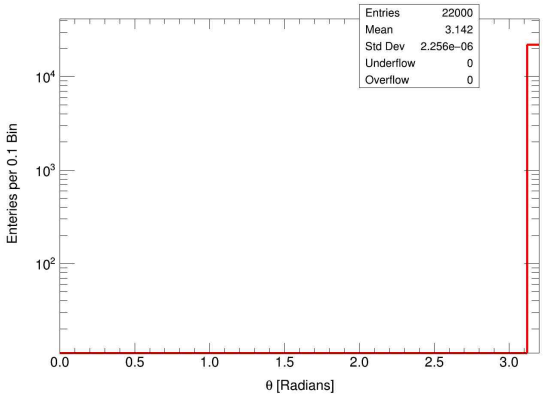
Entries 22000
Mean 3.142
Std Dev 2.256e−06
Underflow 0
Overflow 0
Enteries per 0.1 Bin
10^4
10^3
10^2
0.0
0.5
1.0
1.5
2.0
2.5
3.0
θ [Radians]

(g)

A.3 IDs of the Incoming and Outgoing Partons

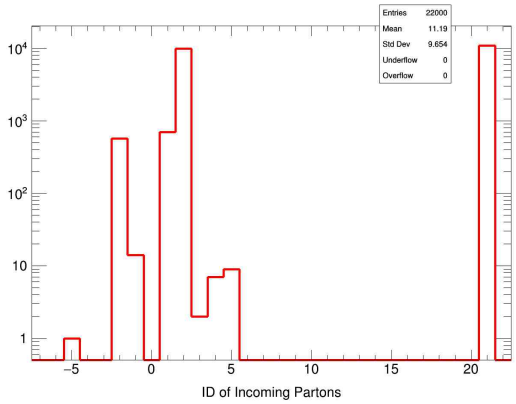

(a) IDs of Incoming Partons

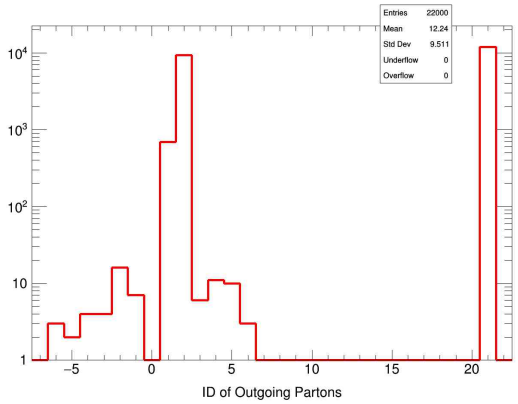

(b) IDs of Outgoing Partons

A.4 Kinematic Variables of First Outgoing Parton

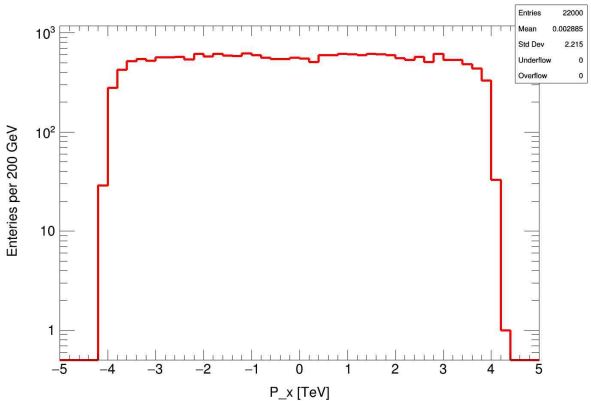

(a)

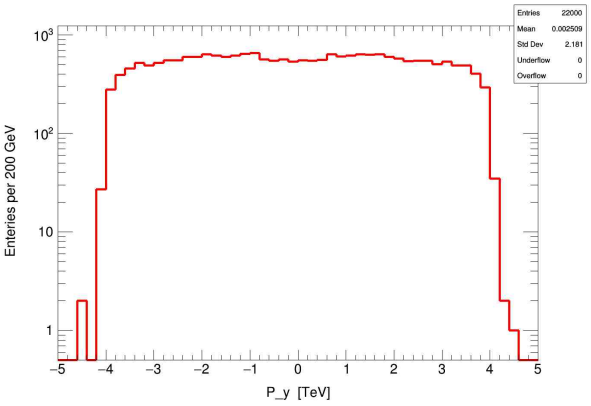

(b)

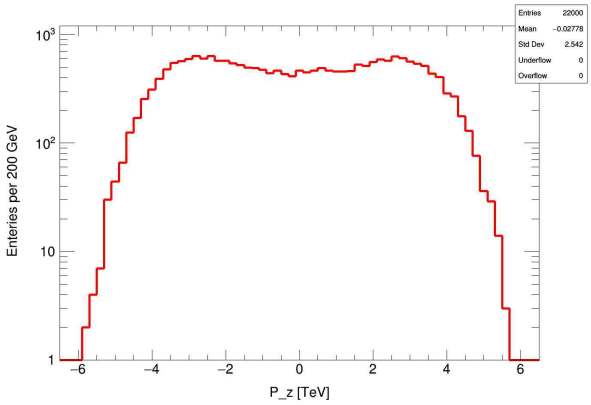

(c)

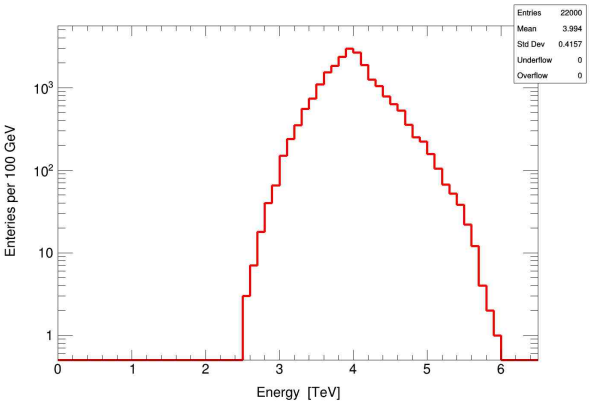

(d)

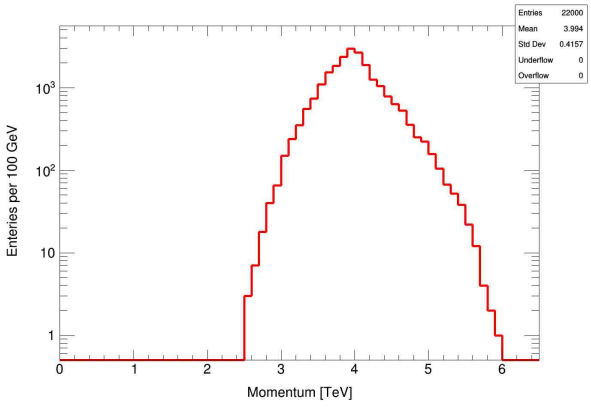

(e)

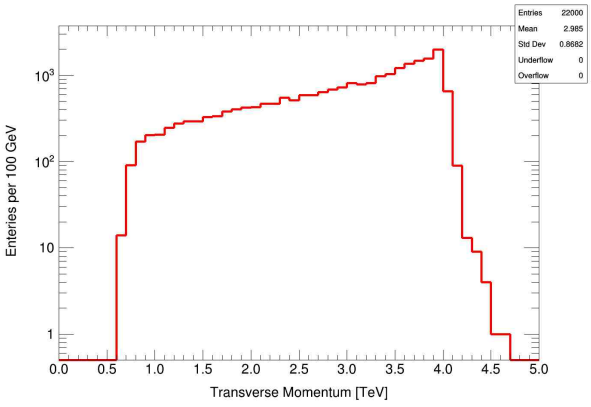

(f)

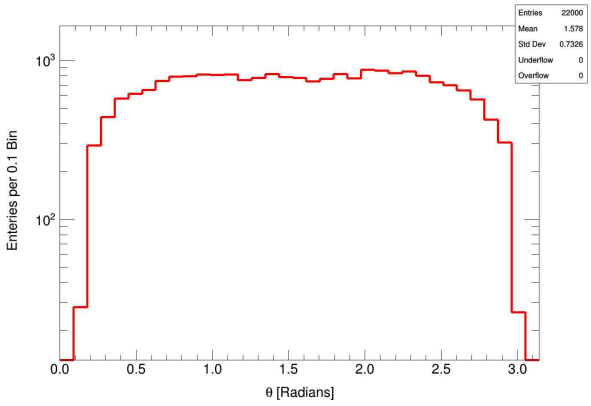
Entries 22000
Mean 1.578
Std Dev 0.7326
Underflow 0
Overflow 0
Enteries per 0.1 Bin
θ [Radians]

(g)

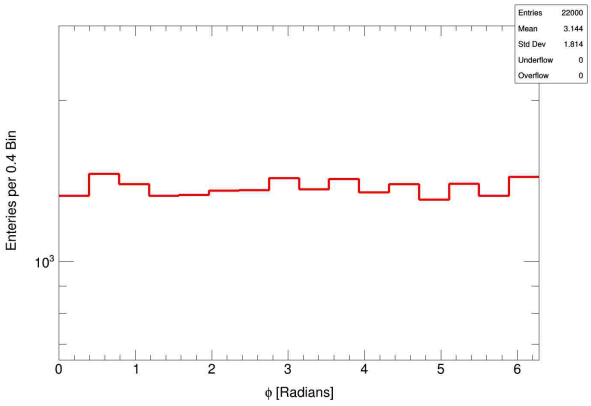
Entries 22000
Mean 3.144
Std Dev 1.814
Underflow 0
Overflow 0
Enteries per 0.4 Bin
ϕ [Radians]

(h)

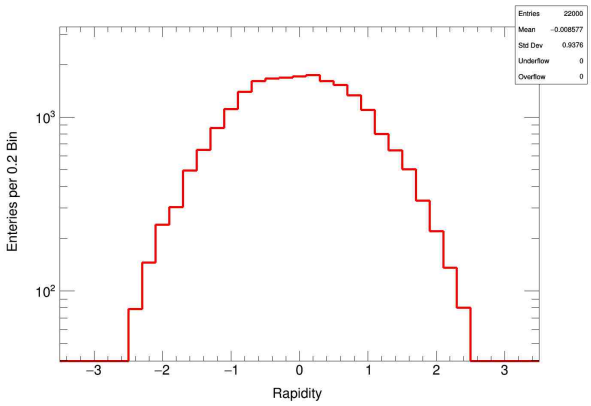
Entries 22000
Mean -0.008577
Std Dev 0.9376
Underflow 0
Overflow 0
Enteries per 0.2 Bin
Rapidity

(i)

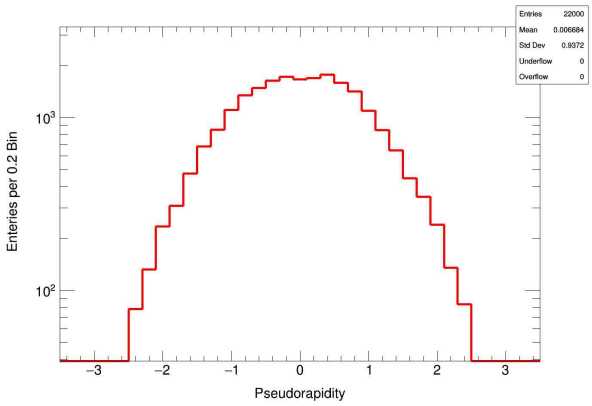
Entries 22000
Mean 0.006684
Std Dev 0.9372
Underflow 0
Overflow 0
Enteries per 0.2 Bin
Pseudorapidity

(j)

A.5 Kinematic Variables of Second Outgoing Parton

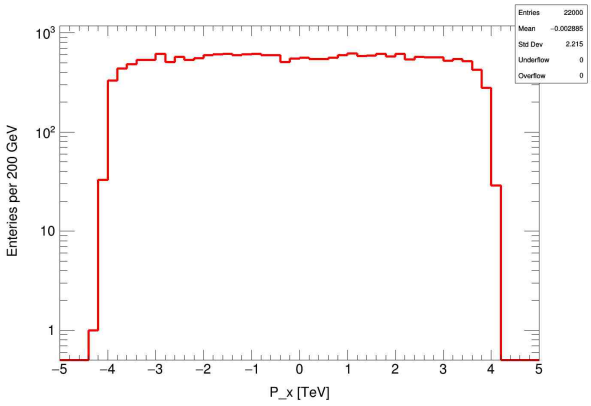

(a)

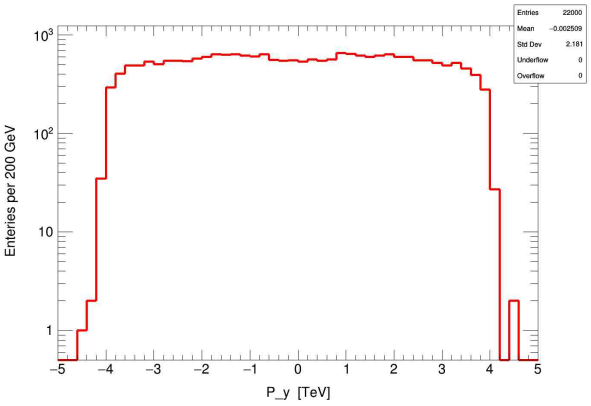

(b)

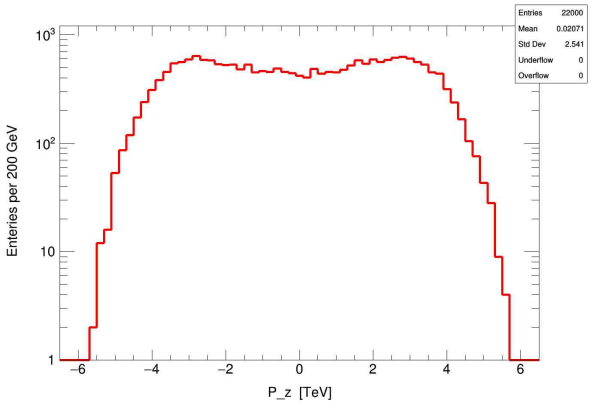

(c)

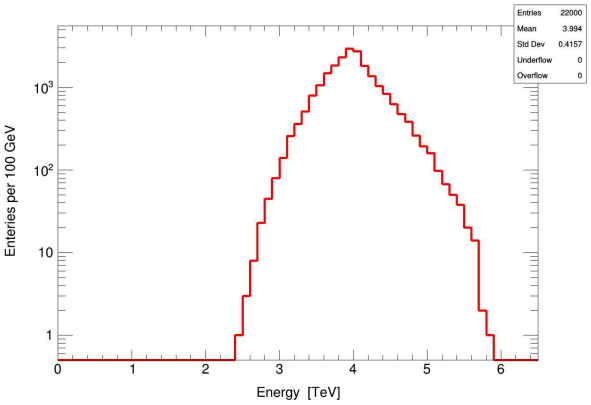

(d)

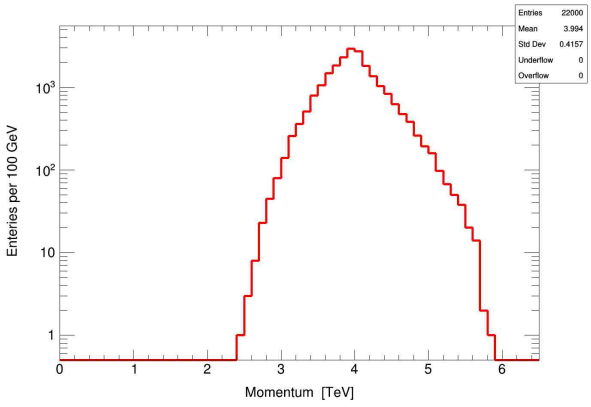

(e)

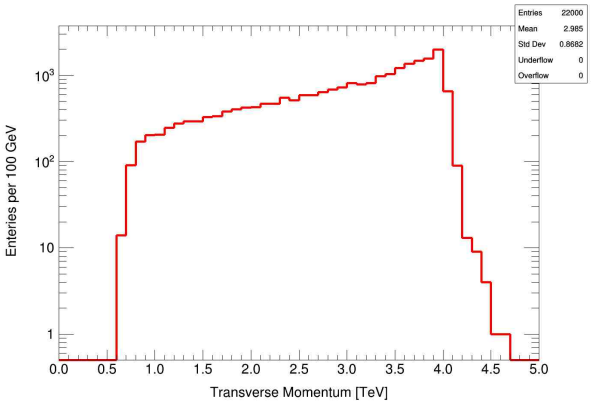

(f)

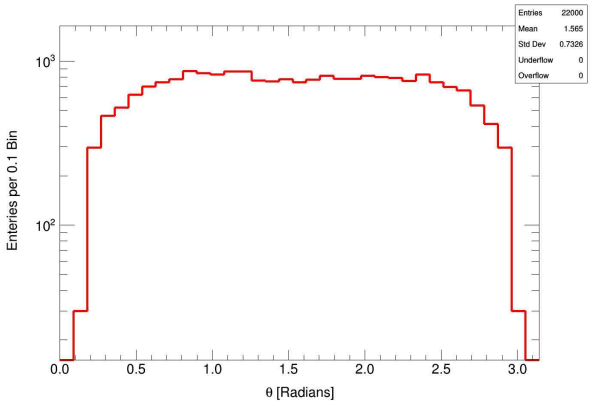
Entries 22000
Mean 1.565
Std Dev 0.7326
Underflow 0
Overflow 0
Enteries per 0.1 Bin
θ [Radians]

(g)

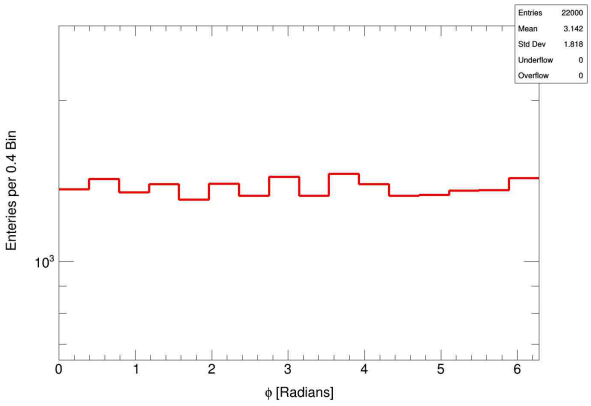
Entries 22000
Mean 3.142
Std Dev 1.818
Underflow 0
Overflow 0
Enteries per 0.4 Bin
ϕ [Radians]

(h)

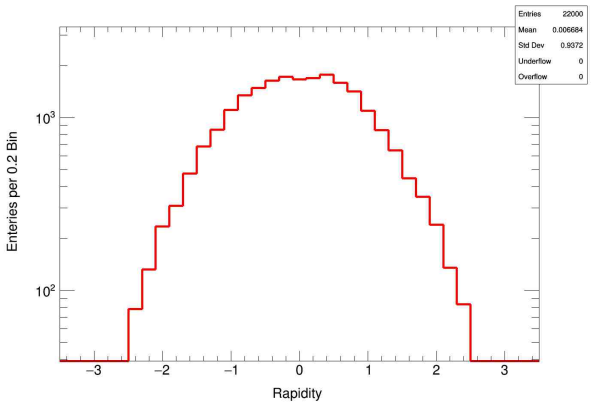
Entries 22000
Mean 0.006684
Std Dev 0.9372
Underflow 0
Overflow 0
Enteries per 0.2 Bin
Rapidity

(i)

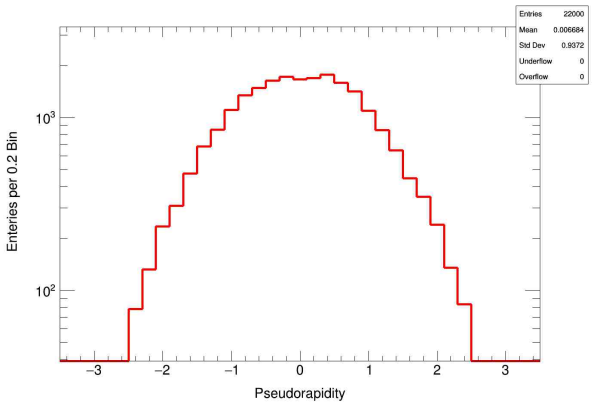
Entries 22000
Mean 0.006684
Std Dev 0.9372
Underflow 0
Overflow 0
Enteries per 0.2 Bin
Pseudorapidity

(j)

A.6 Kinematic Variables of the Two-Parton Combination

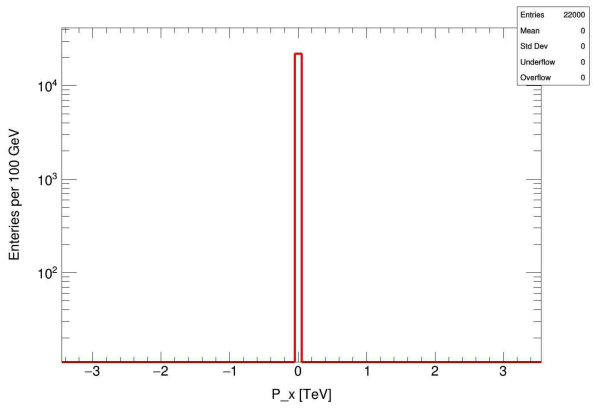

(a)

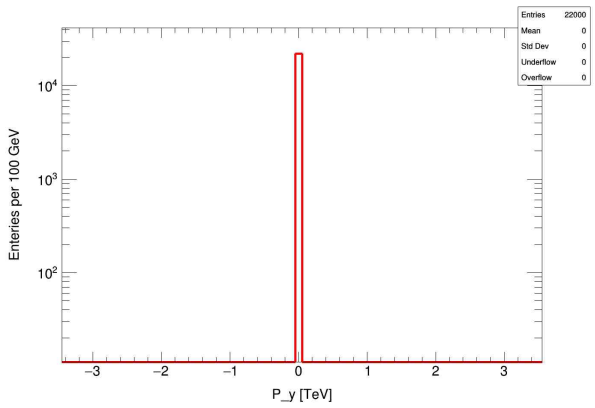

(b)

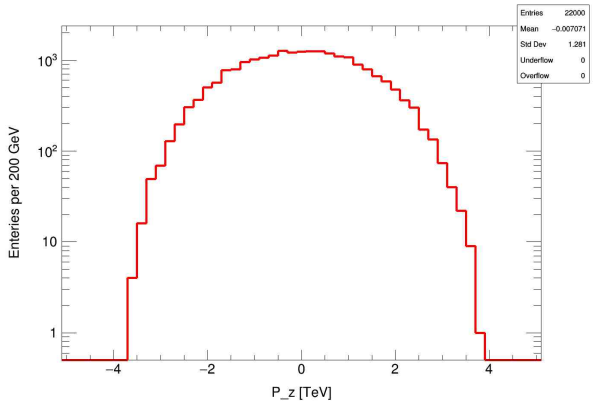

(c)

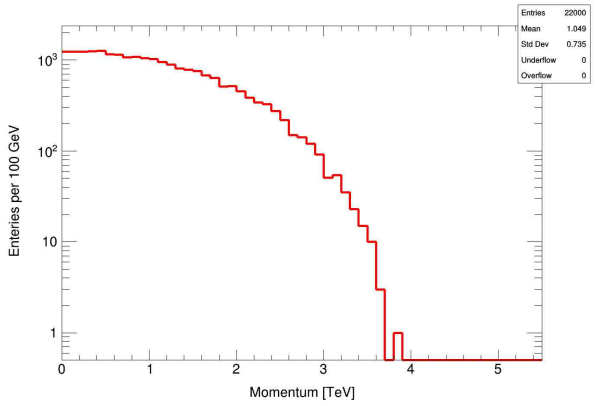

(d)

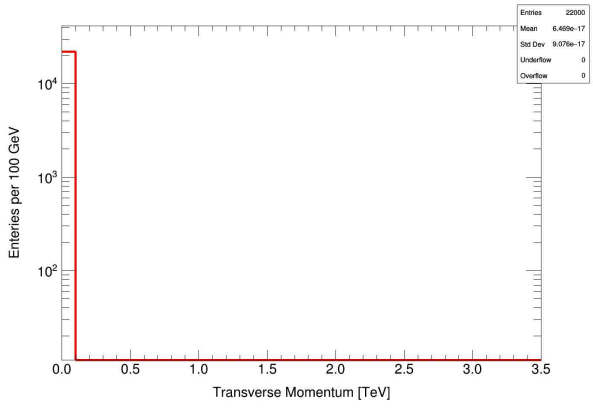

(e)

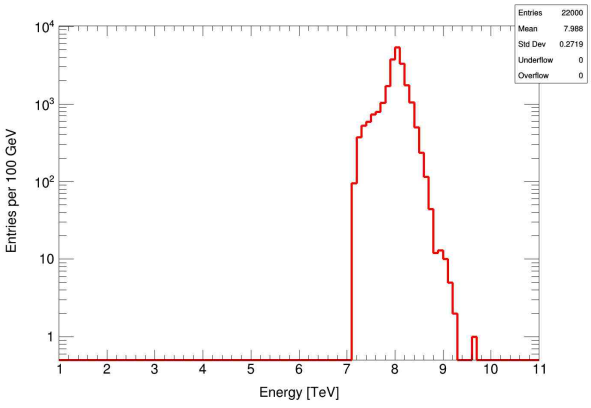

(f)

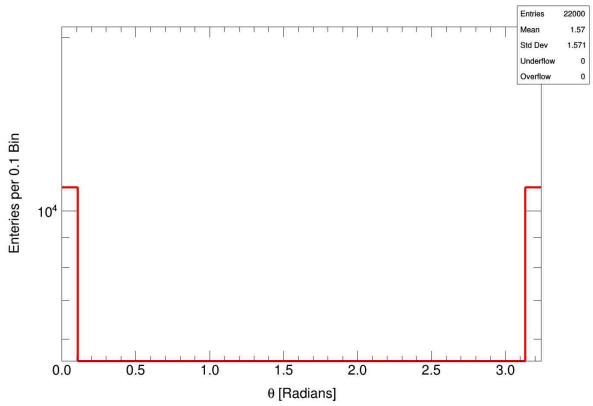
Entries 22000
Mean 1.57
Std Dev 1.571
Underflow 0
Overflow 0
Enteries per 0.1 Bin
θ [Radians]

(g)

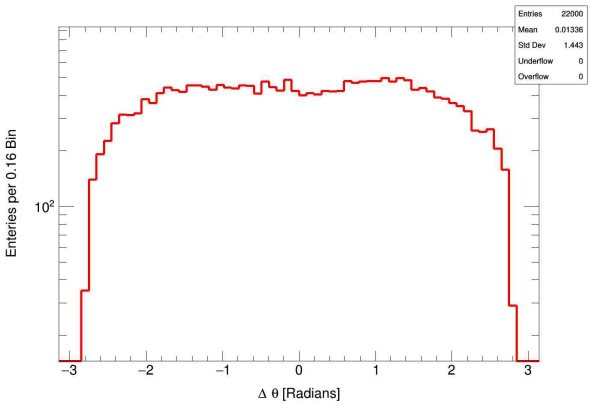
Entries 22000
Mean 0.01336
Std Dev 1.443
Underflow 0
Overflow 0
Enteries per 0.16 Bin
Δ θ [Radians]

(h)

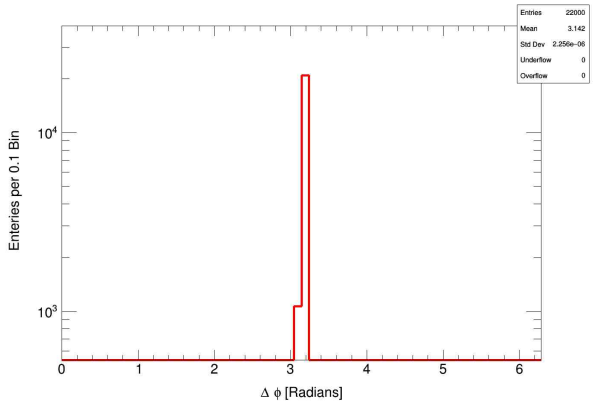
Entries 22000
Mean 3.142
Std Dev 2.256e-06
Underflow 0
Overflow 0
Enteries per 0.1 Bin
Δ ϕ [Radians]

(i)

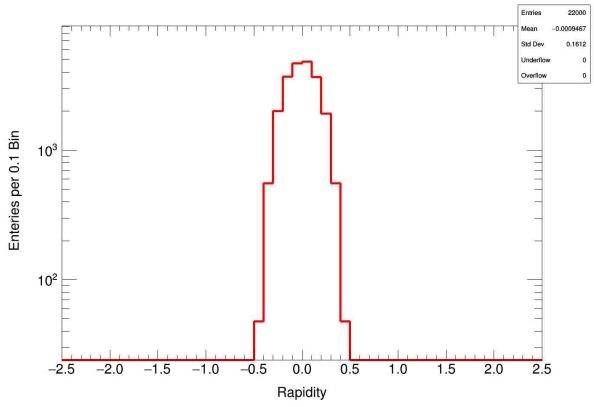
Entries 22000
Mean -0.0009467
Std Dev 0.1612
Underflow 0
Overflow 0
Enteries per 0.1 Bin
Rapidity

(j)

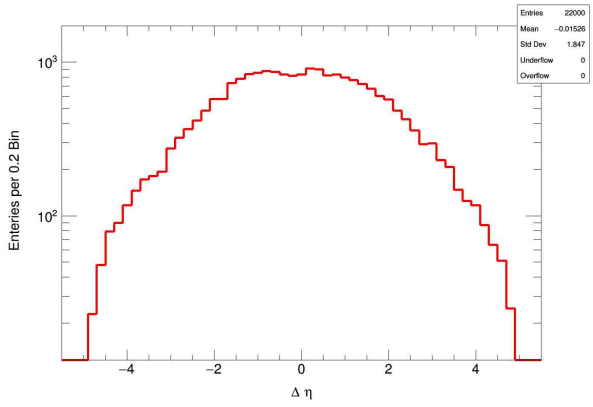
Entries 22000
Mean -0.01526
Std Dev 1.847
Underflow 0
Overflow 0
Enteries per 0.2 Bin
Δ η

(k)

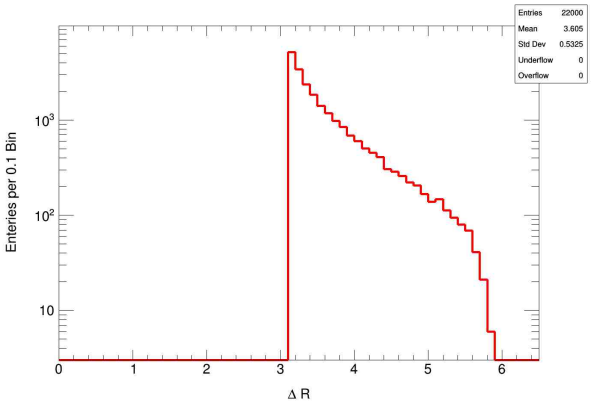
Entries 22000
Mean 3.605
Std Dev 0.5325
Underflow 0
Overflow 0
Enteries per 0.1 Bin
Δ R

(l)

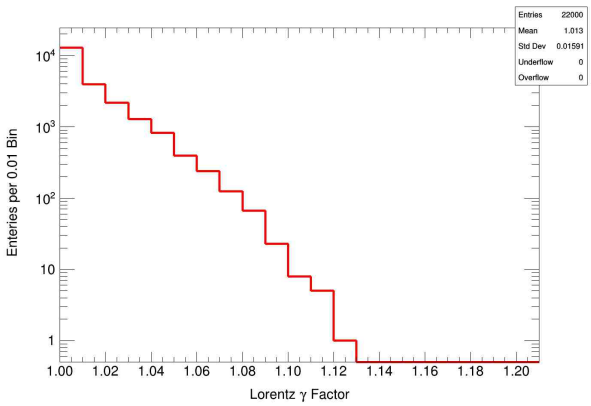

(a)

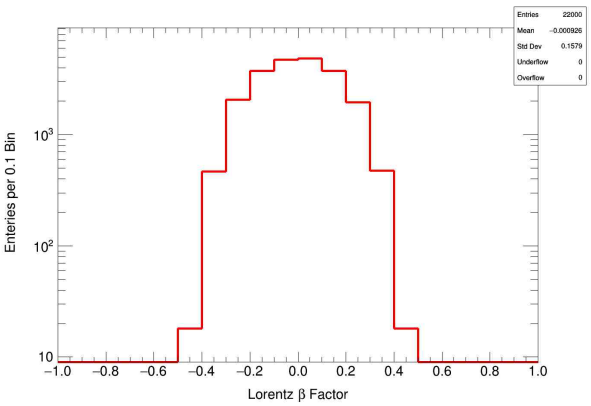

(b)

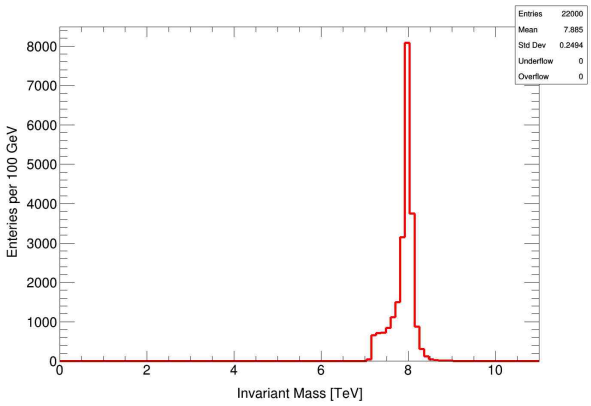

(c) Linear-scale

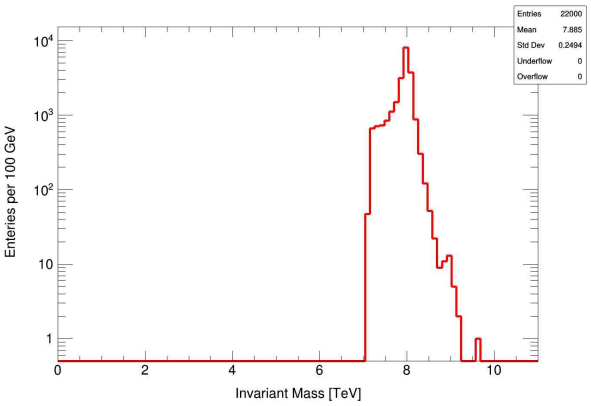

(d) Log-scale

Appendix B

Jet-level validation plots for STRINGS-1.00

Parameters:

13000	Centre of Mass Energy (GeV)
22000	Number of Generated Events by STRINGS
9000	String Scale (GeV)
8047	Minimum Invariant Mass (GeV)
13000	Maximum Invariant Mass (GeV)
2.5	Upper Bound for the Rapidity of the Outgoing Partons
cteq6l1	PDF Set of the LHAPDF
9000	Scale at Which the PDF Set is Evaluated (GeV)
-1	Running Coupling Constant (alpha_s without 4*pi Factor)
9000	Scale at Which the Running Coupling is Calculated (GeV)
0.005	Mass of the Down Quark (GeV)
0.002	Mass of the Up Quark (GeV)
0.001	Mass of the Strange Quark (GeV)
1.27	Mass of the Charm Quark (GeV)
4.4	Mass of the Bottom Quark (GeV)
172.0	Mass of the Top Quark (GeV)
false	(Disabled) Production of QCD tree-level diparton
true	(Enabled) Production of First String Resonance
false	(Disabled) Production of Second String Resonance
true	(Enabled) gg $\rightarrow$ gg Subprocess (ID = 1)
true	(Enabled) gg $\rightarrow$ qqbar Subprocess (ID = 2)
true	(Enabled) gq $\rightarrow$ gq Subprocess (ID = 3)
true	(Enabled) gqbar $\rightarrow$ gqbar Subprocess (ID = 4)
true	(Enabled) qqbar $\rightarrow$ gg Subprocess (ID = 5)
false	(Disabled) gg $\rightarrow$ gGamma Subprocess (ID = 6)
false	(Disabled) gq $\rightarrow$ qGamma Subprocess (ID = 7)

B.1 Kinematic Variables of First Outgoing Jet

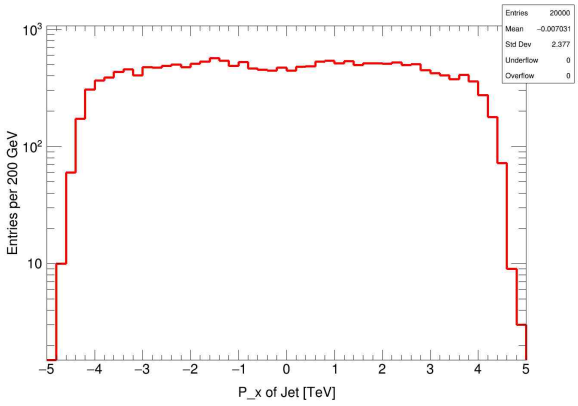

(a)

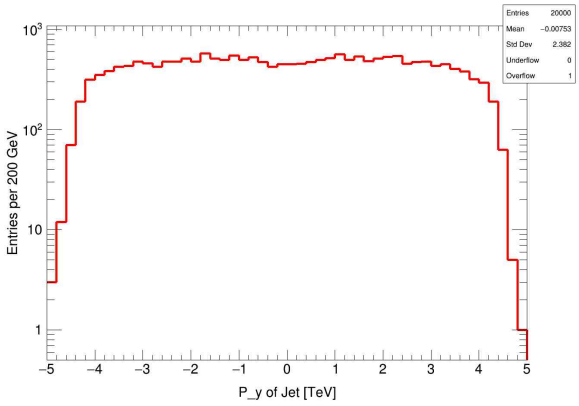

(b)

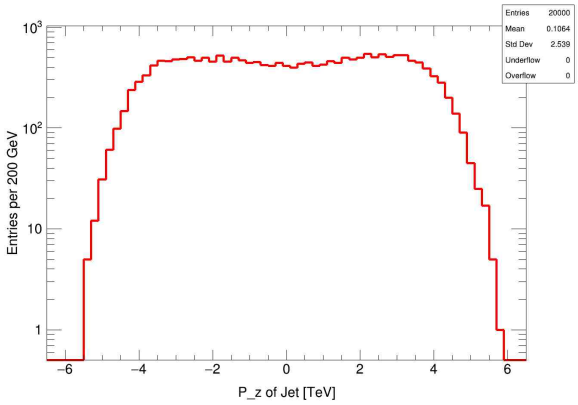

(c)

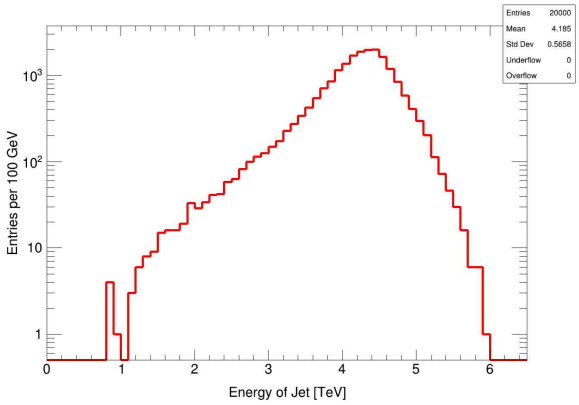

(d)

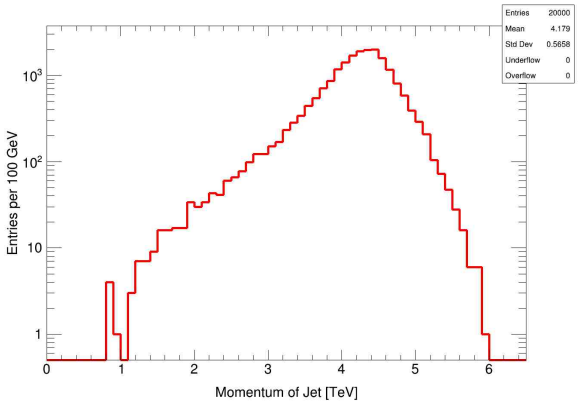

(e)

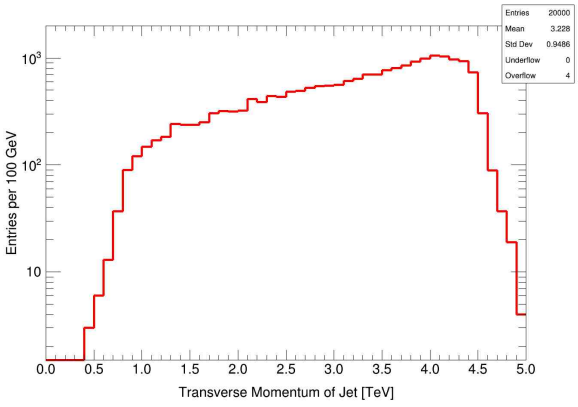

(f)

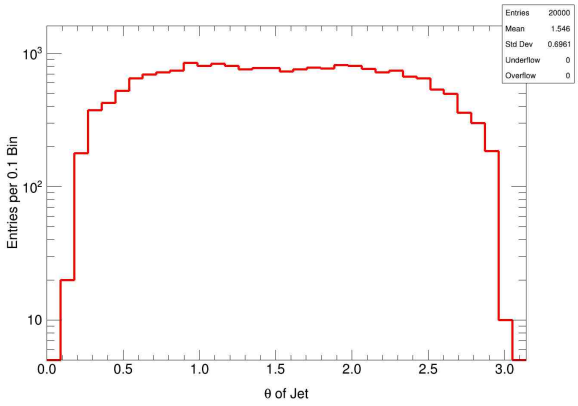
Entries 20000
Mean 1.546
Std Dev 0.6961
Underflow 0
Overflow 0
Entries per 0.1 Bin
θ of Jet

(g)

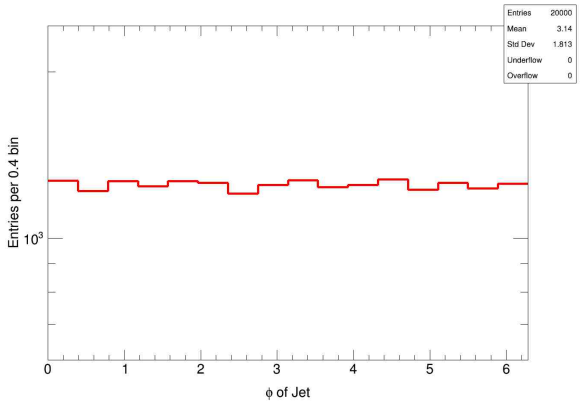
Entries 20000
Mean 3.14
Std Dev 1.813
Underflow 0
Overflow 0
Entries per 0.4 bin
ϕ of Jet

(h)

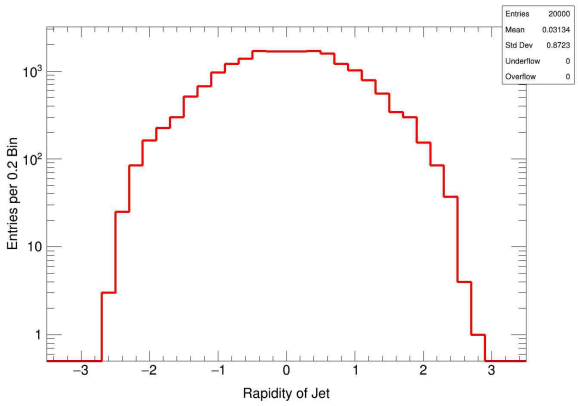
Entries 20000
Mean 0.03134
Std Dev 0.8723
Underflow 0
Overflow 0
Entries per 0.2 Bin
Rapidity of Jet

(i)

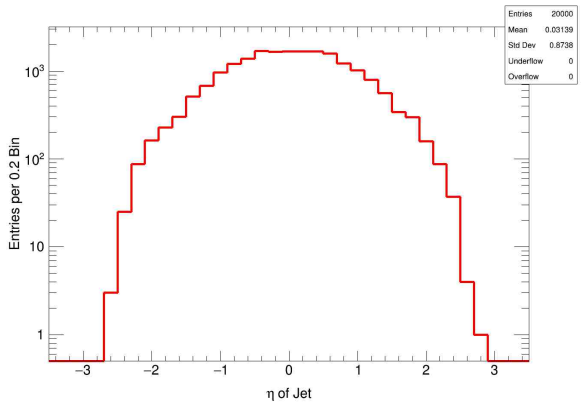
Entries 20000
Mean 0.03139
Std Dev 0.8738
Underflow 0
Overflow 0
Entries per 0.2 Bin
η of Jet

(j)

B.2 Kinematic Variables of Second Outgoing Jet

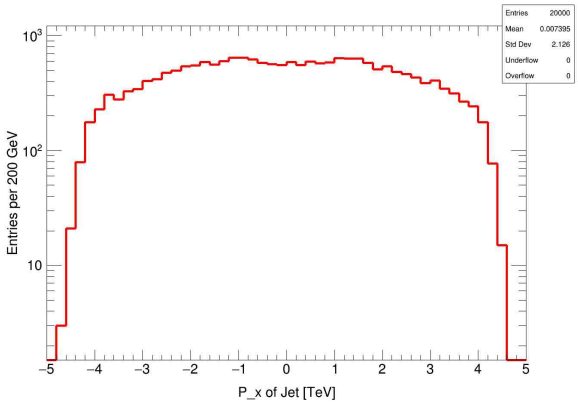

(a)

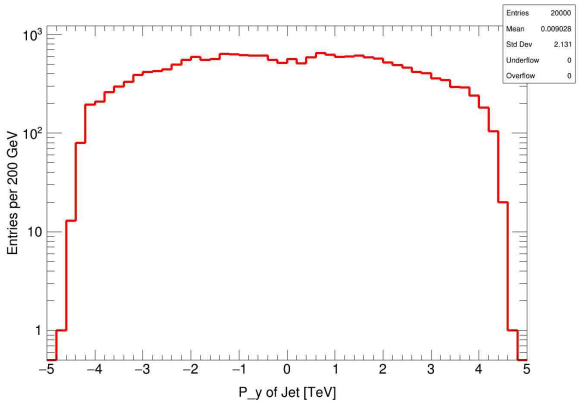

(b)

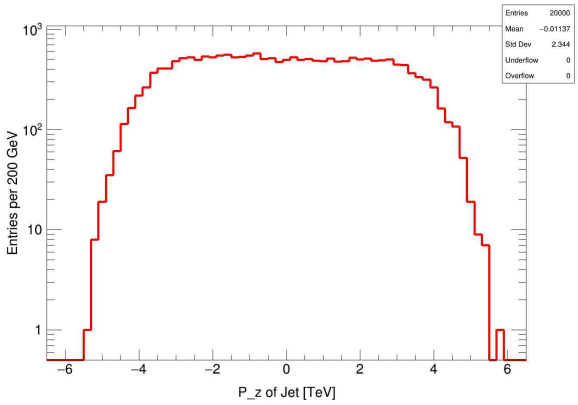

(c)

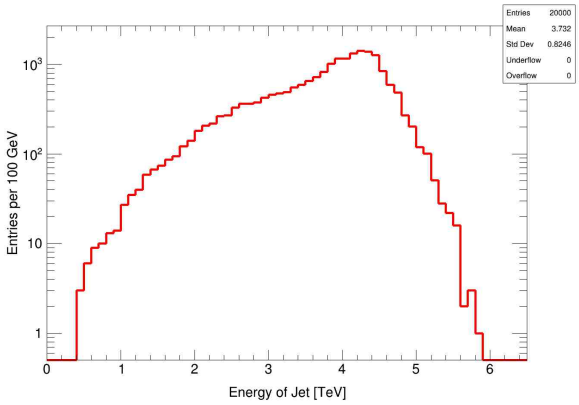

(d)

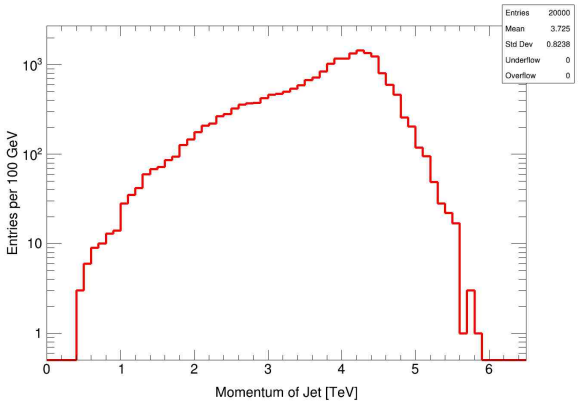

(e)

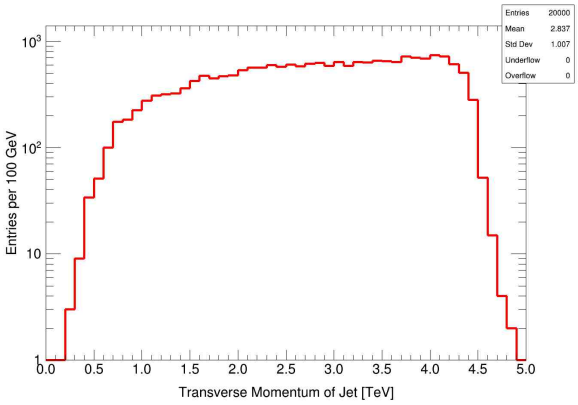

(f)

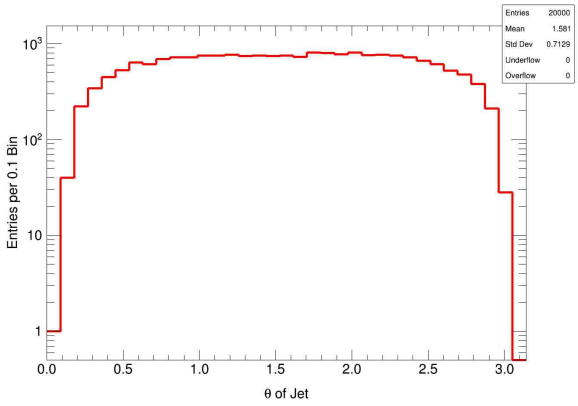
Entries 20000
Mean 1.581
Std Dev 0.7129
Underflow 0
Overflow 0
Entries per 0.1 Bin
θ of Jet

(g)

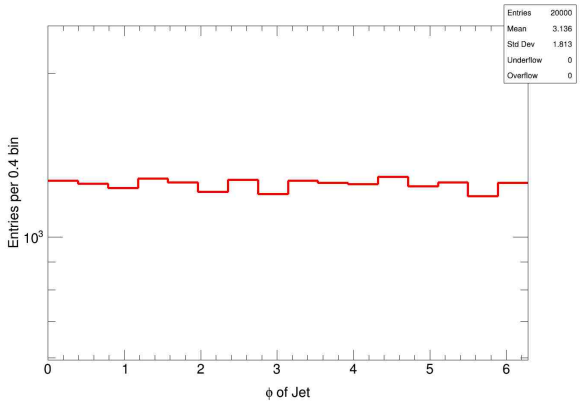
Entries 20000
Mean 3.136
Std Dev 1.813
Underflow 0
Overflow 0
Entries per 0.4 bin
ϕ of Jet

(h)

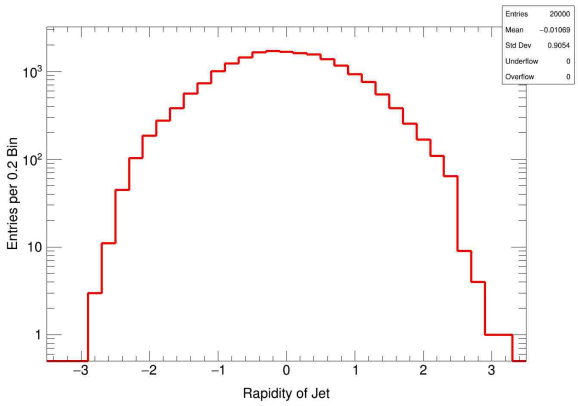
Entries 20000
Mean −0.01069
Std Dev 0.9054
Underflow 0
Overflow 0
Entries per 0.2 Bin
Rapidity of Jet

(i)

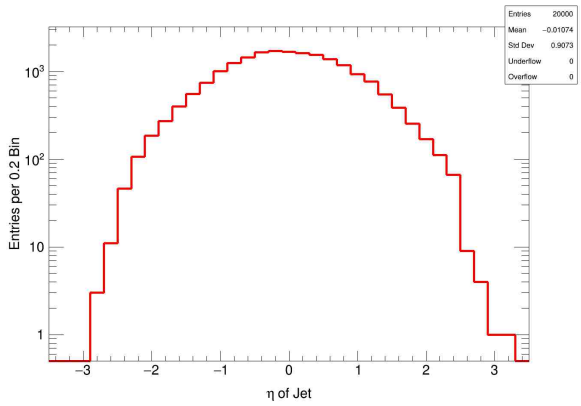
Entries 20000
Mean −0.01074
Std Dev 0.9073
Underflow 0
Overflow 0
Entries per 0.2 Bin
η of Jet

(j)

B.3 Kinematic Variables of the Two-Jet Combination

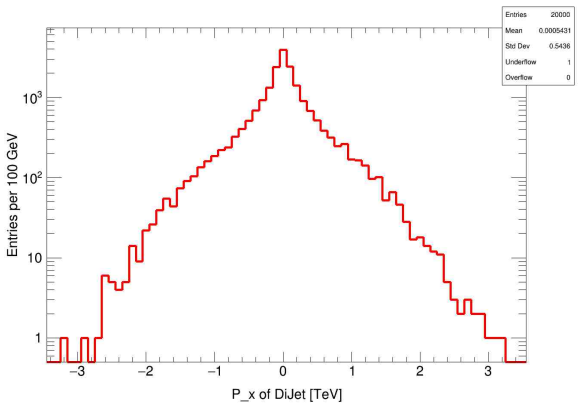

(a)

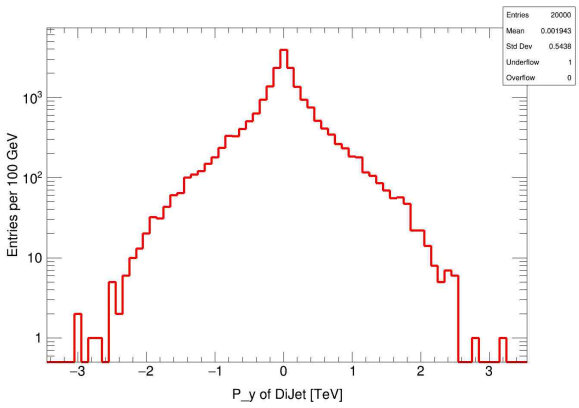

(b)

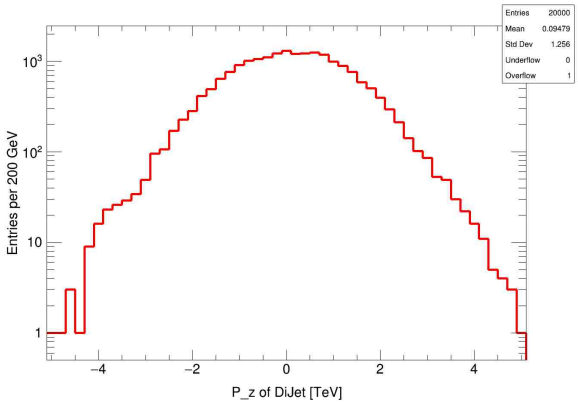

(c)

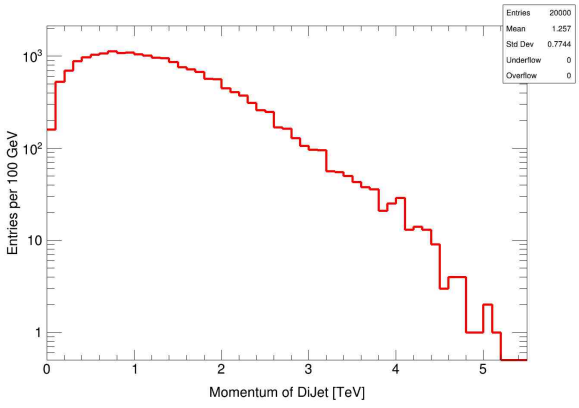

(d)

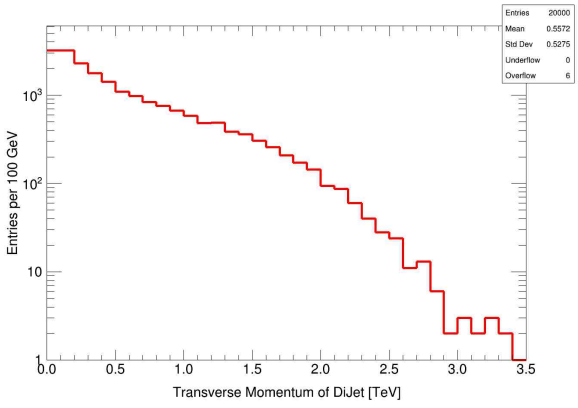

(e)

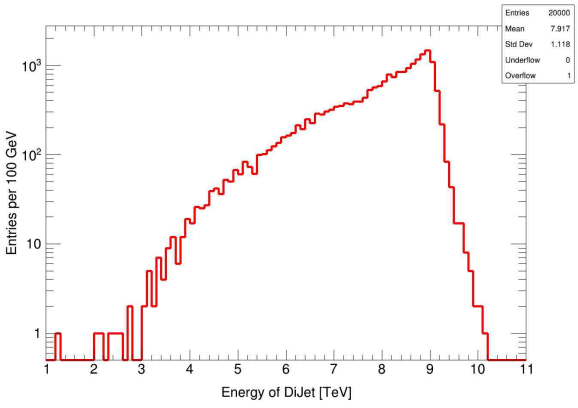

(f)

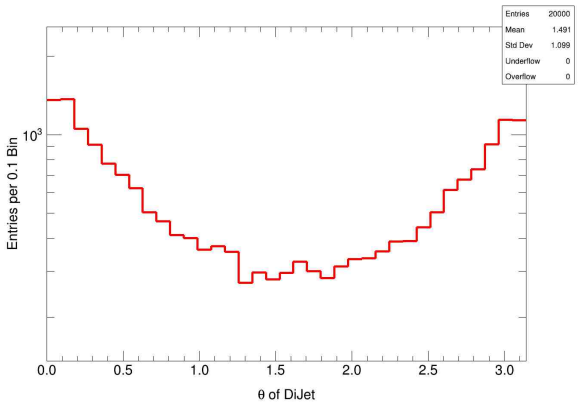
Entries 20000
Mean 1.491
Std Dev 1.099
Underflow 0
Overflow 0
Entries per 0.1 Bin
θ of DiJet

(g)

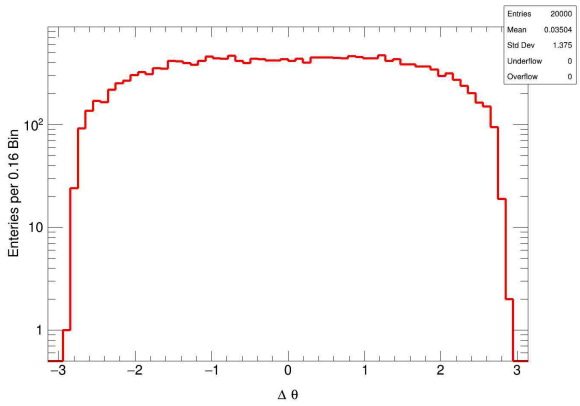
Entries 20000
Mean 0.03504
Std Dev 1.375
Underflow 0
Overflow 0
Enteries per 0.16 Bin
Δ θ

(h)

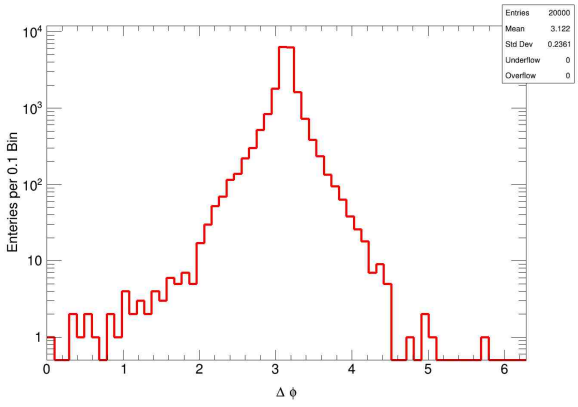
Entries 20000
Mean 3.122
Std Dev 0.2361
Underflow 0
Overflow 0
Enteries per 0.1 Bin
Δ ϕ

(i)

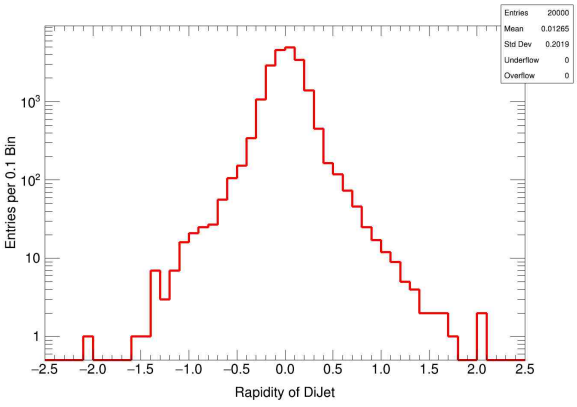
Entries 20000
Mean 0.01265
Std Dev 0.2019
Underflow 0
Overflow 0
Entries per 0.1 Bin
Rapidity of DiJet

(j)

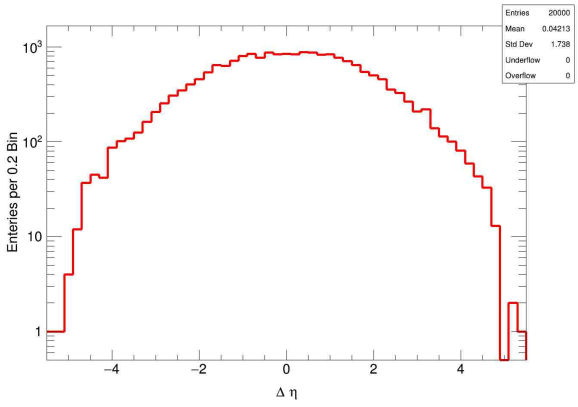
Entries 20000
Mean 0.04213
Std Dev 1.738
Underflow 0
Overflow 0
Enteries per 0.2 Bin
Δ η

(k)

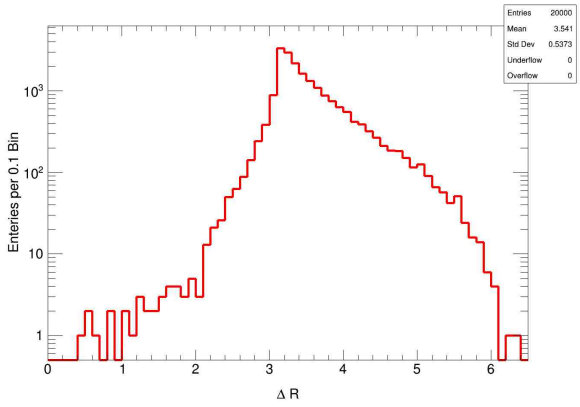
Entries 20000
Mean 3.541
Std Dev 0.5373
Underflow 0
Overflow 0
Enteries per 0.1 Bin
Δ R

(l)

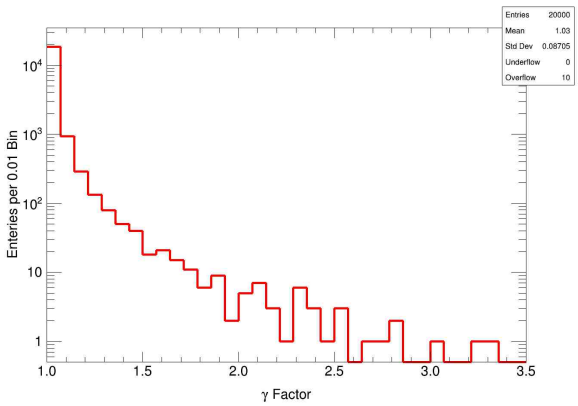

(a)

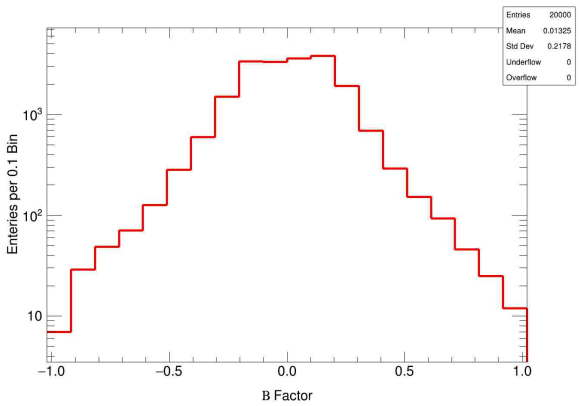

(b)

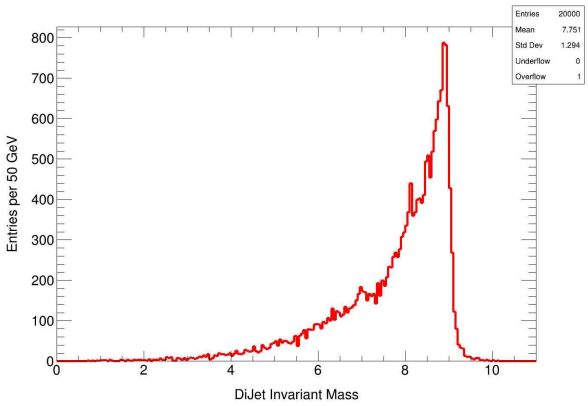

(c) Linear-Scale

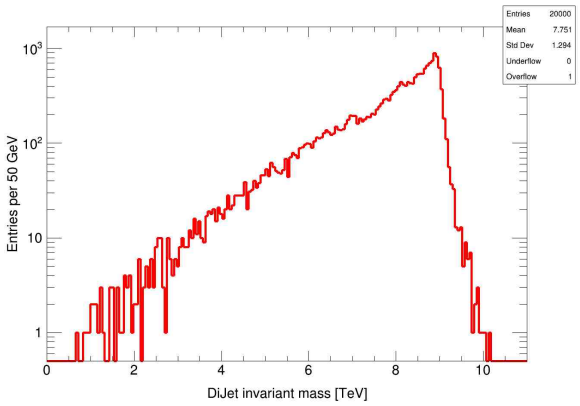

(d) Log-Scale

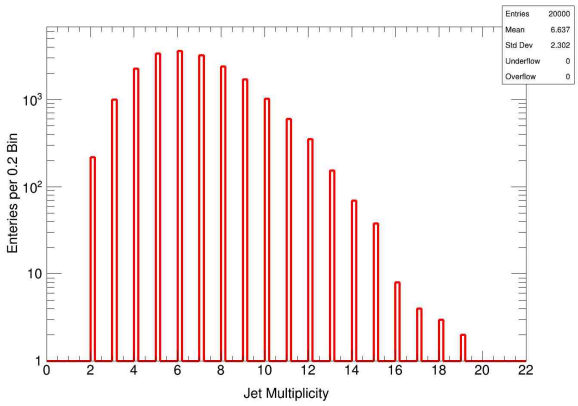

(e)